Universiteit Antwerpen

Faculteit Wetenschappen
Departement Fysica

Carbon nanotubes and graphene based devices: from nanosensors to confined water

Koolstofnanobuisjes en grafeen: van nanosensoren tot ingeperkt water

Proefschrift ingediend tot het behalen van de graad van
Doctor in de Wetenschappen: Fysica
aan de Universiteit Antwerpen, te verdedigen door

Belisa Rebeca Cavalcanti Holanda Tavares de Aquino

Promotoren
Prof. dr. Milorad Milošević
Prof. dr. Mehdi Neek-Amal
Prof. dr. François Peeters

Antwerpen, October 2018

Samenstelling Doctoraatsjury:

Voorzitter
Prof. Dr. Sabine Van Doorslaer, Universiteit Antwerpen, Belgium
Secretaris / plaatsvervangend voorzitter:
Prof. Dr. Sara Bals, Universiteit Antwerpen, Belgium
Leden:
Prof. Dr. Milorad Milošević (promotor), Universiteit Antwerpen, Belgium
Prof. Dr. Mehdi Neek-Amal (promotor), Shahid Rajaee Teacher Training University, Tehran, Iran
Prof. Dr. François Peeters (promotor), Universiteit Antwerpen, Belgium
Prof. Dr. Rahul Nair, Manchester University, UK
Prof. Dr. Erik Neyts, Universiteit Antwerpen, Belgium

Contactgegevens
Belisa Rebeca Cavalcanti Holanda Tavares de Aquino
Universiteit Antwerpen
Departement Fysica
G. U. 209
Groenenborgerlaan 171
2020 Antwerpen
België
belisa.deaquino@uantwerpen.be
belisadeaquino@gmail.com

To my grandmas.
A minhas voinhas.

ACKNOWLEDGEMENTS

I wish to express my sincere gratitude to Professors Milorad Milošević and François Peeters for giving me the opportunity to work in the Condensed Matter Theory (CMT) group at the University of Antwerp. I truly appreciate their support, guidance, constructive criticism and patience during my PhD, which were essential to materialize this thesis. I deeply thank Prof. Mehdi Neek-Amal for his encouragement, invaluable advises and constant availability for fruitful discussions during the whole PhD.

I would like to thank all the members of the jury for their prompt availability and for their constructive and helpful comments to improve the quality of this thesis. I also thank Robbe for translating the summary of my thesis to Dutch. I must say a special thanks to Hossein for his help, collaborative work and inputs, without which this thesis would not have been completed.

I am very grateful to Hilde and Véronique for their kindness and help with administration and logistic support. I also thank Nikolas for his IT support and for contributing to a more cheerful workplace.

I kindly thank all my friends from the CMT group and outside of it. To the South American "gang", Ariel, Diegão, William, Diego Maluco, Lucas, Davi, Jorge Capuã, Jorge Bezerra, Guga, Rafael, Débora, Felipe, Pablo, Jesus, Jagger, Alfredo and Tabhita, I thank you for keeping a warm piece of home near me during the PhD years. To Slaviša, Miša, Donjan, Vincent, Nina and PJ, thank you for the good times together that made those years much more pleasant. To Sara and Samira, for their sisterhood and for the hard and necessary task to keep the woman power in science. To my old friends in Brazil, Ju, Raquel, Ciça, Rafa, Ana, Higor, Berna, Leo, Cyreno, Erik, Dentinho, Tiago and Hugo, thank you for always arranging some time to be around during my trips to Recife. I thank everyone who directly or indirectly contributed to this thesis.

I warmly thank my family for their unconditional support. Particularly, my parents and brother, who always made the (im)possible to shorten the distance between the two continents (by the way, mom, you can include one more turn around the Earth in your count of trips that you made so that we could be together; now it is a return trip to the Moon plus eight and a half trips around the Earth). I thank my uncle Julio that, together with my father, strongly *encouraged me to pursue this PhD. To Toninho, Andrei and Danilo, thank you for always being there for me during those years. I specially thank my my grandmother Zefinha, who have been present in all of the most important moments of my life and my grandmother Isabel, for the warmest and last hug before I boarded the plane to leave Brazil.*

I deeply thank my partner in life and adventures, Víctor, for the love, support, care and encouragement during those years. I must also thank, once again, for helping me with the luggages when I landed here. Now there are more luggages to come, but at this time we will carry them together.

TABLE OF CONTENTS

Part I

Introduction

CHAPTER 1

GENERAL INTRODUCTION

Carbon is a Group-IV element known to form many different compounds. It has outstanding properties such as the four valence bonds and affinity to bind to small atoms, including other carbon atoms, enabling therefore the production of complex molecules and different carbon allotropes. As a result, it plays a fundamental role for life on Earth and enables the most diverse applications, ranging from hydrocarbons and their importance for the petrochemical industry and for the fabrication of synthetic materials to the utilization of graphite, diamond and other carbon allotropes with their distinct properties.

Water is another essential aspect for the existence of life and its evolution. It is present in everyone's daily life and composes about 70% of the Earth surface and over half of the human body. Water is irreplaceable, the human body cannot live without it for more than a few days. Its importance ranges from its role as a solvent, to the ability to structure proteins, nucleic acids and cells. Yet, about only 3% of the water found on Earth is clean, i.e. fresh water, and the ongoing population growth demands the development and improvement of techniques to obtain drinkable water, such as desalination.

Given the importance of both carbon and water, it is crucial to understand their unique properties and anomalies. This can allow the development of new techniques to manipulate and purify water, as well as to achieve controlled assembly and expand the applicability of carbon-based materials. The present

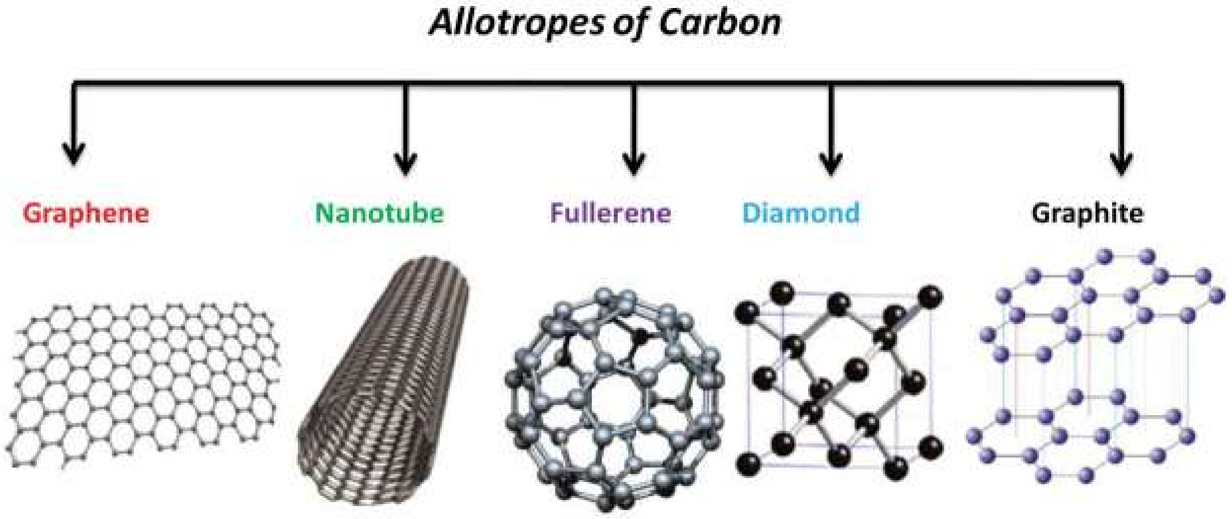

FIGURE 1.1. Different carbon allotropes. Figure taken from Ref. [1].

thesis aims to study both carbon-based hybrid materials and water confined in carbon-based nanochannels by using computational approaches.

1.1 Carbon-based materials

The ability to form several carbon allotropes enables the existence of carbon-based materials with very distinct properties. For example, while diamond is the hardest known natural mineral, graphite is one of the softest. The difference between them arise from their distinct atomic structures. Diamond is a rigid three-dimensional (3D) structure where carbons arrange tetrahedrally, covalently bonded to four other carbons. This structure gives diamond its well known hardness and high light dispersion, making it suitable for industrial applications and jewelry. On the other hand, the carbon atoms in graphite are layered, covalently bonded in-plane to three other carbons forming a hexagonal lattice, while the layers are held together by a weaker van der Waals stacking interaction. The graphite structure is responsible for its conductance, since the fourth carbon electron is free to move in-plane, and for the use of graphite in pencils, since the layers can be readily cleaved.

Recently, other carbon allotropes with remarkable properties and covering all spatial dimensions have been synthesized, e.g., graphene (2D), carbon

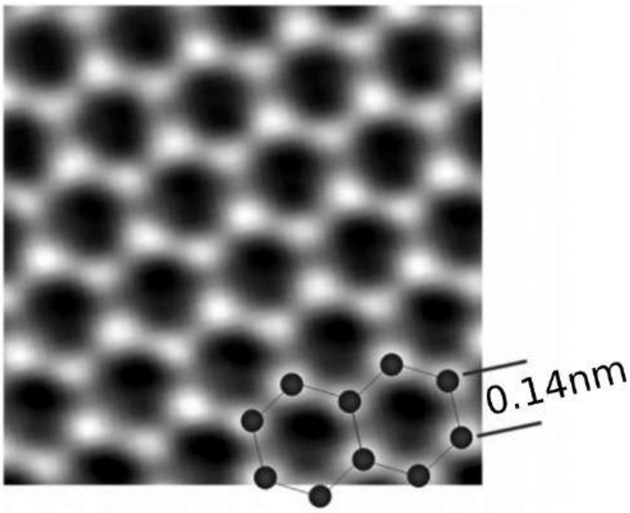

FIGURE 1.2. Transmission electron aberration-corrected microscope image (TEAM) showing the carbon atoms and the honeycomb structure of graphene. Figure adapted from Ref. [2].

nanotubes (~1D) and fullerenes (~0D). While graphene is defined as one single layer of the honeycomb lattice found in graphite structure, a carbon nanotube consists of folded graphene sheet(s) into a cylindrical shape. The smallest fullerene, known as C_{60} is formed by carbon hexagons and pentagons and resembles a football. The structures of different carbon allotropes are depicted in Fig. 1.1. In this thesis, both graphene and carbon nanotubes (CNTs) will be considered and their synthesis, features and properties are briefly discussed below.

1.1.1 Graphene

Graphene is the mother of the graphitic forms of carbon. The weak inter-layer physical bond in graphite in contrast to the strong intra-layer chemical bond enables the isolation of one single layer, i.e. graphene, without damaging the layer itself. However, it was only in 2004 that with a simple micromechanical cleavage method the isolation of a single layer of graphene from graphite was achieved [3]. The identification of graphene was facilitated by transferring the sample into a SiO_2 silicon wafer. The synthesis and identification of graphene was conducted by A. G. Geim and K. S. Novoselov and together with its extraordinary properties led to the Nobel Prize in 2010 and to a new research field.

After its identification, graphene emerged as a new hope for the scientific community and in the field of technological applications. Since then, the honeycomb structure of graphene has been experimentally identified (see Fig. 1.2) and its properties have been extensively investigated [1, 4]. Hidden in its atomic structure lies very high electronic and thermal conductivities, as well as remarkable mechanical, optical and electronic properties [5–8]. Besides being the purest form of carbon, graphene has a very large specific area, being the lightest and the thinnest material ever known, while being the strongest material ever measured. The extremely high strength of graphene is related to its atomic structure, i.e., this is due to the very short C=C bond ($\sim 1.42\,\text{Å}$).

Several top-down and bottom-up methods for the synthesis of graphene have been developed, each one has its advantages and disadvantages [1, 4]. Chemical exfoliation, one of the most familiar techniques, is time-consuming, and requires the use of hazardous chemicals needed and produce samples with defects that might affect their properties. Micromechanical cleavage produces high-quality graphene sheets, however it is also very time-consuming. Chemical vapor deposition (CVD) is one of the best regarding high-quality samples, nonetheless it is very expensive and demands sophisticated instruments. Still none of the methods developed up to date fulfill the requirements for the fabrication of inexpensive and eco-friendly scalable high-quality graphene, and it still is the main challenge for novel technologies to benefit from its great properties. For more details on production methods of graphene, the interested reader is recommended to read Ref. [4].

1.1.2 Carbon nanotubes

Carbon nanotubes consist of cylindrically rolled up graphene sheets. They can be formed either by only one single graphene sheet, i.e., single-walled carbon nanotubes (SWCNTs) or by several graphene sheets, i.e., multi-walled carbon nanotubes (MWCNTs). The discovery of CNTs is attributed to S. Iijima in 1991, who first observed MWCNTs and subsequently SWCNTs [11]. Since

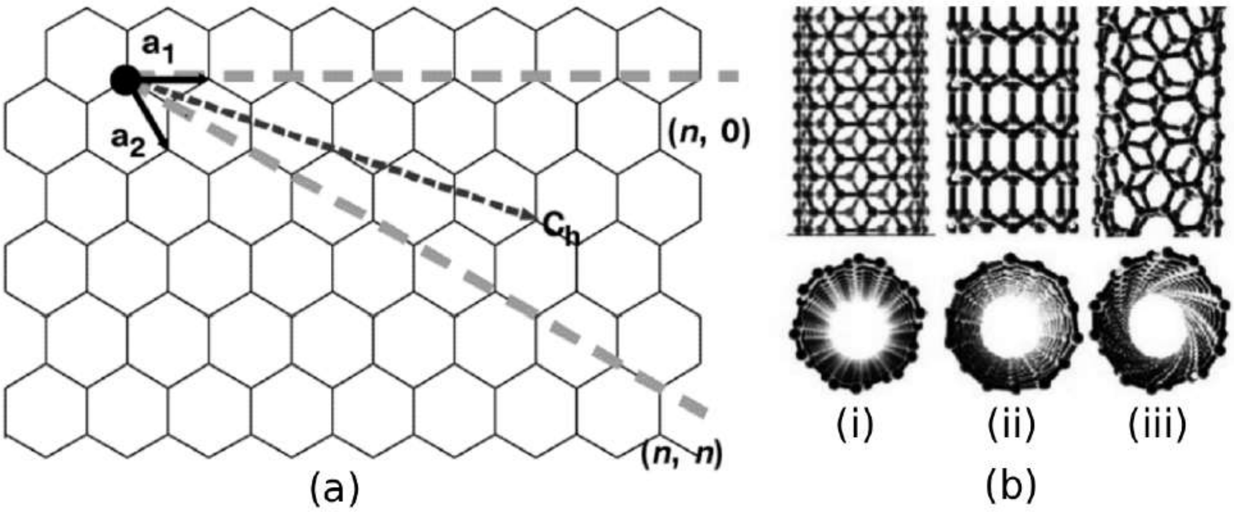

FIGURE 1.3. (a) The chiral vector of a carbon nanotube in a graphene sheet. (b) Atomic structure of CNTs with different helicities: (i) armchair, (n,n), (ii) zigzag, (n,0), and (iii) chiral, (n,m). Figure adapted from Refs. [9, 10].

this achievement, the scientific community focused on the investigation of CNTs remarkable properties and potential applications.

Carbon nanotube is the second hardest material known after graphene. CNTs can conduct electricity better than copper and transmit heat better than diamond. They also have extremely high strength, low mass density and nanometer scale structure. The CNT diameter ranges from $< 1\,\text{nm}$ up to $70\,\text{nm}$, while the typical CNT length is in the order of several microns. Due to their high aspect ratio, CNTs form nearly 1D nanotubes [12].

The CNT properties such as diameter and chiral angle are directly related to its electromechanical properties, e.g., they determine if a CNT acts as a metal or as a semiconductor. The diameter and chiral angle of a CNT are defined by the chiral vector $\mathbf{C_h} = n\mathbf{a_1} + m\mathbf{a_2}$, which indicates the direction at which the graphene sheet is rolled up to form the CNT and it is depicted in Fig. 1.3(a). Depending on the chiral vector, three different types of CNT can be formed. If $m = n$, CNTs are called *armchair* (Fig 1.3(b-i)), while if $m = 0$, they are *zigzag* CNTs (Fig 1.3(b-ii)) and in any other case CNTs are named *chiral* (Fig 1.3(b-iii)). The angle between the chiral vector and the zigzag direction ($m = 0$) is the chiral angle θ, i.e., zigzag (armchair) CNTs have $\theta = 0°$ ($\theta = 30°$)

and chiral CNTs have $0° < \theta < 30°$.

Hundreds of tons of CNTs are produced annually. However, scalable CNT production still depends on overcoming fabrication challenges, with the regulation of the CNT properties being the main obstacle. Aiming potential electronic applications, the best approach for the synthesis of CNTs involves deposition or growth on substrates. Some of the methods to generate CNTs are arc-discharge, laser ablation and chemical vapor deposition (CVD), the latter being one of the best methods to produce CNTs for nanoelectronics fabrication, since it involves lower temperatures in comparison to the other methods and enables significant control in shape, size and specific physical properties of the produced CNTs [13]. For a detailed description of the production methods of CNTs we refer the reader to Ref. [1].

Carbon nanotubes can also be functionalized by indirect or direct physicochemical and physical methods. For example, the carbon nanotubes can be coated with noble and transition metals in order to enhance its properties or broaden its potential applications [14]. Carbon nanotubes can be decorated with nanoparticles by, e.g., evaporation deposition, sputtering or ion/electron beam irradiation. In Chapter 3, the structural and dynamical properties of nanoparticles decorated on carbon nanotubes are investigated.

1.1.3 Applications

Due to their outstanding properties, graphene and graphene-like materials have attracted strong interest for different technological applications. Due to an optical transmittance of more than 98%, graphene can be used in transparent and flexible electronics [15]. The high strength, low weight and high flexibility of CNTs have projected CNTs as one of the best candidates as reinforcing nanofillers [16]. The potential of CNTs to be used as substrates for metallic nanowires have also been widely explored [14]. Pristine or functionalized graphene-based materials can have significant impact in the areas of biochemical sensors, fuel cells, energy storage and filtration devices [4, 17–21]. This thesis will focus on the use of graphene-like materials for mass sensing and confining/separation purposes.

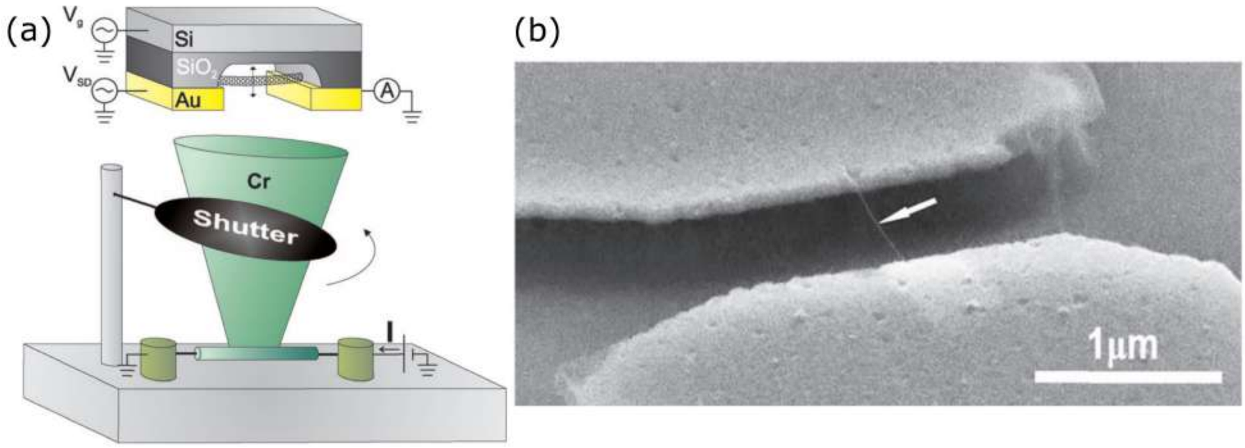

FIGURE 1.4. CNT resonator for mass sensing. (a) Schematic representation of the setup. Chromium atoms are deposited onto the CNT in a Joule evaporator and the mass of the adsorbed atoms is measured. (b) Scanning electron microscopy image of the nanotube resonator. Figure adapted from Ref. [24].

1.1.3.1 Nanosensors

Nanoresonators made of CNTs or graphene exhibit remarkable electromechanical properties which enable frequencies up to the order of gigahertz to be reached [22]. Such unprecedented feature has denoted the potential application of such nanoresonators as nanosensors for detection and differentiation of distinct atom/molecules based on vibration analyses.

The operational principle of nanosensors is the detection of shifts in resonance frequencies caused by surrounding or attached particles. Vibration analyses enables the use of nanoresonators to detect atoms or molecules at very low concentrations [23–26]. The potential of nanosensors range from early disease detection and DNA sequencing to gas detection. A typical experimental setup of a doubly-clamped CNT resonator is shown in Fig. 1.4.

Experimental studies have reported mass sensing under several conditions leading to different sensitivities, e.g., a sensitivity of an attogram (10^{-18} g) [23] was achieved with a doubly clamped CNT resonator with resonance frequencies greater than 1.3 GHz and with higher frequencies in the order of THz expected by scaling down the CNT resonator and selecting suitable coating materials. Decreasing the temperature also enabled better results for a SWCNT resonator, with a sensitivity of 25 zg (25×10^{-21}) at room temperature being improved to 1.4 zg at a temperature of 5 K [24]. By using doubly clamped SWCNT resonators at low temperatures (6 K), mass sensing at atomic-scale precision (0.066 zg) was achieved [25].

More recently, mass sensing experiments with a resolution of 1.7 yg (1.7×10^{-24} g), which corresponds to the mass of one proton, and reaching frequencies of almost 2GHz have been reported [26]. And the potential of gene detection by using vibration analysis on CNT resonators have been computationally investigated, predicting frequencies at the order of 0.1 THz [27]. Despite the high-sensitivity already achieved, the potential application of nanoresonators as nanosensors still face the challenge to differentiate distinct types of atoms/molecules with close densities and at the same environmental conditions. In Chapter 4, the sensing ability of a decorated CNT resonator is investigated by applying electric field.

1.1.3.2 Nanocapillaries

The development in the ability to fabricate artificial nanocapillaries has enabled novel research on molecular transport and nanofluidics [28]. Pores and capillaries of nanometer dimensions are widespread in nature. They also have several potential applications, such as chemical separation, water desalination and filtration [21]. In this sense, carbon nanotubes and graphene nanocapillaries appear as great candidates due to their atomically smooth walls and high aspect ratio.

Recently, the fabrication of narrow and smooth graphene capillaries with channel heights controlled with atomic-scale precision have improved their reproducibility and increased their potential for technological applications [29]. Fig. 1.5(a) shows a schematic view of a capillary device consisting of atomically flat top and bottom graphite separated by an array of spacers made of multilayer graphene stripes of controlled thickness. A free-standing Si nitride membrane with a rectangular hole is used as a support. A top view of the assembly is shown in the scanning electron microscopy (SEM) image in Fig. 1.5(b) [29]. Several studies on gas, liquid and ionic transport through carbon nanotubes and graphene nanopores have been reported [21, 29–33]. It

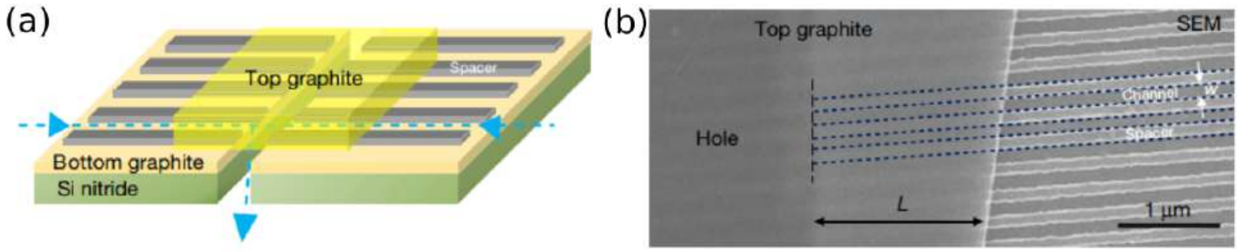

FIGURE 1.5. Graphene capillaries. (a) Schematic view of the assembly. The direction of the flow through the capillaries is indicated by the arrows. (b) Scanning electron microscopy (SEM) image of the device (top view). The channels, spacers, top graphite and edge of the hole are indicated in the figure. Figure adapted from Ref. [29].

was shown that functionalized graphene, i.e., graphene oxide membranes can block different compounds and can perform liquid/liquid and gas/liquid separation [21]. An investigation on water confined in graphene nanocapillaries is conducted in Chapters 5 and 6.

1.2 Water

Water is abundant and essential for chemical processes in nature. It has been extensively studied and several anomalies in the properties of water have been uncovered, such as density, viscosity, phase and diffusive anomalies. However, the principles of the interactions of water molecules and its consequences are still not fully unveiled and this understanding is essential to develop new techniques for water filtration and for the study of biological processes. As this thesis also concerns the study of water under specific conditions, some characteristics and properties of water related to the scope of this work are discussed below.

1.2.1 Phase diagram

Water exhibits different phase structures depending on specific conditions, yielding a complex phase diagram shown in Fig. 1.6. Several triple points and possibly two critical points can be observed, although the critical point in

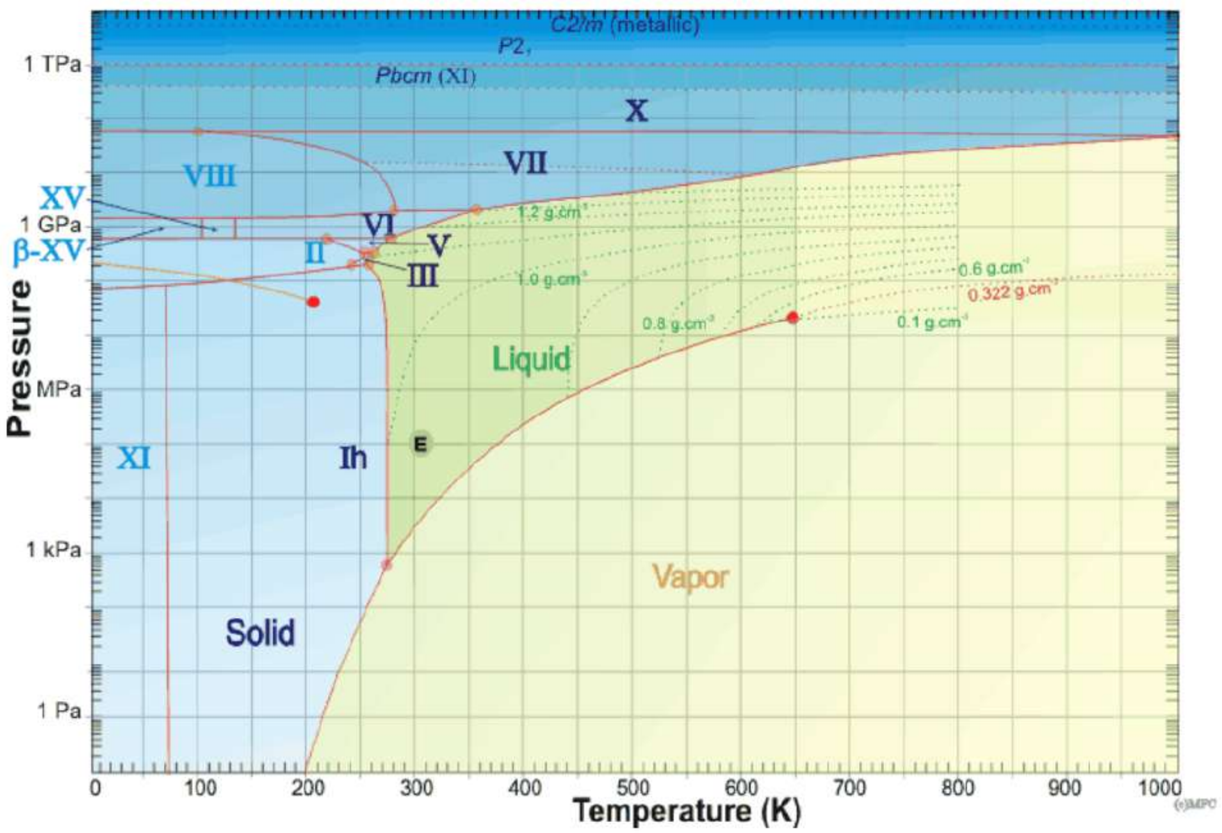

FIGURE 1.6. Water phase diagram. Figure adapted from Ref. [34].

the ice phase, which corresponds to low and high-density forms of amorphous ice, is still a matter of debate [34]. The letter “E” in the diagram of Fig. 1.6 indicates the typical temperatures and pressures on Earth, where water is mainly found in its liquid state unless cooled below 0 °C or heated above 100 °C, when it becomes solid or gaseous, respectively.

Many different ice structures have been reported depending on the conditions of temperature and pressure [34]. Those structures are indicated by roman numerals in Fig. 1.6. Most phase boundaries between ices that share phase boundaries with the liquid phase are parallel to the temperature axis, indicating a density-driven phase transformation, while the entropy-driven phase transformations are denoted by the phase boundaries parallel to the pressure axis. The ice phases that share phase boundaries with liquid have disordered H-bond network, while those with ordered H-bonds are mostly found at lower temperatures.

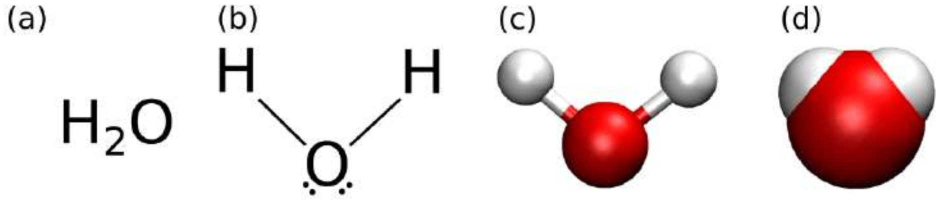

FIGURE 1.7. Water representations. (a) Molecular formula. (b) Structural formula based on Lewis dot structures. (c) Ball and stick model. (d) Space-filling model.

1.2.2 Molecular structure

Water is a V-shaped molecule with the molecular formula H_2O and consists of two hydrogen atoms connected to an oxygen atom. The connections between the atoms are formed by O-H covalent bonds, i.e., the atoms share electron pairs, forming electron clouds. In the case of water, the V-shape is a consequence of the tetrahedral distribution around the oxygen nucleus of the electron clouds formed by the shared electron pairs and the oxygen lone pairs. Therefore, the molecular bent geometry consists of two O-H bonds forming an angle of 104.5°.

Another consequence is the polarity of water. The electrons are strongly attracted by the oxygen nucleus with respect to the hydrogen nuclei, due to the larger number of positive charges on the former. Therefore, the hydrogen atoms carries a slightly positive charge while the charge carried by the oxygen atom is slightly negative. The V-shape causes then the centers of positive and negative charge not to coincide, resulting in a molecular dipole moment pointing from the center of the negative charge (oxygen atom) towards the center of the positive charge (midpoint between the two hydrogens). The existence of this electric dipole moment on the molecule causes the polar nature of water, that allows, e.g., the water molecules to be actuated by applied electric fields.

Several representations for the water molecule have emerged with time, each one evidencing specific features. Fig. 1.7 shows some of them. The most simple, shown in panel (a), is the molecular formula. Panel (b) shows a structural formula inspired by Lewis dot structures, where the V-shape of

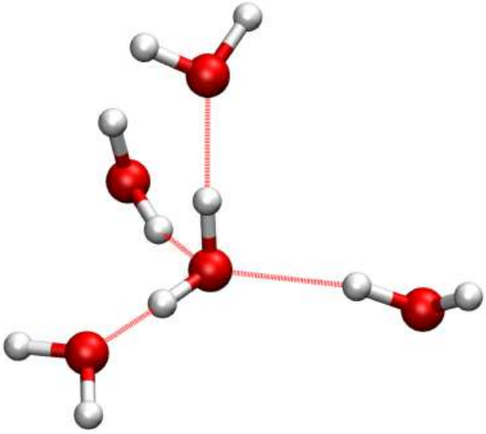

FIGURE 1.8. Four hydrogen bonds (red lines) formed by a water molecule and its surrounding water neighbors.

the molecule is emphasized, the atoms are represented by their chemical symbol, lines represent the bonds between the atoms and the dots represent the lone electron pairs. The ball-and-stick model is shown in panel (c), where the atoms are represented by spheres of different colors that are connected by rods, representing the bonds. In the representation shown in panel (d), the so-called space-filling model, the radii of the spheres representing the atoms are proportional to the van der Waals atomic radii in the same scale as the atom distances. In this case, the bonds are not shown and the rotund shape of the molecule is revealed.

1.2.3 Hydrogen bonds

Several of the unique properties of water, such as density anomalies, high surface tension and capillary action, have the hydrogen bond (H-bond) network as their primary reason. H-bonds occur when a hydrogen atom is attracted by two other atoms, acting as a bond between them. In the case of water, the hydrogen atoms of a molecule are attracted by the oxygen atoms of the neighboring molecules. They are medium strength bonds with lifetime around 1 ps that continuously form and break. The nature of the H-bonds, as well as effects of pressure, temperature and quantum effects have been intensively studied by atomistic simulations [35–37].

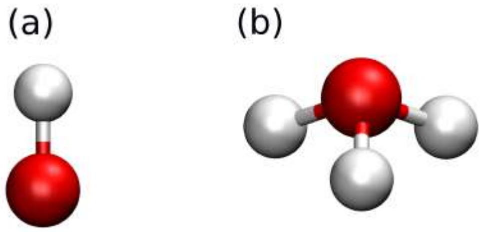

FIGURE 1.9. Structure of the water ions. (a) Hydroxide (OH^-. (b) Hydronium (H_3O^+).

Due to its polarity, a water molecule can form up to four H-bonds, i.e. donating two H-bonds due to their own hydrogen atoms and accepting two other H-bonds due to the hydrogen atoms of the neighboring water molecules. The four H-bonds tend to arrange themselves tetrahedrally, as shown in Fig. 1.8. The strength of the H-bonds is strongly related to the ordering of water molecules. In general, stronger bonds result in more ordered and static structures. A H-bond is strongest when the two water molecules are closer than 3 Å and the three atoms forming the bond are aligned. While the tetrahedral arrangement of H-bonds is a main key in producing the crystalline structure found in ice, it might appear only locally in liquid water [38]. In the latter, water molecules separated by large distances can be connected by hydrogen-bonded chains [39].

1.2.4 Water ionization

Water dissociation, or self-ionization, is very unlikely. Still, the electrical conductivity found in pure water indicates that those events are constantly occurring. The recombination process, however, is among the fastest chemical reactions known [40]. The ions have a crucial role in chemistry and aqueous solutions and determine the pH of water, which simply describe the H_3O^+ concentration and the acidity or basicity of a solution. Due to their short lifetime, however, the mechanisms of water self-ionization and recombination processes have been extensively investigated through molecular dynamics simulations [41–43].

The process of self-ionization of water is believed to occur due to the interplay among electric field fluctuations between neighboring molecules, thermal effects, favorable localized arrangements of hydrogen bonds and quantum effects. The dissociation of water can be characterized by a break in a O-H bond and consequent deprotonation of a water molecule, H_2O, forming the hydroxide ion, OH^-, and subsequent protonation of another water molecule, forming the hydronium ion, H_3O^+, i.e.

$$2\,H_2O \longrightarrow OH^- + H_3O^+.$$

While the OH^- molecule is linear, H_3O^+ exhibits a flattened trigonal pyramidal structure, as shown in Fig. 1.9.

Depending on the local H-bond network, once formed, H_3O^+ and OH^- either rapidly recombine, after 20 ps, or in rare situations separate and independently hydrate, forming H-bonds with neighboring water molecules. The diffusion of the ions is known to be much faster than those of neutral water molecules, following the order $H_3O^+ > OH^- > H_2O$. The fast diffusion is due to the combination of vehicular diffusion and proton transfer processes. The latter follows the so called Grotthuss hopping mechanism, i.e., the excess proton hops from one molecule to the other mediated by the H-bonds until a recombination occurs [44].

1.2.5 Electric effects

The polar nature of water enables electric fields to partially align water molecules. Under different conditions and strength of the electric field, ice formation, melting and even water dissociation have been reported [45–48]. Due to the presence of water ions, electric currents can induce electrolysis, producing O_2 and H_2 [49]. A good control of the orientation of water molecules and position of ions can be achieved by using metallic electrodes [50].

The electric field acts anisotropically in the H-bond network, i.e., strengthening the H-bonds parallel to the field, while weakening H-bonds orthogonal to the field. Therefore, the structural changes in water are caused by H-bond strengthening, bending or breaking. Electric effects on water also include reduction of translational and rotational motions, changes in the O−H bond

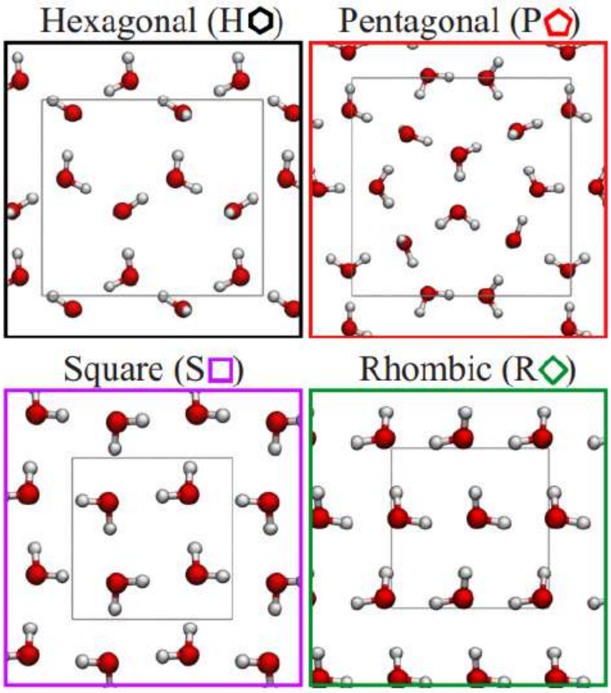

FIGURE 1.10. Different 2D ice structures of confined water. Figure adapted from Ref. [51].

length and H−O−H bond angle, as well as vibrational frequencies and dissociation energy, depending on the relative orientation of the water molecule with respect to the electric field and the strength of the applied field [34].

1.2.6 Confinement

The increasing demand of novel technologies to surpass water scarcity as well as the development of graphene based devices suitable for water desalination have raised the attention to the study of confined water. If the properties of bulk water are already very unique, when confined in nanoscale regions water presents completely distinct structural and dynamical properties. Therefore, the study of such properties can shed light upon fast flow and nanofluidics for applications in water desalination technologies, as well as ion channel flow, which is relevant to biological processes.

When in confinement, the structure of the hydrogen bond network is affected by the limited space and by the nature of the confining walls, yielding structural changes as well as different response to external effects. Typically, water molecules inside graphene nanochannels are ordered and its microscopic structure have been extensively studied [46, 52–55]. Theoretical studies on water confined in graphene nanocapillaries have reported distinct 2D water structures for different applied pressures and channel heights [51, 56] (see Fig. 1.10).

The effects of pressure and electric field on water confined in a graphene nanocapillary will be further explored in Chapter 5. Besides, in Chapter 6 ionized water inside the graphene nanochannel and the effects of confinement on the structural and dynamical properties of the ions will be investigated.

1.3 Applied electric field and polarization

The actuation of real systems by an applied electric field is due to the presence of charge and polarization of the system. The polarization P is defined as the dipole moment p per unit volume, where

$$\vec{p} = q\vec{r}, \tag{1.1}$$

where q and $\vec{r}$ is the charge and position of the dipole.

The local electric field at an atom normally differs from the applied electric field. In fact, it is composed by the external applied field and the sum of the field from the dipoles in the system, where the electric field at a point $\vec{r}$ from a dipole moment $\vec{p}$ is given by

$$\vec{E}(\vec{r}) = \frac{3(\vec{p}\cdot\vec{r})\vec{r} - r^2\vec{p}}{4\pi\epsilon_0 r^5}, \tag{1.2}$$

where ϵ_0 is the vacuum permittivity.

The local electric field relates to the dipole moment through the polarizability α:

$$\vec{p} = \alpha\vec{E}. \tag{1.3}$$

The total polarizability can be separated into three parts: electronic, ionic and dipolar. The electronic contribution is due to the displacement of the negative electron shell with respect to the positive nucleus when an electric field is applied. In the case that ions are present in the system, the ionic contribution appears with the displacement of charged ions. The dipolar polarizability arises from polar molecules such as H_2O that already present permanent electric dipole moment, in which case the applied electric field changes the orientation of the dipole moments of the molecules.

At high frequencies, i.e., in the visible and ultraviolet range (10^{14} – 10^{17} Hz), the dipolar and ionic contributions are negligible due to the inertia of the molecules and ions and the electronic contribution dominates the polarizability. The frequency dependence of the electronic polarizability of an electron bound harmonically to an atom with a resonance frequency ω_0 can be obtained by classically treating the system as a harmonic oscillator. Considering the local electric field as $E_{\mathrm{loc}} \sin \omega t$, the equation of motion reads:

$$m \frac{\mathrm{d}^2 x}{\mathrm{d}t^2} + m\omega_0^2 x = -eE_{\mathrm{loc}} \sin \omega t. \tag{1.4}$$

For a displacement $x = x_0 \sin \omega t$, from Eq. (1.4) one has:

$$x_0 = -\frac{eE_{\mathrm{loc}}}{m(\omega_0^2 - \omega^2)}. \tag{1.5}$$

Since the dipole moment has an amplitude $p_0 = -ex_0$, from Eq. (1.3) the electronic polarizability is given by:

$$\alpha_{(\mathrm{electronic})} = \frac{e^2}{m(\omega_0^2 - \omega^2)}. \tag{1.6}$$

However, in the case of lower frequencies and time-independent uniform applied electric fields, the dipolar contribution must prevail and the dipoles rotate to align with the electric field due to the generated torque

$$\vec{\mathscr{T}} = \vec{p} \times \vec{E}, \tag{1.7}$$

caused by the opposing forces acting on the two dipole charges with opposite signs. This is the case of water polarization under applied electric fields in Chapter 5.

1.4 Organization of the thesis

This thesis is divided in three main parts organized as follows.

Part I – Introduction

This initial part gives an overview of the general aspects and motivations of the thesis.

Chapter 1 presented a general introduction to the properties and applications of carbon-based materials, in specific graphene and carbon nanotubes, are presented. Hereafter, the properties of water and the effects of confinement are stated.

Chapter 2 gives a brief overview of the theoretical methods relevant to obtain the results presented in this thesis. In particular, atomistic molecular dynamics simulations are discussed.

Part II – Decorated Carbon Nanotubes

The second part of the thesis focus on the synthesis and potential applications of hybrid devices composed of carbon nanotubes and metallic nanoparticles.

In *Chapter 3*, the adsorption of metallic nanoparticles on a carbon nanotube is investigated. The nanoparticle migration and coalescence mechanisms, as well as self-diffusion and size are discussed. The nanoparticle properties are linked to the structural properties of the carbon nanotube, i.e., chirality and defects.

In *Chapter 4*, a carbon nanotube decorated with a metallic nanoparticle is subjected to an external electric field. The sensing ability of such hybrid device is investigated through field-induced deformations and unconventional 2D vibrations. The effects of external and internal properties on the resonance frequency are also reported.

Part III – Confined Water

In *Chapter 5*, water confined between two graphene sheets is subjected to an external electric field. Two different systems, i.e., a periodic and an open system are investigated and structural changes due to the channel size, lateral pressure and electric field are investigated.

Chapter 6 expands the study of confined water in graphene nanochannels to the structural and dynamical properties of the water ions. The solvation and recombination processes of hydronium and hydroxide are investigated for different channel heights.

Finally, in *Chapter 7* there are concluding remarks of the study covered in this dissertation and the outlook to further research topics.

CHAPTER 2

MOLECULAR DYNAMICS SIMULATIONS

Molecular dynamics (MD) is the simulation of the motion of interacting particles, atoms and/or molecules, which are classically treated following Newton's equations of motion. MD simulations reveal not only the configuration space, but also the phase space of the system. The system dynamics is calculated by knowing the initial conditions and interaction forces. Considering the complexity of a real system, MD relies on a model for the real system which results matches the real observations. Although implemented by using modern computing power, the first MD methods were developed before the invention of the computer [57]. Nowadays, MD methods can be separated in different classes, depending on how the forces describing the interactions in the system are modelled.

In *ab initio* MD methods, or first-principles MD [58], the forces acting on the particles in a system are derived from quantum-mechanical calculations of electronic energies. Most of the *ab initio* methods are based on the Born-Oppenheimer approximation, where one of the most commonly applied methods is the Car-Parrinello (CP) MD [58]. CPMD was developed in 1985 and is considered the start of *ab initio* MD simulations. Although highly accurate, quantum-mechanical simulations are limited to only a few hundreds of atoms, due to its computational cost.

On the other hand, classical MD is based on inter-atomic forces modelled by empirical or semi-empirical potential functions, obtained by fitting against experiments or quantum-mechanical calculations. The absence of an explicit treatment of the quantum nature of electrons in classical MD yields a computationally cheap method able to simulate systems with millions of atoms. However, since MD simulations are performed by using an approximate Hamiltonian, usually this scheme is less accurate than *ab initio* methods.

In this thesis, different systems of thousands of particles were simulated. Therefore, classical MD simulations were the most employed method in the studies here presented. The main aspects of this method are described in this chapter.

2.1 Initial conditions

Molecular Dynamics simulations start with a suitable choice of initial positions and velocities for all particles in the system and their corresponding degrees of freedom: $(\vec{r_1}(0), \vec{r_2}(0)), \ldots, \vec{v_1}(0), \vec{v_2}(0), \ldots)$. Typically, for a system of N particles in 3 dimensions, $3N$ positions and $3N$ velocities are assigned. A fast convergence and reliable results depend on a good initial guess. When simulating atoms and/or molecules, one may also need to set the mass and charge of each particle in the system.

In order to set the initial position of the atoms, there are different approaches depending on the system of interest. The initial configuration can be a crystalline lattice, an idealized or approximate geometry or even randomly distributed particles, although care must be taken in order to avoid core overlapping. If available, the initial configuration can also be taken from experiments, e.g., from X-ray or NMR.

When considering a system in thermal equilibrium, the initial velocities of the particles must follow the Maxwell-Boltzmann distribution at the chosen initial temperature T:

$$f(v) = \left(\frac{m}{2\pi k_B T}\right)^{3/2} 4\pi v^2 \exp\left(-\frac{mv^2}{2k_B T}\right), \tag{2.1}$$

where v is the magnitude of the velocity vector $\vec{v}$, m is the mass of the particle and k_B is the Boltzmann's constant. The average kinetic energy is therefore given by

$$\langle \frac{1}{2} m v^2 \rangle = \int_0^\infty \frac{1}{2} m v^2 f(v) dv = \frac{3}{2} k_B T, \tag{2.2}$$

which yields an operational definition of the temperature.

In order to avoid a nonzero net momentum of the system, the velocities are rescaled, i.e.,

$$\vec{v}(0) \rightarrow \vec{v}(0) - \frac{\sum_i^N m_i \vec{v}_i(0)}{m_i N}. \tag{2.3}$$

2.2 Integration

The basis of MD simulations is the discretization and numerical integration of Newton's equation of motion:

$$m_i \ddot{\vec{r}}_i(t) = \vec{F}_i(t), \quad i = 1, \ldots, N \tag{2.4}$$

where N is the total number of particles, $\vec{r}_i(t)$ and $\vec{F}_i(t)$ are the position vector and force of particle i at time t, respectively. The force $\vec{F}_i$ depends on the position of the other particles in the system and on possible external factors, e.g., external drives. The interaction between particles is usually taken as pairwise additive, where higher order interactions need to be considered in an effective pair potential U, which relates to the pairwise force so that:

$$\vec{F}_{ij} = -\frac{\partial U(r_{ij})}{\partial r_{ij}}. \tag{2.5}$$

A proper discretization is essential for a reliable and accurate MD simulation and is controlled by the time-step Δt, i.e., the time interval between two consecutive evaluation of the forces. A good choice of Δt should be one that is not too small, as the calculation of forces is the most time-consuming task in a MD simulation, but also not too large, to avoid discretization errors. Typical time-steps in MD simulations are of the order of femtoseconds.

One of the simplest and most widely employed integrators is the velocity Verlet algorithm [59]. Eq. 2.4 can be reduced to:

$$\dot{\vec{r}}_i(t) = \vec{v}_i(t) \tag{2.6}$$

$$\dot{\vec{v}}_i(t) = \frac{\vec{F}_i(t)}{m_i}. \tag{2.7}$$

Considering a small Δt, a Taylor expansion of the particle coordinate yields

$$\vec{r}_i(t+\Delta t) = \vec{r}_i(t) + \vec{v}_i(t)\Delta t + \frac{\Delta t^2}{2}\vec{a}_i(t) + \mathscr{O}(\Delta t^3), \tag{2.8}$$

where $\vec{v}_i = \dot{\vec{r}}_i$ and $\vec{a}_i = \vec{F}_i/m_i = \dot{\vec{v}}_i =$ are the velocity and acceleration of the particle, respectively.

Similarly, for the particle velocity,

$$\vec{v}_i(t+\Delta t) = \vec{v}_i(t) + \vec{a}_i(t)\Delta t + \frac{\Delta t^2}{2}\vec{b}_i(t) + \mathscr{O}(\Delta t^3), \tag{2.9}$$

where $b_i(t) = \ddot{\vec{v}}_i(t)$, that can be obtained in terms of known quantities by expanding $\vec{a}_i$:

$$\vec{a}_i(t+\Delta t) = \vec{a}_i(t) + \vec{b}_i(t)\Delta t + \mathscr{O}(\Delta t^2), \tag{2.10}$$

yielding

$$\frac{\Delta t^2}{2}\vec{b}_i(t) = \frac{\Delta t}{2}[\vec{a}_i(t+\Delta t) - \vec{a}_i(t)] + \mathscr{O}(\Delta t^3). \tag{2.11}$$

Then, the expression for the particle velocity becomes

$$\vec{v}_i(t+\Delta t) = \vec{v}_i(t) + \frac{\Delta t}{2}[\vec{a}_i(t) + \vec{a}_i(t+\Delta t)] + \mathscr{O}(\Delta t^3). \tag{2.12}$$

The velocities are necessary for the calculation of certain physical quantities, e.g., kinetic energy and temperature.

In order to avoid storing accelerations at two different time steps, the velocity Verlet algorithm is implemented by the following steps:

- From $\vec{r}_i(t)$, $\vec{v}_i(t)$ and $\vec{a}_i(t)$, the positions $\vec{r}_i(t+\Delta t)$ are updated:

$$\vec{r}_i(t+\Delta t) = \vec{r}_i(t) + \vec{v}_i(t)\Delta t + \frac{\Delta t^2}{2}\vec{a}_i(t). \tag{2.13}$$

- The velocities are calculated at an intermediate time-step:

$$\vec{v}_i(t+\Delta t/2) = \vec{v}_i(t) + \frac{\Delta t}{2}\vec{a}_i(t). \tag{2.14}$$

- From $\vec{r}_i(t+\Delta t)$, the forces and hence the accelerations $\vec{a}_i(t+\Delta t)$ are calculated.

- Finally, the velocities $\vec{v}_i(t+\Delta t)$ are updated:

$$\vec{v}_i(t+\Delta t) = \vec{v}_i(t+\Delta t/2) + \frac{\Delta t}{2}\vec{a}_i(t+\Delta t). \tag{2.15}$$

Although very simple, the velocity Verlet method works notably well, with small energy drifts on large time scales due to its time-reversibility and its symplecticity, i.e., it preserves area in the phase space. However, as in any integration algorithm, there are intrinsic integration errors and the prediction given by the velocity Verlet method slightly differs from the exact solution. Nevertheless, the method reproduces a similar dynamics and the numerical trajectories are expected to follow some real trajectories for long time scales and therefore they can be used to investigate statistical properties of the system.

2.3 Thermostat

Molecular dynamics appear as a natural tool to simulate isolated systems where the number of particles, volume and energy are preserved, i.e., equivalent to ensemble averages in the microcanonical (NVE) ensemble. However, most experiments are conducted under constant temperature and, therefore, the most common choice is to simulate a system in equilibrium with a heat bath. This implies either canonical/isochoric-isothermal (NVT) or isothermal-isobaric (NPT) simulations. Therefore, a meticulous approach is needed to balance the conservation of energy and the thermal equilibrium of the system, which is handled by the thermostat.

In molecular dynamics simulations, the temperature specifies the thermodynamic state of the system and relates to the microscopic description of simulations through the kinetic energy. Since at thermal equilibrium Eq. (2.2) holds for the average kinetic energy of a particle, the instantaneous temperature of a system of N particles at a simulation time t can be calculated as

$$T(t) = \frac{1}{3k_B N}\sum_{i=1}^{N} m_i v_i^2(t). \tag{2.16}$$

For finite canonical systems, the temperature T fluctuates, since the kinetic energy fluctuates and one should average over many fluctuations in order to have an accurate estimate of the temperature. In order to keep the average temperature constant, a thermostat is employed to add or remove energy from the system.

A reliable thermostat should sample the canonical distribution (or at least yield reliable results for sufficiently large times), do not perturb the particle dynamics significantly and be straightforward to implement. One of the most chosen and also implemented in this thesis is the Nosé-Hoover thermostat, which is rather simple to implement and for which the dynamics of all degrees of freedom are deterministic and time-reversible. This approach was originally developed by Nosé and later improved by Hoover [60, 61]. It is considered a “gentle” thermostat, as the perturbing force acting on each particle in the system acts only along the direction of motion of that particle. The heat bath is considered as an integral part of the system by extending the Hamiltonian H of the system:

$$H_{NH} = H + \frac{p_s^2}{2Q} + gk_BT \ln s, s \tag{2.17}$$

where s, p_s and Q are the position, momentum and fictitious mass of the heat bath, respectively, and $g = (3N+1)$ is the number of degrees of freedom of the extended system, i.e. N particles +1 new degree of freedom due to the heat bath. The magnitude of Q determines the coupling between the real system and the heat bath and relates to the temperature fluctuations. A very small value of Q leads to high frequency oscillations of energy, while a very large value would lead to poor temperature control.

The equation of motion (Eq. (2.4)) is then updated and velocities rescaled:

$$m_i \ddot{\vec{r}}_i(t) = \vec{F}_i(t) - \zeta m_i \vec{v}_i, \tag{2.18}$$

where $\zeta = \dfrac{\partial \ln s}{\partial t}$ and

$$\frac{d\zeta(t)}{dt} = \frac{1}{Q}\left[\sum_{i=1}^{N} \frac{m_i \vec{v}_i^2}{2} - \frac{3N+1}{2} k_B T\right]. \tag{2.19}$$

2.4 Barostat

Besides constant temperature, most experiments are conducted under constant pressure instead of constant volume conditions. When simulating a system at constant pressure, the volume V of the simulation domain is considered as a dynamical variable that changes during the simulation and the pressure of the system can be calculated by the virial theorem:

$$P = \frac{Nk_BT}{V} + \frac{1}{3V}\sum_{i=1}^{N} \vec{r}_i \vec{F}_i, \tag{2.20}$$

where P is the internal pressure of the system which is in equilibrium with a *pressure bath*, i.e.,

$$\langle P_{(\mathrm{int})} \rangle = P_{(\mathrm{bath})}, \tag{2.21}$$

where $P_{(\mathrm{bath})}$ is the target pressure of the external bath.

More rigorously, the pressure is not a scalar but a tensor $\boldsymbol{P}$ where the tensor element P_{xy} is the force in y direction acting on the surface element with its normal vector in x direction. In isotropic systems, $P = P_{xx} = P_{yy} = P_{zz}$ and the pressure can be expressed as a scalar:

$$P = \frac{\mathrm{Tr}(\boldsymbol{P})}{3}. \tag{2.22}$$

Analog to the Nosé-Hoover thermostat, the Andersen and Nosé-Hoover barostats [62, 63] couple the system with V, which is supposed to mimic the action of a piston of effective mass Q and energy given by:

$$E_{\mathrm{piston}} = \frac{Q\dot{V}^2}{2} + P_{(\mathrm{bath})}V. \tag{2.23}$$

As an extension, the Parrinello-Rahman barostat [64] allow changes in the shape and size of the cell during simulation by describing the simulation cell by three vectors $\vec{a}$, $\vec{b}$ and $\vec{c}$ and defining a matrix $M \equiv \{\vec{a}, \vec{b}, \vec{c}\}$, where the volume of the cell is given by $V = \det M = \vec{a} \cdot (\vec{b} \times \vec{c})$. Therefore, the energy of the fluctuating volume is given by

$$E_{\mathrm{volume}} = \frac{Q}{2}\mathrm{Tr}\left(\frac{dM^T}{dt}\frac{dM}{dt}\right) + P_{(\mathrm{bath})}V. \tag{2.24}$$

2.5 Computation of the system properties

Considering a system in equilibrium, the ergodic hypothesis must hold [65, 66]. In statistical analysis of computational systems, this assumption means that the ensemble average of a thermodynamic property A is equal to its time average:

$$\langle A \rangle = \lim_{t\to\infty} \frac{1}{t} \int_{t_0}^{t_0+t} A(\tau) d\tau, \tag{2.25}$$

where $\langle \ldots \rangle$ denotes the ensemble average and the right-hand-side denotes the integral of A over a typical trajectory from a simulation time t_0 to $t_0 + t$. At equilibrium, the average does not depend on t_0. Equation 2.25 is used in this thesis to compute, e.g., deflections of a carbon nanotube in Chapter 4, and density profile of water/ions in Chapters 5 and 6.

From molecular dynamics simulations, structural properties of a system can be investigated. Such information is crucial to understand, e.g., experimental results on disordered systems like liquids. Despite the absence of a crystal structure, there is always some structural order in such systems. To evaluate its extent, radial distribution functions (RDFs) $g(r)$ are very useful, since it describes the variation of density as a function of distance r from a reference particle, i.e., the probability of finding a particle at a distance r from the reference particle. Computationally, this can be calculated as

$$g(r) = \frac{n(r)}{\rho 4\pi r^2 \Delta r}, \tag{2.26}$$

where $n(r)$ represents the number of particles within a distance $r + \Delta r$ of the reference particle (see Fig. 2.1(a)) and ρ is the number density. The positions of the first and second peak in the RDF give the average inter-atomic distance between nearest and next nearest neighbors, respectively, from which the average bond length and angle can be evaluated (see Fig. 2.1(b)). Equation 2.26 is implemented to evaluate the structural properties of water and water ions under confinement in Chapters 5 and 6.

Many other structural and dynamical properties can be evaluated from molecular dynamics simulation [67]. For example, the microscopic mean-squared distance $\langle r^2(t) \rangle$ over which the particles move in a time interval t can be related to the macroscopic diffusion coefficient D:

$$D = \frac{1}{2d} \lim_{t\to\infty} \frac{\mathrm{d}}{\mathrm{d}t} \langle r^2(t) \rangle, \tag{2.27}$$

where d is the dimensionality of the system. In Chapter 3, the nanoparticle diffusion is calculated by using Eq. 2.27.

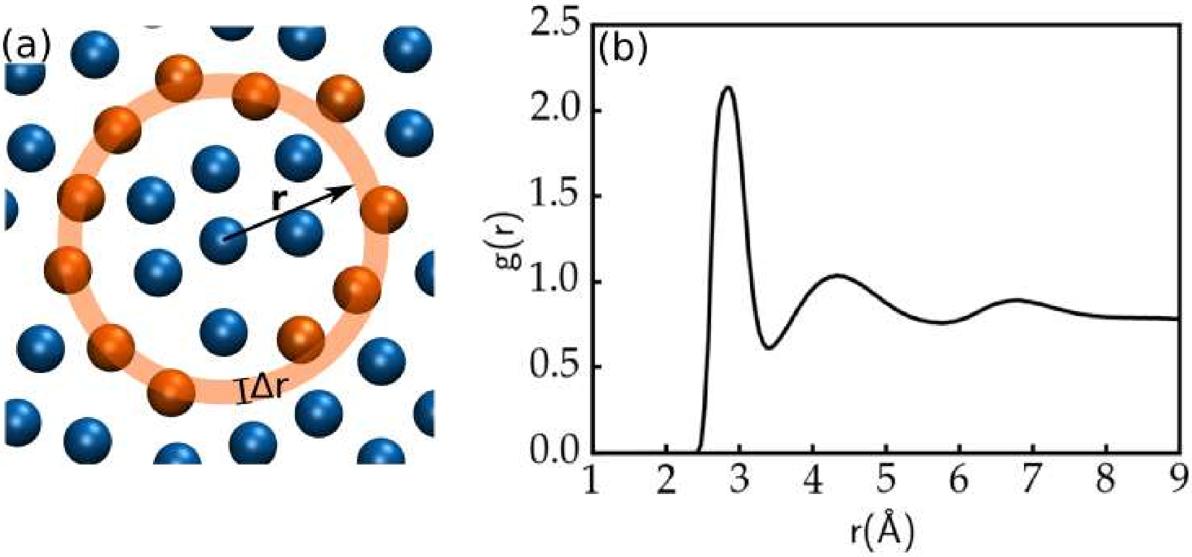

FIGURE 2.1. Radial distribution function (RDF). (a) Space discretization for evaluation of the RDF. (b) RDF of oxygen atoms in bulk water calculated from MD simulations at 298 K.

2.6 Interaction potentials

A fundamental part of molecular dynamics simulations is the description of the interaction forces between particles, usually based on potential functions [68]. Also called force fields, the potential functions can be obtained, e.g., by fitting against experiments or quantum-mechanical calculations. They are built on the assumption that molecules exhibit a chemical environment dependent behavior and are based on non-bonded and bonded terms. The latter refers to strong interactions formed by ionic, covalent or metallic bonding, where there is an overlap of the electron clouds of interacting atoms. On the other hand, non-bonded terms refer to intermolecular interactions. These weak interactions are due either to permanent dipoles, as in the case of dipole-dipole interction and hydrogen bonding, or to instantaneous dipoles in neighoring atoms caused by a nonuniform electron cloud, giving rise to London dispersion forces.

In general, a force field consists of four components that represent intra- and intermolecular forces, namely:

- two-body term for bond stretching,

- three-body term for bending of the angle formed by two bonds,
- four-body term for rotation around bonds (torsion),
- non-bonded terms due to van der Waals and electrostatic interactions.

Three-body and higher order terms are grouped in the category of many-body potentials, which can include also cross terms. An example of function form is given by:

$$\begin{aligned} V(\vec{r}) &= V_{\text{bond}} + V_{\text{angle}} + V_{\text{torsions}} + V_{\text{non-bonded}} \\ &= \sum_{\text{bonds}} \frac{k_i}{2}\left(l_i - l_{i,0}\right)^2 + \sum_{\text{angles}} \frac{p_i}{2}\left(\theta_i - \theta_{i,0}\right)^2 \\ &+ \sum_{\text{torsion}} \frac{V_n}{2}\left(1 + \cos(n\omega - \gamma)\right) + V_{\text{vdW}} + V_{\text{Coulomb}}, \end{aligned} \tag{2.28}$$

where $l_{i,0}$ and $\theta_{i,0}$ correspond to the reference values of bond and angle, respectively, V_n is a coupling constant, n gives the number of function minima in a bond rotation of 360°and γ is the phase factor determining the position of the minimum value of the torsion angle. V_{vdW} and V_{Coulomb} are non-bonded terms due to van der Waals and electrostatic interactions and will be discussed further. External potentials can be added in the system by means of a single-particle term.

Although the potential described by Eq. (2.28) already contains several coupling constants, higher order terms as well as cross terms can be included if a more sophisticated approach is needed. For example, extra terms with additional coupling constants can be added to have a better approximation of the real interaction and cross terms can be included to reproduce the dependent nature of the atomic bonds, e.g., bond stretching due to a bond angle decrease. The different coupling constants present in a force field need to be fitted against experimental or theoretical/computational data and should consider different aspects of the atoms in the system, such as possible hybridisation states. A function form as Eq. (2.28), however, is not suitable for modelling chemical reactions. In this sense, bond-order potentials that will be discussed further have the advantage of enabling bond formation/breaking and describing different bonding states of an atom by using the same set of parameters.

2.6.1 Lennard-Jones potential

For a system of weakly-interacting atoms or rigid molecules, interaction potentials consisting only of non-bonded terms can be used. In this regard and due to its simplicity and reduced computational demand, the Lennard-Jones (LJ) potential [69] is widely used in computing simulations to describe van der Waals interactions, i.e., distance-dependent interactions between atoms or molecules that includes London dispersion forces and the Pauli exclusion principle. The method is described by the following equation:

$$V_{LJ}(r_{ij}) = 4\epsilon \left[\left(\frac{\sigma}{r_{ij}} \right)^{12} - \left(\frac{\sigma}{r_{ij}} \right)^{6} \right], \tag{2.29}$$

where r_{ij} is the distance between particles i and j, ϵ is a measure of how strongly the two particles interact to each other and σ is the distance at which the potential energy between the particles is zero.

The LJ parameters ϵ and σ can be calculated theoretically, empirically or by first principles [70–72]. New LJ parameter values can be obtained by using the Lorentz-Berthelot combination rules, i.e., for given particles A and B with corresponding LJ parameters, ϵ_{AA}, σ_{AA} and ϵ_{BB} and σ_{BB}, the LJ parameters for the interaction between particles A and B will be given by $\epsilon_{AB} = \sqrt{\epsilon_{AA}\epsilon_{BB}}$ and $\sigma_{AB} = (\sigma_{AA} + \sigma_{BB})/2$. Fig. 2.2 shows the LJ potential for pairs of atoms of different elements.

Equation (2.6.1) was developed considering that the interaction between two particles is repulsive at short ranges and attractive at long ranges. The attractive term ($\sim r_{ij}^{-6}$) describes long-range attraction due to London dispersion, which occurs when instantaneous dipoles are formed due to the redistribution of the electron densities of two adjacent atoms. The repulsive term ($\sim r_{ij}^{-12}$) refers to short range Pauli exclusion principle, which prevents the collapse of molecules due to am inter-atomic repulsion at very small distances caused by the overlap of electron density distributions of atoms. The Lennard-Jones potential is used as one of the non-bonded terms in force fields implemented in this thesis. Besides, in Chapters 3, 4 and 5, the LJ potential models the interaction between carbon atoms and other species.

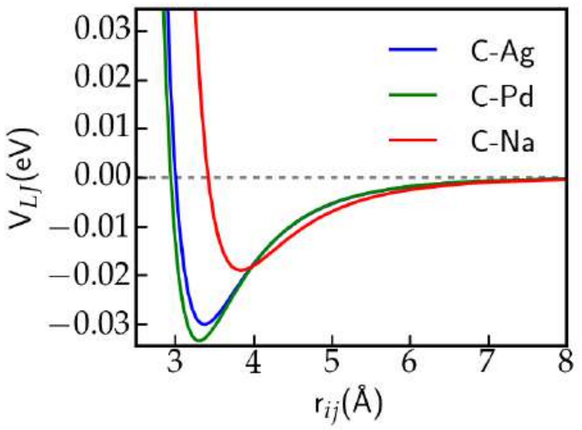

FIGURE 2.2. Lennard-Jones potential for pair of atoms of different elements.

2.6.2 Electrostatic interactions

When electrostatic charges are present, as it is the case in Chapters 4, 5, and 6, the Coulomb potential must be included in the interaction between particles:

$$V_{\text{Coulomb}}(r_{ij}) = \frac{q_i q_j}{4\pi\epsilon_0 r_{ij}}, \tag{2.30}$$

where ϵ_0 is the vacuum permittivity, q_i is the charge of the charged site i and r_{ij} is the distance between the charged sites i and j. Suitable charges are obtained from experimental or theoretical data.

2.6.3 Rigid water models

Developing a model that successfully predicts the physical properties of water have proved to be challenging. Several attempts of describing water and its behavior have been made and over a hundred water models have been proposed. Among those, rigid water models are the simplest water models and are based on non-bonded interactions, which are implicitly considered by constraints. The potential energy of such models consists of an electrostatic interaction modeled by the Coulomb's law and dispersion and repulsion forces

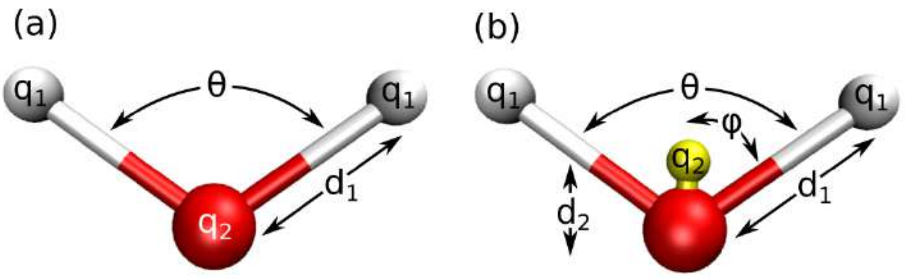

FIGURE 2.3. Molecular structure of water models. (a) Three-site model with charge sites q_1 (q_2) coinciding with H (O) atoms represented in white (red). (b) Four-site model with a dummy atom (yellow) close to the Oxygen (red).

represented by the Lennard-Jones potential. The interaction between two molecules a and b is then described by:

$$E_{ab} = \sum_{i}^{n_a}\sum_{j}^{n_b} \frac{q_i q_j}{4\pi\epsilon_0 r_{ij}} + 4\epsilon\left[\left(\frac{\sigma}{r_{OO}}\right)^{12} - \left(\frac{\sigma}{r_{OO}}\right)^{6}\right], \tag{2.31}$$

where $i,\ldots,n_a$ are the charged sites of molecule a and r_{OO} is the distance between the two oxygen atoms, as in most water models there is only one LJ site corresponding to the oxygen atom.

The different rigid models can be distinguished by the number of interaction sites, with the most commonly applied being 3-site or 4-site models. Three-site models have the charged sites corresponding to the three atoms of the water molecule, as depicted in Fig. 2.3(a). In 4-site models, a negatively charged dummy atom is added near the oxygen atom along the bisector of the HOH angle ($\phi = \theta/2$ in Fig. 2.3(b)). Including the dummy atom improves the electrostatic distribution around the water molecule. In most of the 3-site and 4-site models, the O−H distance and H−O−H angle matches the molecular structure of water. A very common choice is the TIP4P model [73], which is a 4-site model widely implemented in computational chemistry software packages and is used in this thesis in Chapter 5 to model water molecules. The parameters used in this thesis are shown in Table 2.1 [73].

Table 2.1: TIP4P parameters [73].

Parameter	**Value**
O mass	15.9994 g
H mass	1.008 g
O charge	-1.040 e
H charge	0.520 e
r_{OH}	0.9572 Å
θ_{HOH}	104.52°
$\overline{OM}$	0.15 Å
ϵ_{OO}	0.1550 eV
σ_{OO}	3.1536 Å
ϵ_{OH}, ϵ_{HH}, σ_{OH}, σ_{HH}	0.0
Coulombic cutoff	8.5 Å

2.6.4 Bond-order potentials

Classical empirical force fields can be employed with low computational cost to simulate large-scale systems, with reliable results when simulating systems near equilibrium, with fixed charges, as in the study of, e.g., computer-aided drug discovery and polymer research. However, when the local chemical environment becomes relevant, bond-order potentials appear as an alternative able to describe, with the same set of parameters, several different bonding states of an atom and even chemical reactions, depending on the employed method. The bond-order potentials implemented in this thesis are discussed below.

2.6.4.1 Embedded Atom Method (EAM)

Embedded atom method (EAM) is a semi-empirical inter-atomic potential developed to overcome the inability of standard force fields to adequately reproduce the properties of metal systems [74]. This was achieved by including an approximation to many-atom interactions. The principle of the EAM is to assume that the total-electron density in a metal can be approximated by the linear superposition of the contribution of each atom [75]. Then, the electron density around an atom is the sum of the self density contribution and the electron density from the surrounding atoms. The embedding energy is defined as function of the background electron density and the atomic species. Additionally, the electrostatic contribution of the core-core overlap is considered. These assumptions lead to an interaction potential with a computational demand similar to the one required by pairwise potentials.

The total energy can be approximated as:

$$E_{EAM} = \sum_i F_i\left(\rho_{h,i}\right) + \frac{1}{2}\sum_i \sum_{j\neq i} \phi_{ij}\left(r_{ij}\right), \tag{2.32}$$

where $\rho_{h,i}$ is the host electron density at atom i due to the other atoms in the system, $F_i\left(\rho\right)$ is the energy required to embed atom i into the background electron density ρ and $\phi_{ij}\left(r_{ij}\right)$ is the core-core pair repulsion between atoms i and j separated by a distance r_{ij}.

Approximating the electron density as the superposition of the atomic densities, one has

$$\rho_{h,i} = \sum_{j\neq i} \rho_{a,j}\left(r_{ij}\right), \tag{2.33}$$

where $\rho_{a,j}(r)$ is the electron density contributed by atom j. The pair-interaction term is repulsive and can be approximated by the geometric mean of the pair interaction for individual species, being approximated as

$$\phi_{AB}(r) = \frac{Z_A(r)Z_B(r)}{r}, \tag{2.34}$$

where Z_A is the effective charge of an atom of species A, which is constrained to be positive and to decrease monotonically with r. $F\rho$ and $Z(r)$ can be either calculated empirically, by adjusting parameters to fit known experimental data. Fig. 2.4 shows the effective charge $Z(r)$ and the embedding function $F(\rho)$ determined empirically for different metallic elements. They have been determined so as to yield the elastic constants and vacancy-formation energy of each material. In this thesis, the EAM is employed in Chapters 3 and 4 to simulate interactions between metallic atoms composing nanoparticles.

2.6.4.2 Adaptative Intermolecular Reactive Empirical Bond Order (AIREBO) potential

The reactive empirical bond order (REBO) potential [76] was originally developed for modelling chemical vapor deposition of diamond and was later

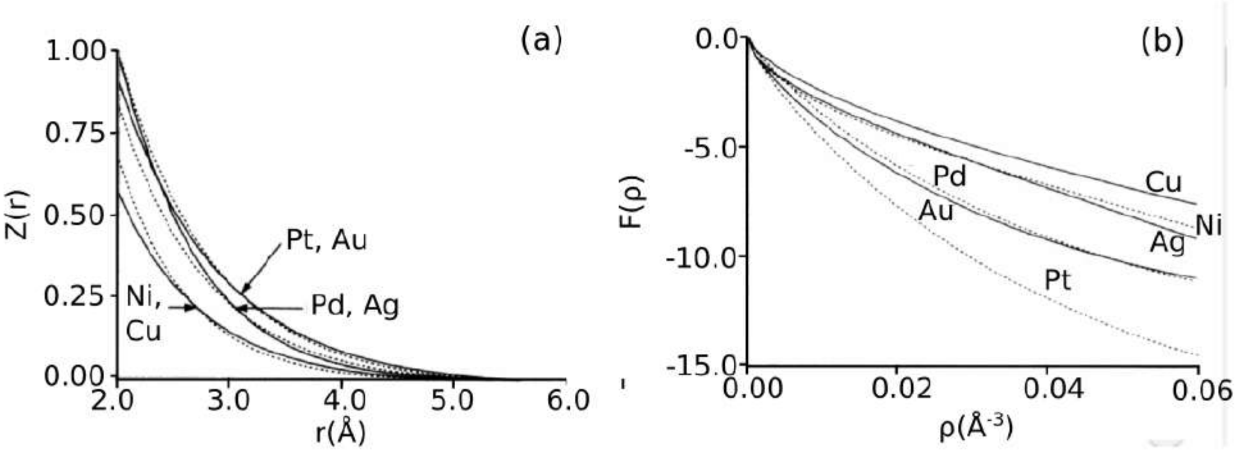

FIGURE 2.4. Components of the EAM potential for different metallic elements. (a) The effective charge $Z(r)$ used to define the pair interaction (see Eq. 2.34). (b) The embedding functions $F(\rho)$ as a function of the background electron density ρ. Figure adapted from Ref. [75].

extended to provide more accurate treatment of energetic, elastic and vibrational properties of solid carbon and small hydrocarbons. However, the absence of dispersion and non-bonded repulsion terms impeded the potential to be used in the case of systems with intermolecular interactions. To circumvent this, the Adaptative Intermolecular Reactive Empirical Bond Order potential (AIREBO) [77] was developed, including an adaptative treatment of non-bonded and torsional interactions to the REBO potential.

The AIREBO potential can be represented by:

$$E^{\mathrm{AIREBO}} = E^{\mathrm{REBO}} + E^{\mathrm{LJ}} + E^{\mathrm{torsion}}, \tag{2.35}$$

where the REBO interaction for a pair of atoms i and j is written as:

$$E_{ij}^{\mathrm{REBO}} = V^{\mathrm{R}}(r_{ij}) + b_{ij} V^{\mathrm{A}}(r_{ij}), \tag{2.36}$$

with the repulsive (V^{R}) and attractive (V^{A}) terms determined by the atom types (carbon or hydrogen) and depending only on the distance r_{ij} between the atom pair, being combined in a ratio defined by the bonding term b_{ij}.

The b_{ij} term specifies the bond order for the interaction between two atoms i and j and accounts for several chemical effects that influences the strength of the covalent bonding interaction, e.g., coordination number, bond angle and hybridisation, which is empirically treated.

In the AIREBO potential, the transition between bonded and non-bonded interactions is controlled by bond-weight terms, which are included in the repulsive V^{R} and attractive V^{A} terms and control the contribution of the REBO interactions, i.e., the REBO contribution is smoothly switched off as the atom pair separation distance exceeds the bond distance.

The intermolecular interactions in the AIREBO potential are modelled with a Lennard-Jones potential (see Eq. (2.6.1)). However, in order to preserve the reactive character of the potential, the LJ interaction is coupled to a smooth switch that controls the LJ contribution depending on: i) the distance between the two atoms in question, ii) the strength of the bonding interaction between them, and iii) the bond network connecting them. This means that the LJ repulsion at short distances will be considered only if the two atoms are not likely to form a chemical bond and they are not vicinal (1-4) neighbors in the same molecule.

The mathematical expression for the LJ interaction between atoms i and j is given by

$$E_{ij}^{\mathrm{LJ}} = S(t_r(r_{ij}))S(t_b(b_{ij}^*))C_{ij}V_{ij}^{\mathrm{LJ}}(r_{ij}) + [1 - S(t_r r_i j)]C_{ij}V_{ij}^{\mathrm{LJ}}(r_{ij}), \tag{2.37}$$

where $S(t)$ is a spline switching function that guarantees that the function and its first derivative are continuous at the endpoints of the switching region. The scaling function $t_r(r_{ij})$ is given by

$$t_r(r_{ij}) = \frac{r_{ij} - r_{ij}^{\mathrm{LJ\ min}}}{r_{ij}^{\mathrm{LJ\ max}} - r_{ij}^{\mathrm{LJ\ min}}}, \tag{2.38}$$

where $\left[r_{ij}^{\mathrm{LJ\ min}}, r_{ij}^{\mathrm{LJ\ max}}\right]$ is the switching region. The $S(t_b(b_{ij}^*))$ term is a bond switch, where the scaling function $t_b(b_{ij})$ is defined analogously to Eq. (2.38). The b_{ij}^* term in Eq. (2.37) slightly differs from the b_{ij} term in Eq. (2.36) and represents an hypothetical b_{ij} evaluated at r_{ij}^{min}. Finally C_{ij} in Eq. (2.37) is a connectivity switch, which accounts for the number of connections of the atoms and excludes the LJ contribution in case the atom pair is connected by a series of three or fewer bonds, in which case the REBO potential satisfactorily describes the pair interaction.

The torsion term in Eq. (2.35) has a different functional dependence as compared to Eq. (2.28), since the reactive nature of the AIREBO potential considers that the relative energies and barries to rotation depend on the chemical environment. Therefore, the torsion potential is chosen so that its symmetry is naturally defined from the local coordination environment and is expressed as:

$$V^{\mathrm{torsion}}(\omega) = \left[\frac{256}{405}\cos^{10}\left(\frac{\omega}{2} - \frac{1}{10}\right)\right], \tag{2.39}$$

where the constants are chosen in order to obtain the expected threefold symmetry for sp^3 carbons. The functional form of V^{tors} reflect the physical symmetries of the repulsion between atoms or bonds that is assumed to be the origin of the torsional potential. The torsional potential is implemented in the AIREBO model in the form:

$$E^{\mathrm{torsion}} = \frac{1}{2}\sum_i \sum_{j\neq i} \sum_{k\neq i,j} \sum_{l\neq i,j,k} w_{ij}(r_{ij}) w_{jk}(r_{jk}) w_{kl}(r_{kl}) V^{\mathrm{torsion}}(\omega_{ijkl}), \tag{2.40}$$

where $w(r)$ is a bond-weight term. The use of bond weights ensures that the torsional energy will be smoothly removed as any of the constituent bonds are broken.

The AIREBO potential is implemented in Chapters 3 and 4 in this thesis to model the interaction between carbon atoms in carbon nanotubes.

2.6.4.3 Reactive Force Fields (ReaxFF)

The ReaxFF is a reactive force field developed in order to describe systems constituted of different atomic species accounting for the formation and breaking of chemical bonds as well as charge polarization [78]. ReaxFF [79] is able to be implemented in molecular dynamics simulations of systems of the order of hundreds of thousands of particles and is based on the concept of bond order to model the particle interactions. A dynamic description of each atomic and molecular interaction makes ReaxFF a method independent of predefined reactive sites. In this way, specifying charges or bonds (constraints) during initialization of the system becomes unnecessary, since they vary dynamically during the simulation depending on the environment. In this way, the method has as its main advantage the ability to describe the dissociation and formation of chemical bonds.

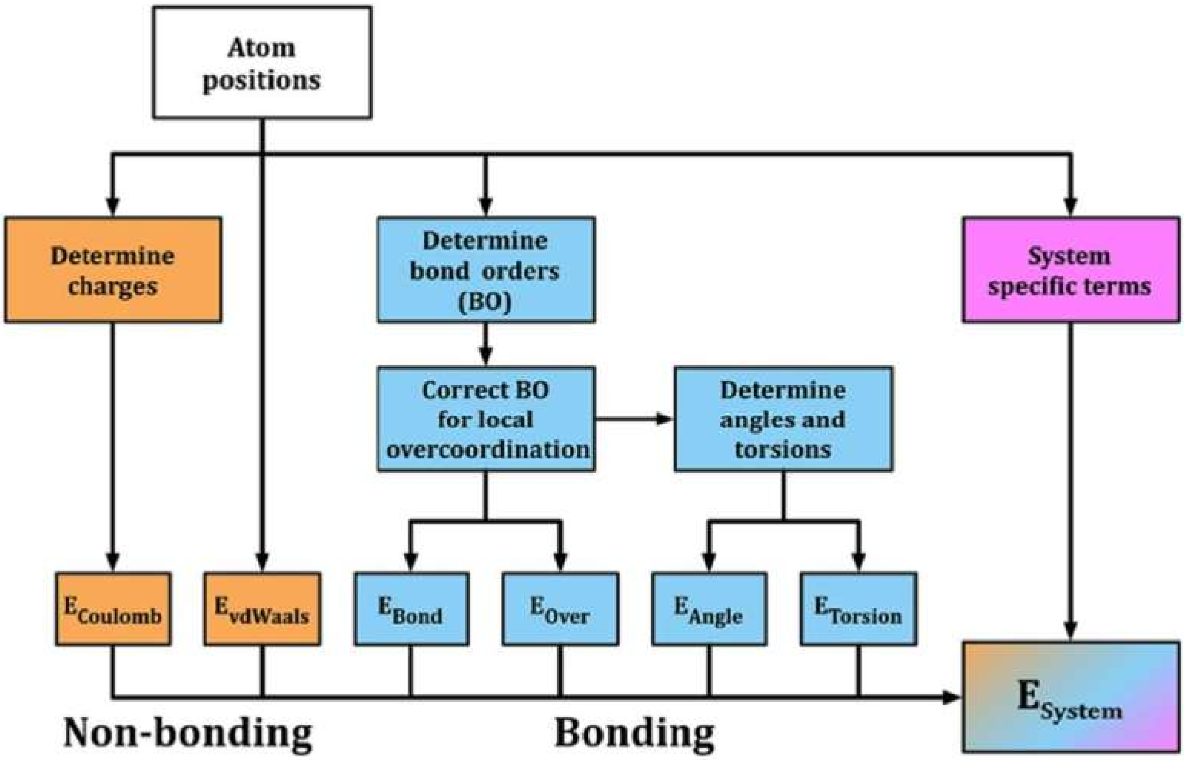

FIGURE 2.5. Overview of the components of the ReaxFF force field. Figure adapted from Ref. [78].

To obtain the ReaxFF force field for a given system, the atomic, bond, angle and torsion properties of each particle are parameterised against experimental data and quantum calculations. In addition, the non-bonded interactions are modelled by van der Waals (LJ) and Coulombic potentials. The energy of the system can be described based on its contributions:

$$E_{\text{system}} = E_{\text{bond}} + E_{\text{over}} + E_{\text{angle}} + E_{\text{torsion}} + E_{\text{vdW}} + E_{\text{Coulomb}} + E_{\text{specific}}, \tag{2.41}$$

where E_{over} is an energy penalty to prevent overcoordination of the atoms and is based on the atomic valency rules, E_{specific} represents specific terms inherent to the system of interest that are otherwise not included. The nature of the other terms have been already discussed previously, although their functional dependence can be different. Fig. 2.5 shows an overview of the energy components with their dependences and indicates that E_{bond}, E_{angle} and E_{torsion} are bond-order terms, while E_{vdW} and E_{Coulomb} are non-bonded terms.

The bond-order between a pair of atoms can be calculated from their separation distance. For example, in the case of carbons, the bond-order is given by:

$$\begin{aligned} BO_{ij} &= BO_{ij}^{\sigma} + BO_{ij}^{\pi} + BO_{ij}^{\pi\pi} = \exp\left[p_{\mathrm{bo},1} \cdot \left(\frac{r_{ij}}{r_0^{\sigma}}\right)^{p_{\mathrm{bo},2}}\right] + \\ &+ \exp\left[p_{\mathrm{bo},3} \cdot \left(\frac{r_{ij}}{r_0^{\pi}}\right)^{p_{\mathrm{bo},4}}\right] + \exp\left[p_{\mathrm{bo},5} \cdot \left(\frac{r_{ij}}{r_0^{\pi\pi}}\right)^{p_{\mathrm{bo},6}}\right], \qquad (2.42) \end{aligned}$$

where the first, second and third term correspond to the single (σ), double (π) and triple (double π) bond order contributions, respectively. The bonding terms (p) and bonding equilibrium distances (r_0) are parameterised according to quantum mechanical predictions for species separated by a distance r_{ij}.

The non-bonded contributions are calculated independently, as indicated in Fig. 2.5. The van der Waals interactions are modelled by a distance-corrected Morse potential, where a shielded interaction helps to avoid excessively high repulsions at short distances. The most computationally demanding part of the ReaxFF calculations is the charge update at every timestep. A polarisable charge calculation method is essential for reactive force fields and is included in ReaxFF, which employs the Electronegativity Equalization Method (EEM) [80] and charge equilibration (QEq) method [81], which are based on the effective electronegativity and chemical hardness parameters. The electrostatic energy is minimized with the calculated equilibrium charge distribution. The implementation of ReaxFF is discussed in more details in Ref. [82].

The ReaxFF force field is implemented in this thesis in Chapter 6 to describe the interactions of water molecules in a graphene nanochannel in the presence of ions, where it is essential to consider proton transfer mechanisms (bond formation and breaking).

2.7 LAMMPS

The results reported in this thesis are obtained from molecular dynamics simulations implemented by using the LAMMPS package [83]. LAMMPS is an acronym for Large-Scale Atomic/Molecular Massively Parallel Simulator.

It is an open source molecular dynamics code written in C++ and suitable for particles in liquid, solid or gaseous state. With a wide range of force fields and boundary conditions, and the possibility to include new capabilities, LAMMPS can model atomic, polymeric, biological, metallic, granular and coarse-grained systems of up to billions of particles. For rectangular systems with an uniform particle density, LAMMPS has proven to be the post efficient in a parallel computing sense. The code integrates Newton's equations of motion for atoms, molecules or macroscopic particles, with short or long-range interactions and several initial and boundary conditions. Some details are briefly discussed below.

2.7.1 Neighbor lists and periodic boundary conditions

The computational efficiency is improved by the use of neighbor lists to track nearby particles. Spatial-decomposition techniques are used to partition the simulation domain and smaller sub-domains are assigned to different processors. This approach is suitable for slowly changing environments during a typical simulation, where it is not necessary to update the neighbors lists every time-step. The nearby particles, i.e., the ones closer to the boundaries of the sub-domains, are tracked by “ghost" atom information stored and communicated between the processors.

The ghost atom information allows LAMMPS to model infinitely large systems. In order to avoid boundary effects on the particles in a system, periodic boundary conditions can be implemented. In LAMMPS, this is done by sharing translated ghost atoms between processors responsible for opposite boundaries of the simulation domain, i.e. particles at the boundaries are added as ghost atoms outside the original simulation domain when the neighbor lists are built and when integrating the equations of motion.

2.7.2 Long-range interactions

LAMMPS deals with long-range Coulombic interactions in periodic boundary conditions by means of a long-range solver. This approach is needed, e.g., for the implementation of the long-range TIP4P water model.

The method chosen in this thesis is based in the Ewald summation, which rewrites the interaction potential as the sum of two rapidly converging series:

$$\phi(\vec{r}) = \phi_s(\vec{r}) + \phi_l(\vec{r}), \tag{2.43}$$

where ϕ_s is a short-range term in the real space and ϕ_l is a long-range term in the reciprocal (Fourier) space. This is achieved by using shielding charge distributions about the atomic charges themselves, in a way that the electrostatic interactions decay rapidly and can be evaluated by applying an spherical cutoff (typically $\sim 10\,\text{Å}$), corresponding to the short-range interactions [84]. In order to cancel the shielding distributions, a second charge distribution is included, with equal magnitude and opposite sign, corresponding a long-range smooth function whose Fourier transform decays rapidly. Due to the Fourier sum, the method considers that the system is infinitely periodic. Therefore, the long-range term considers the charges of the unit cell and all its images (ghost atoms).

The standard Ewald method considers a spherical Gaussian shielding distribution [85]:

$$\gamma_l(\vec{r}) = \frac{\alpha^3}{\pi^{3/2}} \exp(-\alpha^2 r^2), \tag{2.44}$$

where α is the truncation parameter. The short-range electrostatic potential due to a point charge minus and including the normalized Gaussian shielding distribution is:

$$\phi_s(r) = \frac{1}{4\pi\epsilon_0}\left(\frac{1}{r} - \frac{\operatorname{erf}(\alpha r)}{r}\right) \tag{2.45}$$

and the long-range contribution is given by:

$$\phi_l(\vec{r}) = \frac{1}{\epsilon_0 V} \sum_{\vec{k}} \frac{\exp(-k^2/(4\alpha^2))}{k^2} \sum_i q_i \exp(i\vec{k}\cdot(\vec{r}-\vec{r}_i)). \tag{2.46}$$

The long-range potential is obtained by performing the analytical Fourier transform of Poisson's equation, solving the equation for the Fourier transformed potential and then applying the inverse Fourier transform.

Solving analytically the Fourier transforms results in high computational cost. In order to circumvent this drawback of the Ewald summation method, the particle-particle particle-mesh (PPPM) method was developed by Hockney and Eastwood [85, 86], where the short-range (long-range) term is calculated from particle-particle (particle-mesh) interactions. The shielding charge distribution in the PPPM method is a S2 function, i.e., a sphere with decreasing density:

$$\gamma(\vec{r}) = \begin{cases} \frac{48}{\pi a^4}\left(\frac{a}{2} - r\right), & r < a/2 \\ 0, \quad r > a/2 \end{cases} \tag{2.47}$$

where the short range interaction between two particles with S2 charge distributions $\gamma(\vec{r})$ can be expressed as:

$$\phi_s(\xi_{ij}) = \frac{1}{4\pi\epsilon_0}\left(\frac{1}{r_{ij}} - \frac{1}{70a}\sum_{n=-1}^{7} C_n \xi_{ij}^n\right) \quad \xi_{ij} < 2, \tag{2.48}$$

where

$$C = \begin{cases} (0, 208, 0, -112, 0, 56, -14, -8, 3), & 0 < \xi_{ij} < 1 \\ (12, 128, 224, -448, 280, -56, -14, 8, -1), & 1 < \xi_{ij} < 2. \end{cases} \tag{2.49}$$

The long-range contribution is given by

$$\phi_l(\vec{k}) = \frac{\hat{\gamma}(\vec{k})^2}{\epsilon_0 k^2}\hat{\rho}(\vec{k}) = \hat{G}(\vec{k})\hat{\rho}(\vec{k}), \tag{2.50}$$

where other forms for the optimal influence function, $\hat{G}(\vec{k})$, can be taken for a given system size, charge shape and interpolation function.

In order to solve the long-range function, The PPPM method maps the atom charge to a 3D mesh by using weighting functions to compensate for the actual position of the charges. The Poisson's equation on the mesh is solved by very efficient numerical 3D Fast Fourier Transforms (FFTs) to obtain $\hat{\rho}(\vec{k})$ and, by multiplying with $\hat{G}(\vec{k})$, $\hat{\phi}_l(\vec{k})$ is obtained. By applying again the FFT, at this time to $\hat{\phi}_l(\vec{k})$, $\phi_l(\vec{r})$ is obtained at the mesh points. The electrostatic fields on the mesh are then obtained by numerically differencing the potentials and the fields on the original atoms position are calculated by interpolating the values of the mesh points. The computational cost of the traditional Ewald summation method for a system of N particles scales as $\mathcal{O}(N^{3/2})$, while the PPPM solver scales as $\mathcal{O}(N\log(N))$ due to the FFTs [87].

2.7.3 Bond and angle constraints

In order to consider a group of particles as a rigid body, constraint algorithms are needed to ensure that the distance between the particles are maintained. Rigid water models, as the TIP4P model, demand bond and angle constraints for the water molecule to be treated as a rigid body. This is essential when using the TIP4P model in a system under an applied electric field. This is achieved by resetting the specified bonds and angles to their equilibrium lengths and angular values each time-step. An additional constraint force is applied so that the desired particle separations are preserved at their new positions.

2.7.4 Electric field

An electric field is applied in the system or in a group of particles in the system by adding an electric force:

$$F_i = q_i E \tag{2.51}$$

where q_i is the charge of the particle i and E is the chosen electric field. When subjected to the electric force, particles move or rotate according to the applied electric field and their potential energy changes. This is a crude approximation of the effects of an applied electric field, since here we consider that the local electric field is equal to the applied electric field and that the polarization is only constituted by the dipolar contribution. Nonetheless, this approach can give good insights regarding the actuation of systems by an electric field.

Part II

Decorated carbon nanotubes

CHAPTER 3

STRUCTURAL AND DYNAMICAL PROPERTIES OF METALLIC NANOPARTICLES ON CARBON NANOTUBES

Metallic nanoparticles are known to bind to different compounds and nanomaterials and to be able to enhance properties such as electrical conductivity and sensing capabilities of the host. Metallized hybrid materials are highly desirable in nanoelectronics, optics and biochemistry and have a wide range of applicabilities. With that as motivation, we investigate using molecular dynamics simulations the deposition, clustering and distribution of metallic nanoparticles on a carbon nanotube. We present here the properties of the nanoparticles that depend on the properties of the carbon nanotube and temperature.

3.1 Introduction

Experimental and theoretical studies of carbon nanotubes (CNTs) have been focused to date on the investigation and optimization of their properties, as well as the conjugation with different particles and biomolecules and the effects of external parameters such as applied electric fields [88–92]. The nanoscale diameter of a CNT and its length that can reach the macroscale range enable simultaneously quantum effects and the possibility to connect to macroscopic devices. The near one-dimensionality of CNTs confers unique electromechanical, optical and chemical properties, allowing for their wide potential applicability and making the use of CNTs highly desirable in the fabrication of high-strength fibers and quantum wires [93, 94].

The addition of suitable materials on the CNT surface can significantly enhance its sensing abilities [92]. Decorated carbon nanotubes can be conjugated with different nanoparticles (NPs), forming hybrid nanostructures of high interest to electronic, magnetic and catalytic purposes. In this regard, metallic NPs appear as great candidates, since they are known to bind to different compounds with high selectivity and specificity. Moreover, the electrical conductivity of CNTs could also be enhanced by the deposition of metallic atoms on its surface, which is highly desirable in the application of CNTs as nanowire templates [95–97]. The presence of structural defects on the CNT surface such as vacancies can also improve the catalytic activity and durability of CNT-NP based nanostructures, as a higher binding energy surface avoids the migration of NPs on the support surface [98, 99].

The investigation of hybrid nanostructures composed of metallic NPs and carbon nanotubes have been concentrated on the self-assembly of NPs on the CNT surface [100–103]. The CNT-NPs structures can be produced by different methods, i.e., electrochemical deposition, electroless deposition, dispersion of NPs on functionalized CNTs and physical methods [104]. Different methods of fabrication can lead to different adsorption schemes. The ability to control the assembly of NPs and their properties enables the optimization of such devices. For example, the control of size and distribution of NPs grown by electrochemical deposition was already achieved by varying potential, time and solution concentration [105, 106]. Besides temperature and other external factors that can be important for the application in fuel cells and sensing mechanisms, properties such as the CNT radius and chirality may also be important to determine the NPs characteristics. The migration and coalescence of NPs are expected and have been already indirectly observed experimentally for the case of Ag NPs on CNTs through changes in the NPs sizes and position when increasing the temperature [52]. However, another study with varying temperature was only able to observe significant changes on gold NP size and shape under specific circumstances, although the NP properties were found to be affected by the film thickness [107]. The effects of external and internal factors on the response characteristics of CNT-NPs nanodevices are still open questions. In this sense, a theoretical investigation of the NP dynamics and their preferred assembly mechanisms can highly contribute to this matter.

Here we theoretically investigate the deposition, clustering and distribution mechanisms of Ag NPs on CNTs. Different adsorption schemes are found according to the CNT properties. By performing molecular dynamics simulations, we show that properties of the NPs such as size, migration mechanisms and diffusion are closely related to the CNT properties such as chirality and presence of defects. We also report the influence of the temperature on the NPs properties. Our aim is to shed light on aspects of CNT/NP hybrid devices that are troublesome to infer only by experimental results.

3.2 Simulation details

We employed atomistic molecular dynamics (MD) simulations, as implemented in the LAMMPS package [83]. The Adaptive Intermolecular Reactive Empirical Bond Order (AIREBO) force field [77] and the Embedded Atom Method potential (EAM) [75] are used to model the C-C and Ag-Ag interaction, respectively. The Ag-C interaction was modelled by the Lennard-Jones (LJ) potential, with $\epsilon_{\text{C-Ag}} = 0.0301\,\text{eV}$ and $\sigma_{\text{C-Ag}} = 3.006\,\text{Å}$ [108].

Initially, we considered pristine CNTs of different chiralities with height $h = 100\,\text{nm}$ and 1500 Ag atoms randomly distributed around the tube axis at a distance of $3-5\text{Å}$ from the CNT surface. Periodic boundary conditions were applied along the z direction (parallel to the CNT axis). The system was equilibrated at a temperature of $T = 300\,\text{K}$ for 30 ns using the NVT ensemble with a Nosé-Hoover thermostat and a timestep of 1 fs. Defective CNTs were also considered, where randomly selected carbon atoms were removed from the CNT surface. We considered different defect concentration.

3.3 Types of formed nanoparticles after metallic adsorption on a CNT

Our MD simulations on adsorption of Ag atoms on the CNT surface led to formation of Ag NPs. The size and shape of NPs were determined by their migration and coalescence mechanisms. Different shapes of NPs were then obtained, e.g. elongated, dot- or ring-shaped NPs (depicted in Fig. 3.1). Dot-shaped [Fig. 3.1(a)] nanoparticles were formed by a smaller number of Ag atoms. Ring-shaped [Fig. 3.1(b)] or elongated [Fig. 3.1(c)] NPs were usually formed by initially smaller dot-shaped NPs, which migrated and coalesced to form larger NPs. For a sufficient available density of Ag atoms, the ring-shaped NPs completely enveloped the CNT, which was favoured by the high curvature of CNTs with small radius. On the other hand, the high aspect ratio of NPs favoured the formation of elongated NPs aligned to the tube axis. Experimental studies have commonly reported dot-shaped metallic nanoparticles [95–97]. The diameter of carbon nanotubes and the size of nanoparticles on experiments, however, are usually larger than those considered here. Therefore, the different NP shapes found here might indicate that other shapes can be favoured by a larger surface curvature.

3.4 Nanoparticle migration and coalescence mechanisms

The interaction between NPs and CNTs is considered to be of van der Waals type. Such weak interaction, together with the interplay of the interparticle interaction between NPs and the effects of temperature, leads to the migration of NPs over the CNT surface. The NP migration leads to a reorganization of the distribution of NPs on the nanotube and can also lead to coalescence of NPs. Fig. 3.2 shows the evolution in time (t) of the metallization of a (6,6) CNT at $T = 300\,\mathrm{K}$. For $t \leq 3\,\mathrm{ps}$, the nanotube is coated by small NPs. The small NPs migrate and coalesce, which is easily seen in the shown snapshot at $t = 42\,\mathrm{ps}$. The NPs rearrange following the tube morphology, i.e., forming helical patterns, with the helical pitch increasing with the size of NPs. This

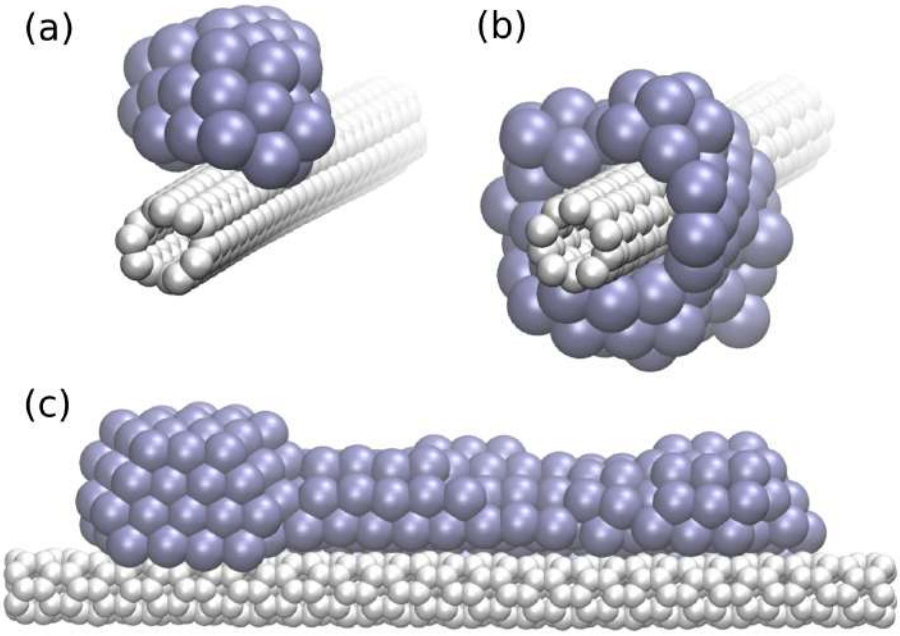

Figure 3.1: Typical nanoparticle shapes. (a) Dot-shaped NP. (b) Ring-shaped NP. (c) Elongated NP.

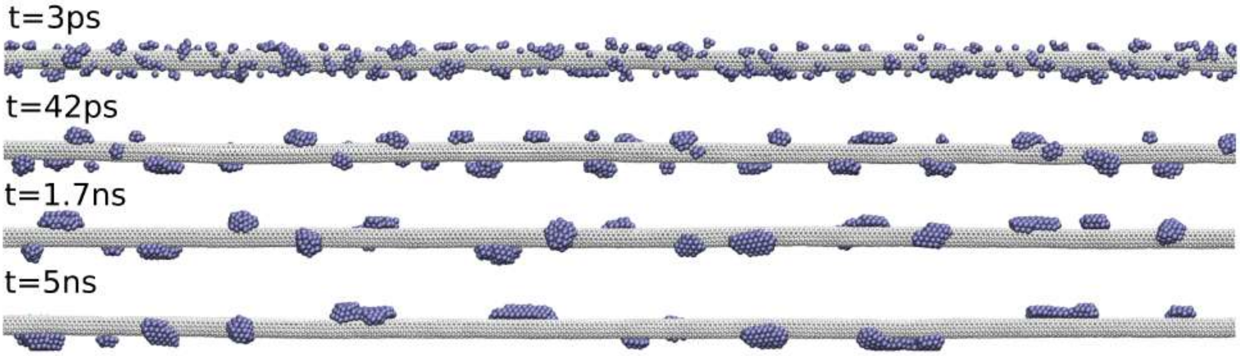

Figure 3.2: Time evolution of the formation of Ag NPs on the surface of a (6,6) CNT at $T = 300\,\mathrm{K}$ (60% of the simulated length is shown).

is shown in Fig. 3.2, through snapshots for $42\,\mathrm{ps} \leq t \leq 5\,\mathrm{ns}$. Smaller NPs are typically dot-shaped while larger NPs exhibit an elongated form aligned to the tube axis.

The CNT properties determine not only the displacement of the ions but also their mobility. Fig. 3.3 shows that CNT chirality is detected by the NPs and determines the resulting motion trajectories of the NPs. Distinct trajectories are shown for NPs adsorbed on a chiral (8,4) and an armchair (6,6) CNT with nearly the same diameter ($d \sim 8.3\,\text{Å}$). For the (8,4) CNT [panel (a)], two Ag NPs are initially separated (red), and move towards each other following helical trajectories in different directions and with different helical pitches until coalescence (blue). During the process, other NPs rearrange their position [depicted in the edges of the tube portion shown in panel (a)]. Although the helical pitch may vary, the NP motion on the surface of chiral CNTs is limited to helical trajectories. However, NPs adsorbed on zigzag and armchair CNTs also exhibit axial motion, as shown in panel (b) for the (6,6) CNT. The displacement of a smaller NP, initially shown in the left-hand side of the tube (red) exhibits a two-step behavior: first, it follows an axial path and later a helical trajectory until it merges with a larger NP (blue). Meanwhile, a third NP, shown on the right-hand side, follows a helical path. The different migration trajectories of nanoparticles for different CNT chiralities indicates that some CNT properties can be detected by analysing the adsorbed metallic nanoparticles. We note that our results are in line with previous reports on different helical pitches for thermophoretic mass transport through CNTs of different chiralities [109].

3.5 Nanoparticle diffusion

The effects of the CNT properties on the migration trajectories of NPs lead to different diffusion coefficients of nanoparticles on distinct CNT chiralities. This result is shown in Fig. 3.4, where the mean square displacement (MSD) $\langle r^2(t) \rangle$ of NPs on a (10,0) CNT (zigzag) is the largest, while on the (6,6) CNT (armchair) is the smallest. The (8,4) CNT (chiral) exhibits a small increase in the MSD of NPs as compared to the armchair CNT. The three considered CNTs have nearly the same diameter, i.e., $d \approx 8\,\text{Å}$, so the observed differences cannot be attributed to the CNT size. The vectors $\mathbf{a}_1$ and $\mathbf{a}_2$ in the bottom panels of Fig. 3.4 represent the vectors of the hexagonal unit cell of the nanotubes. The MSD curves in Fig. 3.4 and the migration trajectories in Fig. 3.3 indicate that the most favoured directions for NP migration are those parallel to $\mathbf{a}_1$ and $\mathbf{a}_2$ in the zigzag direction. The considerably larger MSD for the (10,0) CNT specifies that the $\mathbf{a}_2$ direction for zigzag CNTs is preferable to the $\mathbf{a}_1$ direction. The significant decrease in the MSD for armchair CNTs as

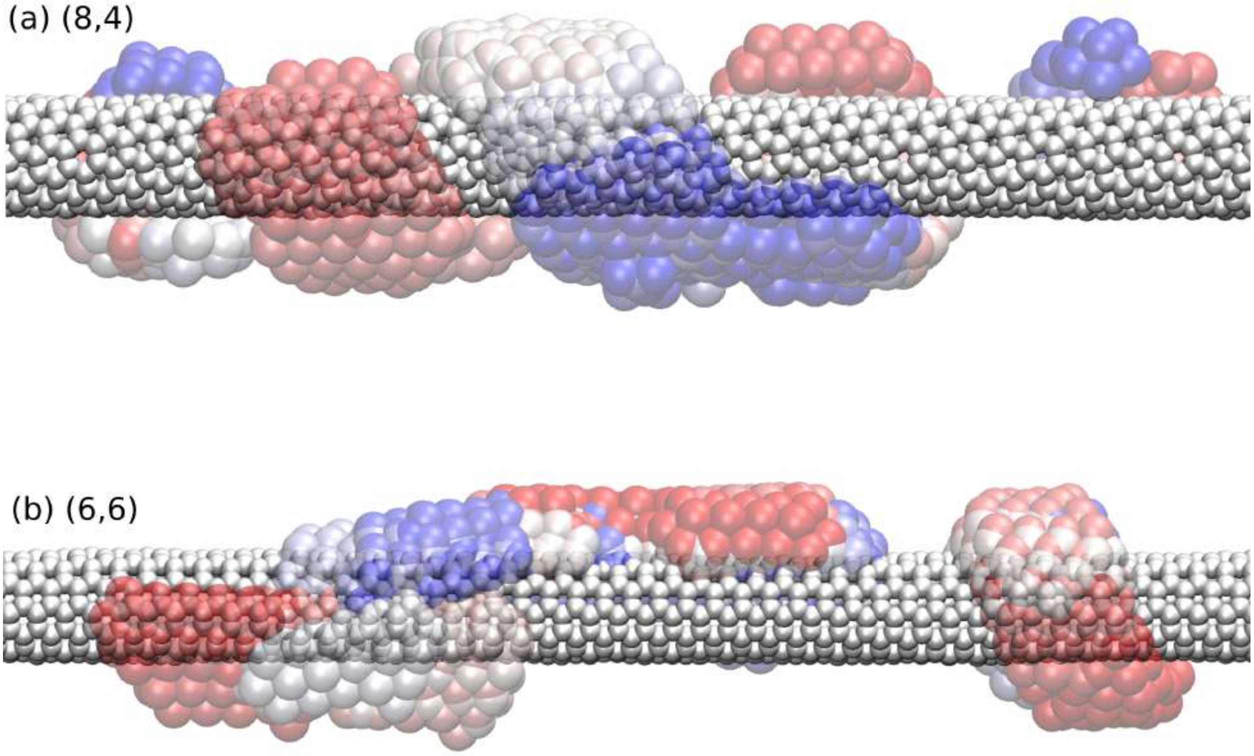

Figure 3.3: The detailed trajectories of Ag NPs on the (a) (8,4) CNT for a time interval of $t = 0.4$ ns, and (b) (6,6) CNT for a time interval of $t = 0.3$ ns, both at $T = 300$ K. The beginning stages of the trajectories are depicted in red, while the middle are in white and the final positions are shown in blue.

compared to zigzag CNTs indicates that the axial motion shown in Fig. 3.3(b) does not have a significant influence on the NP displacement for longer times. From the distinct MSD for different chiralities, one can conclude that a zigzag CNT would be better employed for mass transport purposes, while an armchair CNT would be the best choice for a static support.

3.6 Size of nanoparticles

The likelihood of distinct migration patterns of NPs according to the CNT chirality affects not only the NP diffusion but also the size of NPs. Fig. 3.5 shows the probability distribution of the radius of gyration of NPs for different CNT chiralities. The faster diffusion of NPs on zigzag CNTs is reflected on a higher probability to find larger NPs on such CNTs, although with a wider size distribution. In the bottom panels of Fig. 3.5, 30% of the simulated CNT

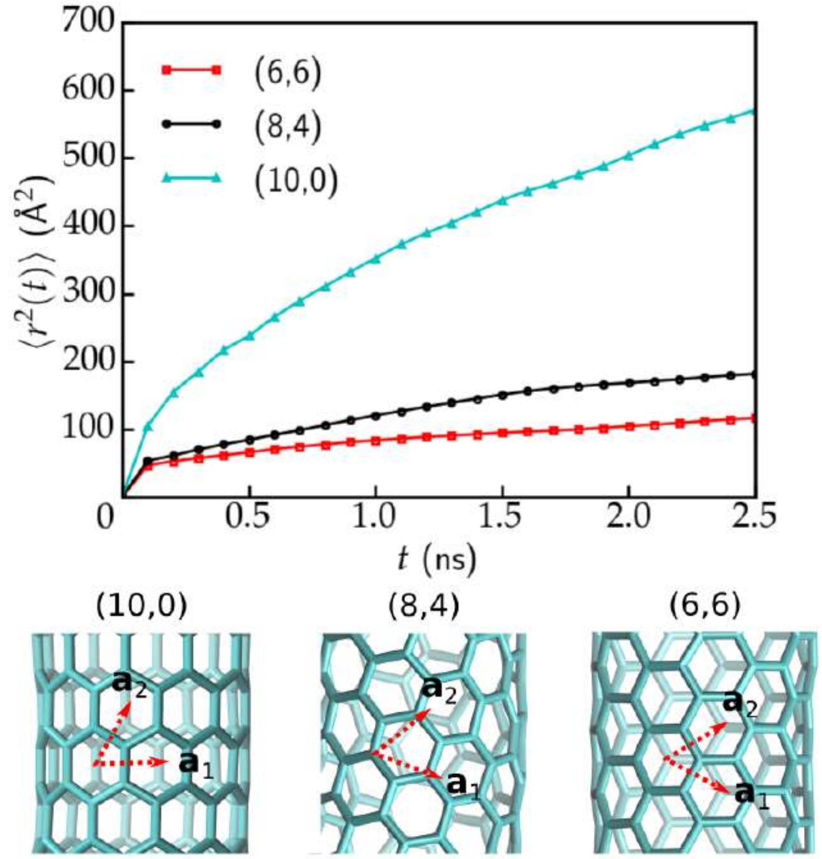

Figure 3.4: Mean square displacement of Ag nanoparticles adsorbed on CNTs of different chiralities.

length is visible, where NPs with different characteristics are shown for the distinct chiralities of CNTs. In the case of the (10,0) CNT, elongated NPs aligned to the tube axis are found together with a smaller dot-shaped NP. For the (8,4) CNT, the assymmetry of the chiral angle with respect to the tube axis favours helical NPs, which depending on the number of available atoms may close to form ring-shaped NPs. Dot-shaped NPs are more likely to be found on the (6,6) CNT than for the other chiralities.

3.7 Temperature effects

The NP properties of NPs formed by adsorption on a CNT can also be affected by temperature, since thermal vibrations favour the NP migration and consequent coalescence. Fig. 3.6 shows that the average size of NPs in-

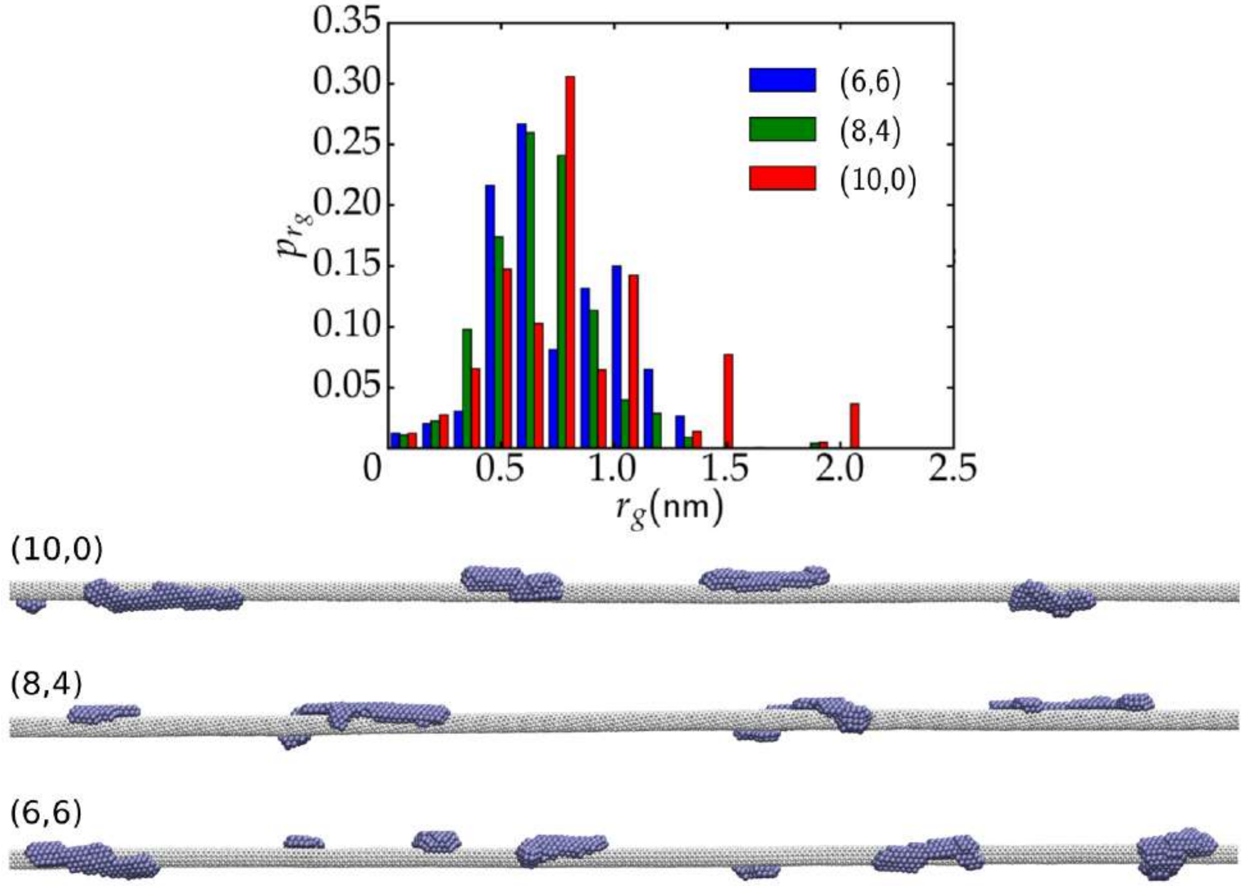

Figure 3.5: Probability distribution of the radius of gyration of NPs adsorbed on CNTs of different chiralities (top panel), and corresponding snapshots of NPs on CNTs after $t = 30\,\mathrm{ns}$ (bottom panel, 30% of the simulated length is shown).

creases with increasing temperature and different adsorption schemes are observed depending on the temperature of the system. At low temperatures, e.g., $T = 5\,\mathrm{K}$, thermal vibrations are not sufficient to overcome the binding between metallic atoms and the CNT surface and there is less NP migration. For that reason, the final configurations can be reached at shorter times, even for $t \sim 0.5\,\mathrm{ns}$. No axial motion is found at this temperature. Rings and elongated NPs with a tendency to have a helical displacement are found. However, very small NPs are also observed. At $T = 150\,\mathrm{K}$, dot-shaped NPs are distributed along the tube, although some elongated NPs can also be seen. At this temperature, the helical displacement of NPs is favoured. However, at higher temperatures, the helical pattern is lost due to the formation of

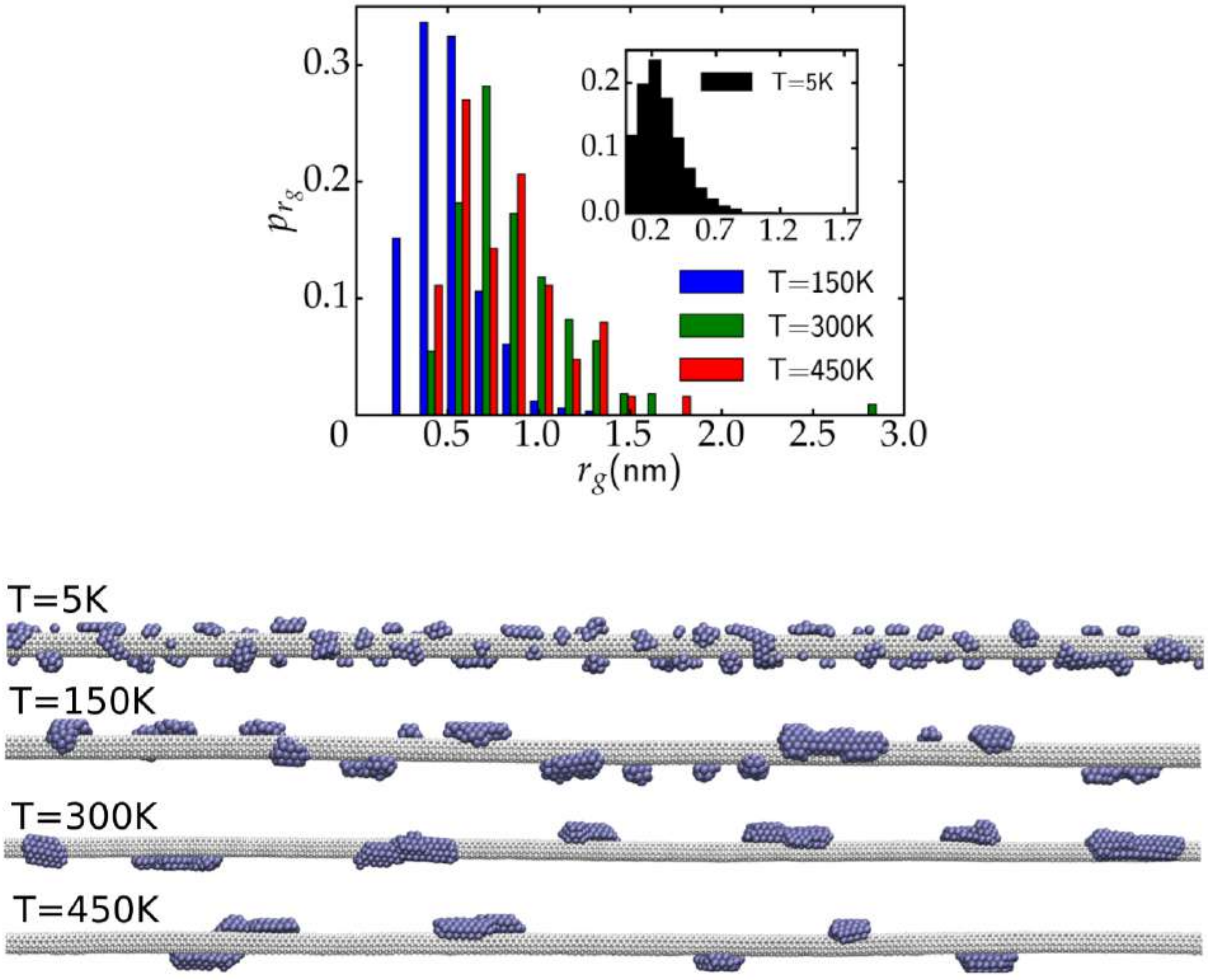

Figure 3.6: The probability distribution of the radius of gyration of Ag NPs on the (3,3) CNT (top panel), and the snapshots of the NP configuration after $t = 5$ ns at different temperatures indicated in the figure (30% of the simulated length is shown).

larger NPs, as shown for $T = 300$ K and $T = 450$ K. As seen in Fig. 3.6(b), the average size of NPs increases with increasing temperature.

3.8 Defective carbon nanotubes

Although the experimental techniques for the synthesis of CNTs have been constantly improving [1], the fabrication of pristine carbon nanotubes is still challenging and the presence of structural defects on the fabricated CNTs is common. Structural defects such as vacancies on the CNT surface are

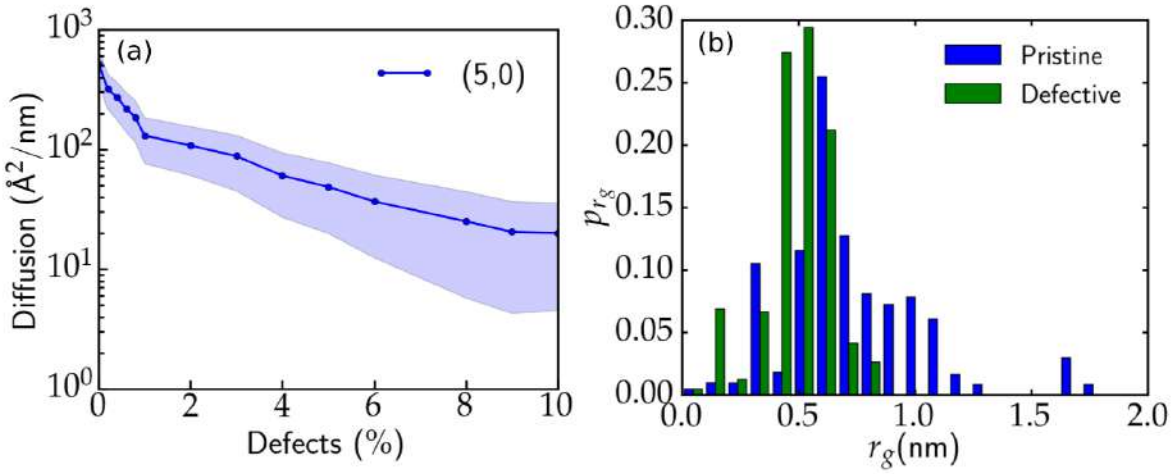

Figure 3.7: (a) Diffusion of NPs on a (5,0) CNT as a function of the defect concentration (filled region corresponds to standard deviation). (b) The probability distribution of the radius of gyration of NPs adsorbed on pristine and defective (5,0) CNTs.

expected to exhibit a pinning behavior, i.e., nanoparticles are easily trapped in those defective sites. Functionalization of carbon nanotubes can also favour the anchoring of nanoparticles [104]. In the case of defective or functionalized CNTs, NPs may present different structural and dynamical properties as compared to pristine CNT. For example, when considering vacancies on the CNT surface, we found that the NP diffusion significantly drops even for zigzag CNTs, which presented the larger MSD in the case of a pristine CNT. This effect is shown in Fig. 3.7(a), where the NP diffusion is shown for the (5,0) CNT. A drop of more than one order of magnitude is observed for the NP diffusion when 5% of the carbon atoms are randomly removed from the CNT structure.

The presence of defects on the CNT surface also affects the size of the adsorbed NPs, since the pinning effect of the vacancies impedes NP migration and consequently the coalescence as well. As a result, the probability distribution of the radius of gyration in Fig. 3.7(b) shows a narrower distribution for the defective CNT, compared to a pristine one, and smaller mean size of NPs.

3.9 Conclusions

Different adsorption scenarios of metallic atoms are observed depending on the carbon nanotube properties and temperature. The formation of nanoparticles occurs through migration and coalescence mechanisms. The nanoparticle migration follows preferred trajectories and directions on the tube surface, depending on the chirality of the carbon nanotube. The size and displacement of nanoparticles is affected not only by the tube chirality, but also by the presence of structural defects on the nanotube. For pristine carbon nanotubes, zigzag nanotubes presented higher nanoparticle mobility, yielding larger nanoparticles, while armchair nanotubes exhibited the lowest nanoparticle mobility. By varying the temperature of the system, the nanoparticle migration could be controlled, achieving smaller (larger) nanoparticles for lower (higher) temperatures. The coating of carbon nanotubes with metallic nanoparticles can be optimized by structural defects on the tube surface such as vacancies, leading to smaller and more uniformly sized nanoparticles with reduced mobility. Our results on the link between the NPs and CNT properties is important not only for the optimization of hybrid nanodevices, but also as a mechanism to indirectly determine certain CNT properties by observing characteristics of the adsorbed NPs.

CHAPTER 4

UNCONVENTIONAL TWO-DIMENSIONAL VIBRATIONS OF A DECORATED CARBON NANOTUBE UNDER ELECTRIC FIELD: LINKING ACTUATION TO ADVANCED SENSING ABILITY

In this chapter we show that a carbon nanotube decorated with different types of charged metallic nanoparticles exhibits unusual two-dimensional vibrations when actuated by applied electric field. Such vibrations and diverse possible trajectories are not only fundamentally important but also have minimum two characteristic frequencies that can be directly linked back to the properties of the constituents in the considered nanoresonator. Namely, those frequencies and the maximal deflection during vibrations are very distinctively dependent on the geometry of the nanotube, the shape, element, mass and charge of the nanoparticle, and are vastly tunable by the applied electric field, revealing the unique sensing ability of devices made of molecular filaments and metallic nanoparticles.

4.1 Introduction

Nanoelectromechanical systems (NEMS) exhibit profound effects stemming from the coupling of the mechanical properties of the devices to their electronic degrees of freedom [88, 110–113]. NEMS have been intensively studied and have an incredible potential for technological applications, e.g., the detection of external electromagnetic fields, control and enhancement of the high quality factor of the resonators and tunable high natural mechanical frequencies [88, 114, 115]. The latter makes nanoresonators candidates for advanced mass and force detectors, since small quantities of adsorbed mass can be detected by distinct shifts in the frequency of vibrations [17, 18, 24, 26, 116–119]. In that sense, doubly-clamped carbon nanotubes (CNTs), as well as cantilevers, have attracted noticeable attention since they offer unique resonance properties that are proven useful to detect atoms and single molecules [89, 120, 121], which can be applied, among other possibilities, in mass spectrometry and air pollution control [122–124]. Furthermore, such precise mass sensing enables other biotechnological applications, e.g., DNA sequencing and detection of biomarkers at early stages of cancer and other diseases [125, 126]. The electromechanical properties of CNTs typically allow to reach frequencies in the GHz range. Higher frequencies, i.e., up to the order of THz, are expected when suitable coating materials are used [23, 27, 127–129]. Moreover, CNTs are now able to present high quality factors, which combined with high resonance frequencies are essential for applications in mass sensing [129–131].

On the other hand, metallic nanoparticles (NPs) have found numerous applications in engineering, materials science, physics, chemistry, biology and medicine [132–136]. They have an incredible potential for application in diagnostic imaging and drug delivery systems. Metallic NPs can attach to different organic compounds and antibodies with high selectivity and specificity, which can be improved by a ligand conjugation. The development of materials with antibacterial properties based on metallic NPs and studies of interaction of metallic NPs with HIV-1 have been already reported [137, 138]. This versatility of NPs, and their relatively easy functionalization open a possibility to synthesize CNTs decorated by metallic NPs, and thereby broaden and advance NEMS applications [97, 139, 140].

Traditionally the resonance frequency of CNTs is obtained from the one-dimensional (1D) oscillator model, characterized by a single frequency, where several definitions have been used for the effective spring constant κ [18, 88, 111–115], each of which adequate for a specific setup. Such 1D description is not always sufficient, since it is known that applied electric field as well as molecular adsorption may induce nonlinear effects that entirely change the nanoelectromechanical resonant properties [141, 142], calling for further advanced theoretical models.

Here we thoroughly analyse the vibrational properties and the induced deflections of a doubly clamped CNT decorated with a charged metallic NP and subjected to an external electric field. We reveal that such a system exhibits nontrivial and diverse 2D vibrational motions depending on the strength of the electric field, and we propose a suitable theoretical model incorporating two frequencies of vibrations, i.e. the conventional frequency and the modulation frequency. Significant shifts in those frequencies were found for CNTs with different chiralities and for NPs made of different elements, which can be further employed for engineering nanoparticle diagnosis for biomedical applications based on nanomechanical sensors.

4.2 Model and methods

Our mechanical nanosensor, shown in Fig. 4.1a, comprises a charged metallic NP located around/at the outer midpoint of the doubly clamped carbon nanotube, and is subjected to an external constant electric field perpendicular to the nanotube. We investigate three types of CNTs of $\approx 0.4\,\text{nm}$ diameter, i.e. (3,3) (armchair), (4,2) (chiral) and (5,0) (zigzag) CNTs. CNTs of small diameter constitute essentially ideal 1d systems and the existence of 0.4-nm CNTs has been theoretically predicted and experimentally confirmed [143, 144]. In most of the here considered cases the length of the CNT was L =50 nm, while the number of atoms within the NP and the charge of the NP were taken as N =50 - 100 and q =1 - 10e, respectively. We considered three kinds of NPs, made of Na, Pd or Ag. To isolate the vibrations induced solely by the actuation due to the charged NP and external electric field, we neglected induced charges on the CNT [89]. In order to compare the deflections and vibrations of a decorated CNTs with those of a pristine CNT, we considered a charged (5,0) CNT with an uniform charge $q = 1\mathrm{e}$.

4.2.1 MD simulations

We employed atomistic MD simulations, with the Adaptive Intermolecular Reactive Empirical Bond Order (AIREBO) force field [77] and the Embedded Atom Method potential (EAM) [75] as implemented in the LAMMPS package [83] to respectively model the carbon-carbon bonds and metal-metal interaction (for silver and palladium). The metal-metal and the carbon-metal interactions for sodium were modeled by the Lennard-Jones (LJ) potential with parameters taken from Refs. [108], [71].

CNT-NP composites can be synthesized either by chemisorption or physisorption, leading to different interfaces between the CNT and the NP. For example, the intensity of the adsorption energy and the nature of the adsorption site indicate that while Ag NPs are physisorbed, Pd NPs are chemisorbed, with stable covalent bonds due to a large contribution from d-orbitals [145–148]. However, the binding between the CNT and Ag or Pd NPs is relatively weak as compared to the metal-metal interaction [148, 149] enabling one to use the simple LJ potential in the model for the C-Ag and C-Pd interactions [149, 150]. Note that our method comprises classical simulations which allows us to simulate large systems and their behavior over long time.

4.2.2 Euler-Bernoulli beam theory

Our theoretical description of carbon nanotubes as nanoelectromechanical systems is based on the linear theory of elasticity and more specifically on the Euler-Bernoulli beam theory, which enables the calculation of load-carrying, deflection and vibrational characteristics of beams [111, 112]. Considering a doubly clamped beam of length L bent due to a downward force (e.g., electrostatic force) and a coordinate system such that x is along the beam axis, the elastic energy of the beam is given by [151]:

$$U = \frac{1}{2}\int_0^L \left[YI\ddot{u}^2(x) + T\ddot{u}^2(x) + Kz \right] \mathrm{d}x, \tag{4.1}$$

where $u(x)$ is the tube deflection at the x position, Y is the Young's modulus, $I = \pi r^4/4$ is inertia moment and K is the force per unit length. The derivatives are with respect to x. The first term in Eq. (4.1) is the energy of an unstressed beam (flexural energy), while the second term is the elastic energy due to the built-up tension:

$$T = T_0 + \frac{YS}{2L}\int_0^L \dot{u}^2 dx, \tag{4.2}$$

where T_0 is the residual stress that may result from fabrication and the second term is the induced stress due to the acting force, with the cross section $S = \pi r^2$. Minimizing the energy leads to the equilibrium equation:

$$YI\ddddot{u} - T\ddot{u} - K = 0. \tag{4.3}$$

4.2.2.1 Beam deflection

Equation (4.3) should be solved with the appropriate boundary conditions. In the case of a doubly-clamped beam, the following conditions should be fulfilled:

$$u(0) = u(L) = \dot{u}(0) = \dot{u}(L) = 0. \tag{4.4}$$

The solution for Eq. 4.3 with the conditions in Eq. 4.4 is given by:

$$u(x) = \frac{FL}{2T\xi}\left[\frac{\sinh\xi L}{\cosh\xi L - 1}(\cosh\xi x - 1) - \sinh\xi x + \xi x - \frac{\xi x^2}{L}\right], \quad \xi = \sqrt{\frac{T}{YI}}. \tag{4.5}$$

Different regimes are possible depending on the magnitude of the applied force, with $T \ll YI/L^2$ ($T \gg YI/L^2$) yielding the bending (elastic) regime.

4.2.2.2 Resonant frequency

The dynamics of a beam can be captured by considering that

$$K = \mu\frac{\mathrm{d}^2u}{\mathrm{d}t^2}, \tag{4.6}$$

where μ is the linear mass density of the beam. Considering a solution of the form:

$$u(x,t) = \mathrm{Re}\left[u_0(x)e^{-i\omega t}\right], \tag{4.7}$$

the bending and elastic regime in Eq. 4.3 can be considered seperately, yielding:

$$\omega = \begin{cases} \left(\frac{\beta_n}{L}\right)^2 \sqrt{\frac{YI}{\mu}}, & \text{if } T \ll YI/L^2 \\ \frac{\pi}{L}\sqrt{\frac{T}{\mu}}, & \text{if } T \gg YI/L^2, \end{cases} \tag{4.8}$$

where the constant β_n depends on the boundary conditions and μ. In the case that both regimes are combined, Eq. 4.3 has to be solved self-consistently, accounting for all the terms, which leads to second order corrections to the solutions in Eq. 4.8 [112].

4.2.2.3 Stress and strain

The beam equation also describes forces and moments and therefore can be used to describe stresses. The stress σ_x in an Euler-Bernoulli beam are related to the deflection by the strain ϵ_x. For a homogeneous isotropic linear elastic material, the stress is related to the strain by

$$\sigma_x = Y\epsilon_x, \tag{4.9}$$

where

$$\sigma_x = -zY\ddot{u} \tag{4.10}$$

is the stress, where z is the distance from the neutral axis to the point of interest.

4.3 Results and discussion

4.3.1 Field-induced deformations

Once a CNT decorated with a charged metallic NP is subjected to an external electric field ($E = E_x$) applied perpendicularly to its axis (the z axis), it is bent [see Fig. 4.1a] and actuated into vibrations by the force acting on the charged NP. Our system can be modelled as a massive beam (of length L, aligned to the z axis, and fixed at both ends) subjected to a central force ($F_e = qE$) and stretched by a tension T. The maximal deflection at the midpoint of the beam, where the NP is located, is then given by [112]:

$$u_0(z = L/2) = \frac{F_e L}{4YI\xi^2}\left[1 - \frac{\tanh(\xi L/2)}{\xi L/2}\right], \tag{4.11}$$

where Y is the Young's modulus, I is the area moment of inertia, and $\xi = \sqrt{T/YI}$. If the bending energy is dominant and there is residual tension, one can write $T = c_1 + c_2 E^2$ [112].

By performing atomistic molecular dynamics (MD) simulations, our detailed analysis of the NP formation on a CNT revealed two typical types: i) a ring-shaped NP which is wrapped around the nanotube (with N =100 atoms) [see Fig. 4.1b], and ii) a dot-shaped NP which is attached on one side of the outer surface of the nanotube (N =50) [see Fig. 4.1c]. The variations of u_0/L with E for CNTs with chiralities (3,3), (4,2) and (5,0), all of them with diameter $d \approx 0.4$ nm and length L =50 nm, decorated with a Na, Pd or Ag NP with charge q =1e are shown in Fig. 4.1d. Notice that the ring-shaped NPs remain attached to the CNT up to significantly higher electric field than the dot-shaped NPs. This is due to the larger number of atoms on the ring-shaped NP and the larger number of bonding sites between CNT and NP favored by the ring geometry. As the electric force actuating the CNT is proportional to the charge of the NP, NPs of different chemical elements but having equal charges induce nearly identical maximal deflections. However, for higher electric fields and consequently higher tension in the CNT, the different built-in tension on the CNT due to the different chemical elements of the NP can lead to slightly different deflections, as can be seen in Fig. 4.1d for the (3,3) CNT in the range of fields between 3 $\mathrm{Vnm^{-1}}$ and 8 $\mathrm{Vnm^{-1}}$. Although u_0 is not very sensitive to the chemical element of the NP, it depends significantly on the CNT chirality, due to the different bending stiffness of such CNTs. The observed behaviour can be modelled by the continuum beam theory and captured by Eq. (4.11) – using two fitting parameters $a = 4c_1/qL$ and $b = 4c_2/qL$ – as shown by solid and dashed lines in Fig. 4.1d. For example, the fitting parameters for the (5,0) CNT in Fig. 4.1d were found to be $a \sim 25\,\mathrm{Vnm^{-2}}$ and $b \sim 13\,\mathrm{V^{-1}}$.

For the (5,0) and (4,2) CNTs, u_0 is linearly increasing with increasing

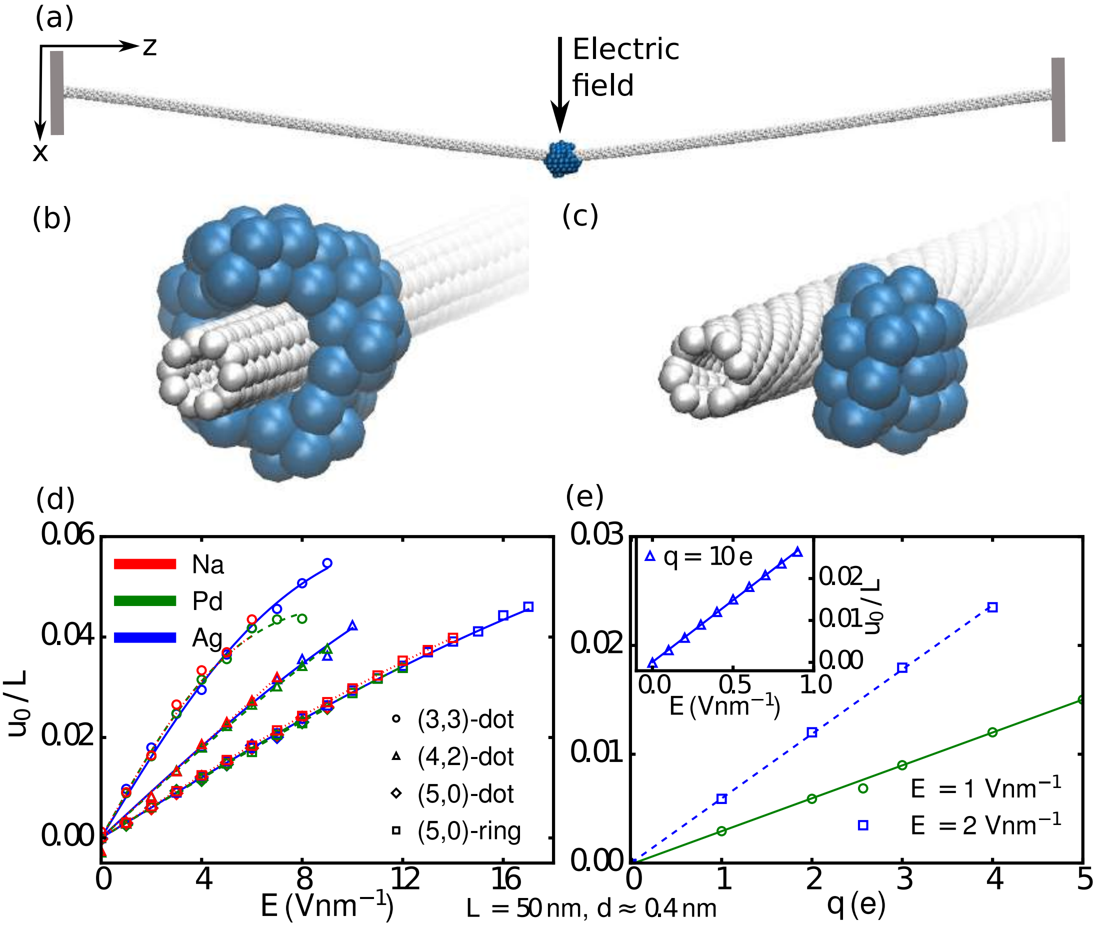

FIGURE 4.1. (a) The clamped CNT with a charged NP attached, bent under applied electric field. (b) A CNT decorated with a ring-shaped NP (100 atoms), and (c) with a dot-shaped NP (50 atoms) (zoomed in). (d) The variation of the maximal deflection of CNTs midpoint (u_0) relative to the CNT length (L) with electric field (E), and (e) the NP charge q. The inset in (e) shows variations of u_0/L with E for q =10e, while q = 1e in (d). The lines plotted in (d,e) are the best fits obtained using Eq. (4.11).

the electric field whereas for the (3,3) CNT (armchair) the linear response is observed only for the small deflections and small electric fields. Furthermore, u_0 can be tuned by varying the charge of the NPs, i.e. the larger the charge the larger the exerted force on the tube for the given field, hence larger the u_0. In Fig. 4.1e the variation of u_0/L with charge up to q =5e is depicted. The variations are shown for two (relatively large) values of electric field (E =1 Vnm^{-1} and E =2 Vnm^{-1}) applied on a (5,0) CNT decorated with a dot-shaped Ag NP. For this particular case, the system responds linearly to the external force, i.e. $u_0 \propto qE$. The lines in Fig. 4.1e are two linear fits that yield the spring constant of the tube.

We note that we do not consider field emissions on carbon nanotubes, since it is mostly favoured by electric fields applied parallel to the carbon nanotube axis, due to the charge concentration on the tip. Moreover, one can achieve similar and larger deflections of the CNT by using weaker electric field, by simply using a NP with larger charge. We verified this for a NP with q =10e on the (5,0) CNT and E <1 Vnm^{-1}, as plotted in the inset of Fig. 4.1e. This goes on to prove the high degree of tunability of our hybrid device and its performance.

CNTs with larger diameter have smaller deflections, which is attributed to their larger bending stiffness. Compared to the results for the (3,3) CNT, we found a decrease in u_0 of about 35% and 45% at E =9 Vnm^{-1} for (4,4) ($d = 0.54$ nm) and (5,5) ($d = 0.68$ nm) CNTs, respectively. The deformations of the CNTs also depend on the length of the tubes. For example, we found a linear increase of u_0 with increasing the length of the (5,0) CNT decorated with a dot-shaped Ag NP (N =50 atoms, q =1e) and two different applied electric fields, i.e. E =1 Vnm^{-1} and E =2 Vnm^{-1}. The latter are in agreement with the predictions of Eq. (4.11) [112]. Notice that such nanoscale deflections are measurable using atomic force microscopy [152].

4.3.2 Two dimensional vibrations

The presence of two spatially orthogonal vibration modes allows the CNT to vibrate along both directions even when subjected to a time-independent and constant electric field, which is due to a nonlinear interaction between the

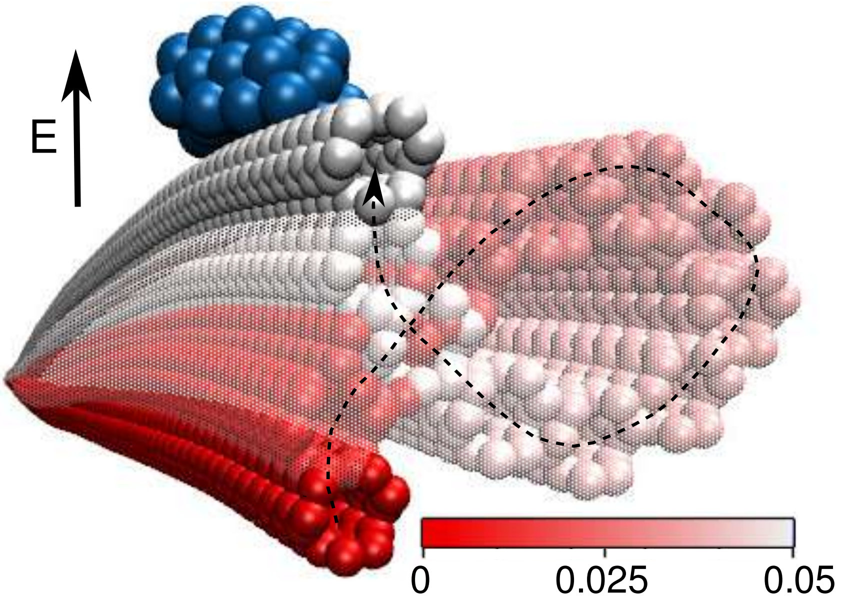

FIGURE 4.2. Cross-sectional view (55% of the CNT length) of the two-dimensional motion of the (3,3) CNT ($L = 50\,\text{nm}$) decorated with a dot-shaped Ag NP (N = 50, q = 1e), subjected to E =4 Vnm^{-1} (direction indicated by the arrow). The colour bar represents the simulation time in nanoseconds.

two vibration modes [141]. Moreover, this effect can be enhanced by the ever present asymmetry due to the attachment of a NP, which can also lead to changes in the orthogonal frequencies of vibration [142]. This is particularly relevant to our case, due to the not ideally symmetric positions of the metallic atoms within the NP (even the atoms of a ring-shaped NP do not form a perfect circular ring), as well as the asymmetry of the boundary conditions with respect to the chirality of the CNT on the clamped ends. Figure 4.2 depicts the two-dimensional motion of the (3,3) CNT decorated with a dot-shaped Ag NP subjected to E =4 Vnm^{-1}.

More generally by neglecting longitudinal vibrations, the deformation of the tube can be written as $\vec{u} = u_x\hat{i} + u_y\hat{j}$, where

$$u_i(\vec{r},E,t) = u_{0,i}(\vec{r},E) + w_i(\vec{r},E,\Omega_i,t)\cos(\omega_i,t), \tag{4.12}$$

with $\vec{r}$ being the position vector on the tube surface and $i = (x, y)$. Here w_i is a periodic function (with angular frequency Ω_i) indicating the envelope of the vibrational profiles in the i direction (see below), and $u_{0,i}$ is the maximal deflection of the tube in the i direction. The ω_i is the angular frequency of vibrations along the i axis. Notice that for any given electric field as well as CNT and NP properties, we always found $u_{0,y} = 0$ and $u_{0,x} = u_0$ in Eq. (4.12) [see Eq. (4.11)]. The non-uniform distribution of atoms in a ring-shaped NP causes the net force exerted on it (due to the electric field) to be different in, e.g., $\theta = 0$ and $\theta = 180°$ directions, where θ is the polar angle at the circular cross-section of the tube at $z = L/2$ [see Fig. 4.3a, where $F_R(\theta = 180°) < F_L(\theta = 0°)$]. The latter results in a net torque (τ) and eventually a complex entangled and combined linear and rotational motion in the x-y plane.

The aforementioned asymmetry in the microscopic structure of NPs may increase when large electric field is applied. In fact the atoms within the NP quickly rearrange once the electric field is switched on, e.g., noticeable changes on the structure of the ring-shaped Ag NP ($N = 100$, $q = 1$e) on the (5,0) CNT ($L = 50\,$nm) were observed for $E \geq 4\,\mathrm{Vnm}^{-1}$ within the initial 30 ps of the simulation. We found that the NPs preserve the new arrangement during the rest of the simulation, in all considered cases. Although such change in the microscopic structure of the NPs is usually neglected in similar considerations to ours [18], there were some experimental observations of the latter effect under specific circumstances reported by Conley *et al.* [141] and Gil-Santos *et al.* [142]. We show here that this effect is much more important than previously assumed.

In Fig. 4.3b, 4.3c and 4.3d we depict three typical trajectories of the observed 2D vibrations of the midpoint of the (5,0) CNT decorated with a ring-shaped Ag NP with $q = 1$e. Completely different trajectories were found for different applied electric fields. For $E = 3\,\mathrm{Vnm}^{-1}$ (b) and $E = 12\,\mathrm{Vnm}^{-1}$ (d) we obtained a non-circular (butterfly wings) pattern of trajectories, while an toroidal-shape trajectory pattern was found for $E = 5\,\mathrm{Vnm}^{-1}$ [see panel (c)].

The corresponding variations with time of $u_x(z = L/2, E, t)$ and $u_y(z = L/2, E, t)$ relative to L are shown in Fig. 4.3e, 4.3f and 4.3g, revealing different envelope frequencies of vibrations, i.e., $\Omega_{x,y}$, for different applied electric fields, e.g., $\Omega_x/2\pi = 0.36\,$GHz, $\Omega_x/2\pi = 0.94\,$GHz and $\Omega_x/2\pi = 4.22\,$GHz for $E = 3\,\mathrm{Vnm}^{-1}$, $E = 5\,\mathrm{Vnm}^{-1}$ and $E = 12\,\mathrm{Vnm}^{-1}$, respectively. The correlation

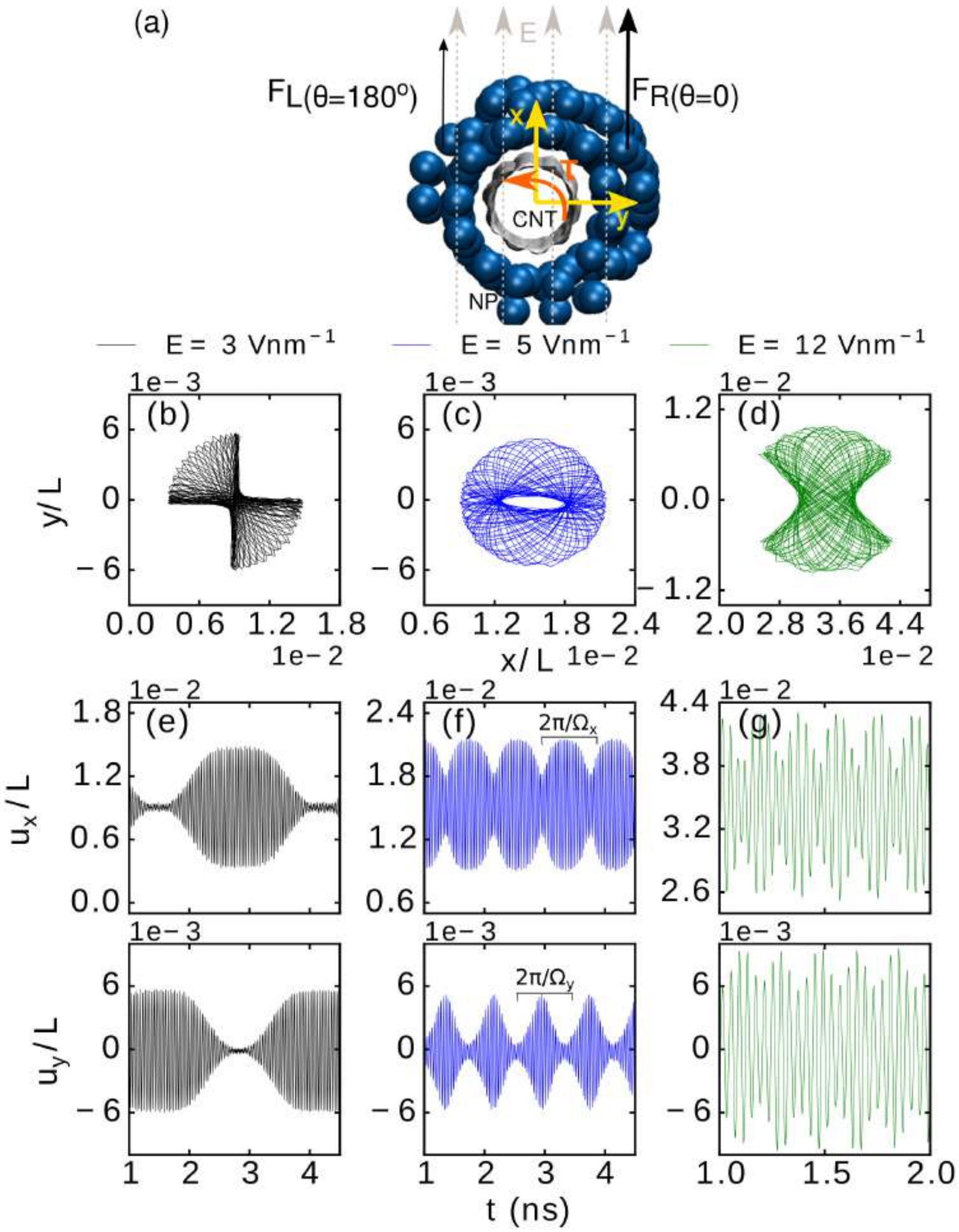

FIGURE 4.3. (a) Cross-sectional view of a decorated CNT, with indicated typical force components on the right and left side of the NP (F_R and F_L respectively), and the resulting torque τ. For for $t = 3$ ns, the path of vibrational motion in the (x, y) plane of the midpoint of a (5,0) CNT with $L = 50$ nm decorated with a ring-shaped Ag NP of 100 atoms and $q = 1$e, subjected to electric field E =3 Vnm^{-1} (b), 5 Vnm^{-1} (c), and 12 Vnm^{-1} (d). The corresponding relative deflections u_x/L and u_y/L as a function of time are shown in panels (e), (f), and (g), respectively. The envelope frequencies Ω_x and Ω_y are indicated in panel (f).

function $\langle u_x(t), u_y(t)\rangle = \delta$ can reveal the extent in which the observed 2D vibrations contain linear ($\delta \rightarrow 1$) or perpendicular polarization ($\delta \rightarrow 0$). In most of the cases, for weak electric fields [e.g. see Fig. 4.3b] the x and y motions were found to have predominantly linear polarization (being correlated/anti-correlated (i.e. $\delta > 0/\delta < 0$)), while for larger electric fields (e.g. Fig. 4.3c and 4.3d) the motions have predominantly perpendicular polarization, i.e. become nearly uncorrelated. The complete set of found trajectory patterns and the corresponding calculated δ are shown in Fig. 4.4.

The trajectories of the observed 2D vibrations of the midpoint of the (5,0) CNT decorated with a ring-shaped NP with q = 1e are shown in Fig. 4.5a, 4.5b and 4.5c for E =2 Vnm^{-1} and different constituent elements of the NP. For a Na NP (a) we obtained a circular fishnet trajectory pattern. For a Pd NP (b), a toroidal-shape trajectory pattern was found (similar to the pattern depicted in Fig. 4.3c for an Ag NP subjected to E =5 Vnm^{-1}). In the case of an Ag NP subjected to E =2 Vnm^{-1} a linear pattern of trajectories was observed (c).

The envelope frequency primarily depends on the properties of the NP and its bonding to the CNT. We point out that NPs of different elements could not be discerned in our deflection analysis in Fig. 4.1d, but do lead to different 2D pattern of vibrations of the CNT in the last analysis. Therefore, different envelope frequencies are observed for different constituent elements of the NP, as shown in Fig. 4.5d, 4.5e and 4.5f, even when having nearly identical mass as in the case of Ag and Pd. The latter is mainly due to slightly different interactions between Pd and Ag atoms, which leads to a higher density of Pd NPs as compared to Ag NPs. Also, there is a stronger interaction between Pd NPs and the CNT, as the C-Pd equilibrium distance is smaller than that of C-Ag. The different induced local strain (where the NP is bonded to the CNT) causes a subtle yet distinctive difference in the elastic properties of the tube. Moreover, the two-dimensional CNT motion also relates to the properties of the nanotube, since different 2D trajectory patterns and envelope frequencies are also observed for CNTs of different chiralities.

The quality (Q) factor of the CNT-NP device can be determined by measuring the number of oscillations corresponding to the attenuation of the CNT vibrations. By increasing the electric field we found that the Q factor

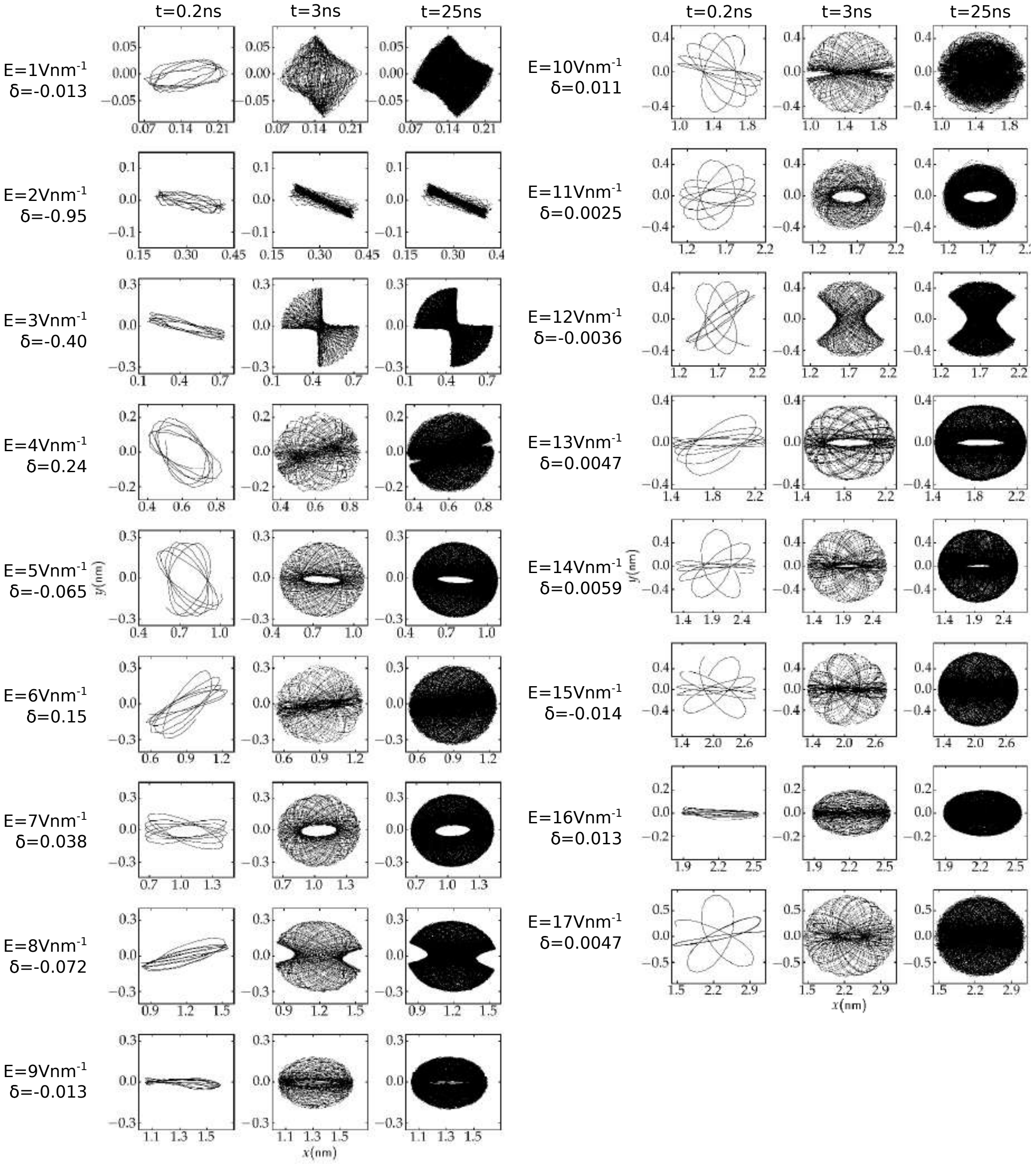

FIGURE 4.4. A sequence of plots showing the evolution of vibrational patterns of a (5,0) CNT with a ring-shaped Ag NP with time and electric field. $\delta = \langle u_x(t)u_y(t)\rangle$ indicates the variations in the correlation between linear ($|\delta| = 1$) and perpendicular ($\delta = 0$).

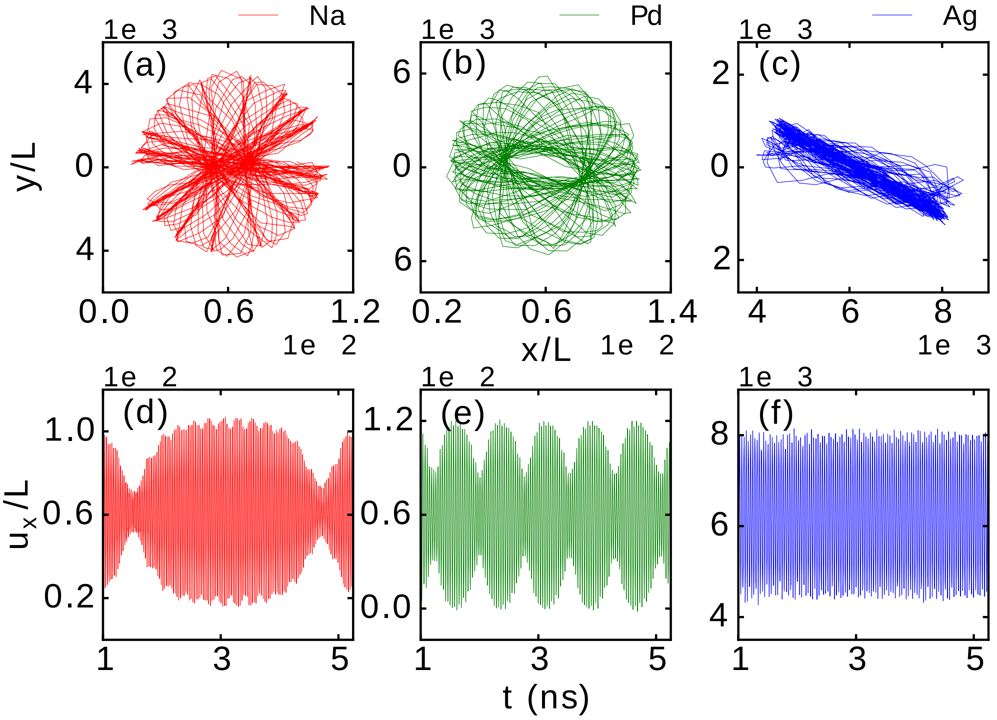

FIGURE 4.5. The path of vibrational motion in the (x,y) plane of the midpoint of a (5,0) CNT with $L = 50$ nm, subjected to the electric field $E = 2\,\mathrm{Vnm}^{-1}$ during $t = 3$ ns and decorated with a Na (a), Pd (b) and Ag (c) ring-shaped NP of 100 atoms and $q = 1e$. The corresponding relative deflection u_x/L as a function of time is shown in panels (d), (e), and (f), respectively.

decreases, e.g., a (5,0) CNT decorated by a dot-shaped Ag NP ($N = 50$, $q = 1$e) shows a decrease in the Q factor from $Q = 3.5 \times 10^4$ to $Q = 7.6 \times 10^3$. Furthermore, by increasing N we found decreasing Q, e.g., the Q factor of a (4,2) CNT decorated with a dot-shaped Ag NP decreases from $Q = 6.5 \times 10^4$ for $N = 20$ to $Q = 7.0 \times 10^3$ for $N = 150$. These results are in agreement with Ref. 129. In the case of CNTs decorated with ring-shaped NPs, we did not find significant attenuation in the CNT vibrations during our simulation time of $t = 25$ ns, confirming the possibility of achieving higher Q factors [130, 131].

We emphasize that a pristine CNT has thermal vibrations at finite temperature. On the other hand, an external electric field induces charge on CNTs. By applying an electric field (in the absence of a NP), a corresponding electrostatic force is distributed along the CNT instead of a central localized force (when a charged particle is located at the midpoint of a neutral CNT).

Therefore, the 2D vibrations and trajectory patterns of a pristine CNT are expected to be different than that of a decorated CNT. We depict the relative deflections u_x/L and u_y/L of a pristine (5,0) CNT as a function of time in Fig. 4.6a and 4.6b, where a net charge q = 1e distributed over the CNT is subjected to $E = 5\,\mathrm{Vnm}^{-1}$. We found different time evolution in comparison to the deflections of a (5,0) CNT decorated by a ring-shaped Ag NP (N = 100, q = 1e), shown in Fig. 4.3f. For a pristine (5,0) CNT, initially the deflections in the x-direction are four times larger than those in the y-direction. The trajectory pattern for a pristine CNT during a simulation time under 3.5 ns is shown in Fig. 4.6c. However, the deflections in x and y directions reach the same order of magnitude at a later time. The trajectory pattern for 17ns – 20ns (Fig. 4.6d) shows that the deflections for the pristine CNT can be even 3 times smaller than the deflections of the decorated CNT (see Fig. 4.3c). As seen in Fig. 4.6c, 4.6d and 4.3c, the trajectory patterns for a pristine and a decorated CNT are clearly different. Furthermore, the pristine CNT yields $u_0/L \approx 7.7 \times 10^{-3}$, while for the decorated CNT $u_0/L \approx 1.5 \times 10^{-2}$. Such differences also impact the resonance frequency of vibrations, e.g., the pristine CNT has a resonance frequency of about 35 GHz for $E = 5\,\mathrm{Vnm}^{-1}$, while a frequency of 27 GHz was obtained for the decorated CNT.

4.3.3 Resonance frequency

Although we show there exist two frequencies characterizing the 2D vibrations, we found that the conventional frequencies (ω_x) remain well described by traditional models. The frequency of vibrations along the x axis can be approximated as [88, 153]

$$f_x = \frac{\omega_x}{2\pi} \approx \frac{1}{2\pi}\sqrt{\frac{192YI}{mL^3}} + \sqrt{\frac{T}{4mL}}, \tag{4.13}$$

where $m = 0.375m_0 + M$ is the effective mass, with m_0 and M being the mass of the CNT and the NP, respectively. Obviously, f_x should decrease with increasing L. The variation of f_x with L for three different CNTs is shown as data symbols in Fig. 4.7a for the case of a dot-shaped Ag NP with 50 atoms and q = 1e and E =0. We found that f_x still decreases with L when an electric

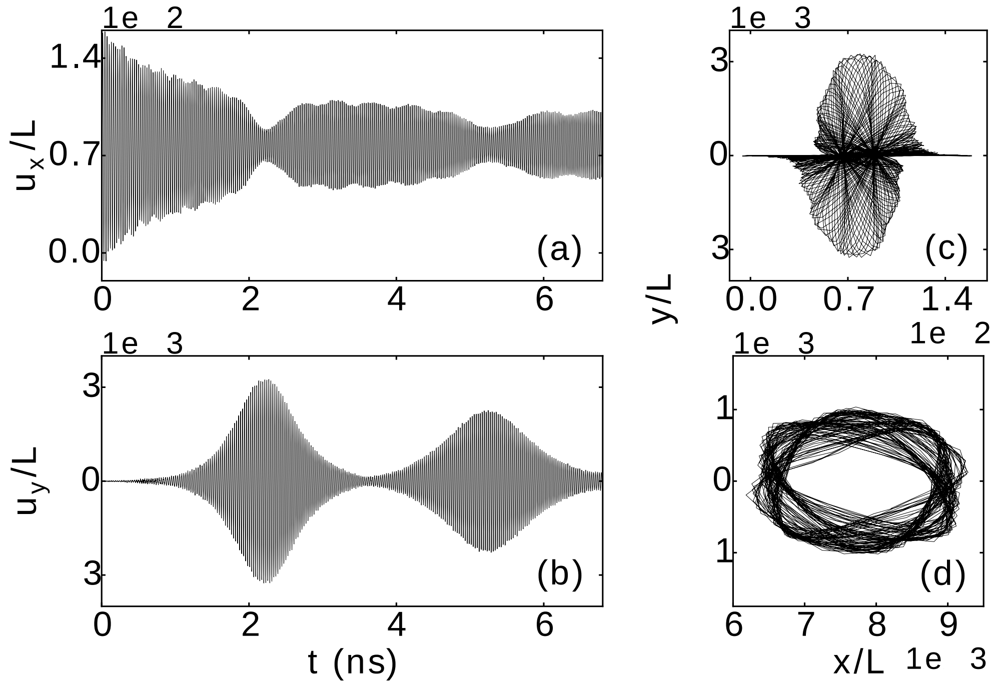

FIGURE 4.6. The variation with time of the relative deflections (a) u_x/L and (b) u_y/L, and the corresponding path of vibrational motion in the (x,y) plane of the midpoint of a pristine (5,0) CNT with $L = 50\,\mathrm{nm}$, $q = 1\,\mathrm{e}$, and subjected to the electric field $E = 5\,\mathrm{Vnm}^{-1}$, for a simulation time (c) under 3.5 ns and (d) in the period 17ns-20ns.

field is applied, as shown in the inset of Fig. 4.7a for the (5,0) CNT subjected to $E = 2\,\mathrm{Vnm}^{-1}$. The plotted lines are fits according to the functional dependence $c_3\sqrt{L^{-3}} + c_4\sqrt{L^{-1}}$ (notice that $T = c_1$ for $E = 0$).

The fit in Fig. 4.7b is made according to $f_x \propto 1/\sqrt{0.375m + \mu N}$, which explains very well the found behaviour of f with the number of atoms in the NP. Interestingly, the same fit holds for all three considered chairalities of the CNT with Ag NP, with a 10% spread on the value of $\mu \approx (94 - 112)$. There are distinct shifts in the found frequency of vibrations for different CNTs, as shown in Fig. 4.7a and 4.7b, which are clearly enabling one to identify the chirality of the CNT. Furthermore, we also found frequency shifts when the atomic element or the overall mass of the NP was changed, for a given CNT. For instance, we found a frequency shift of about 1 GHz for two NPs with $M \approx 5.5\,\mathrm{zg}$, but made of either 150 Na or 30 Ag atoms. For NPs with

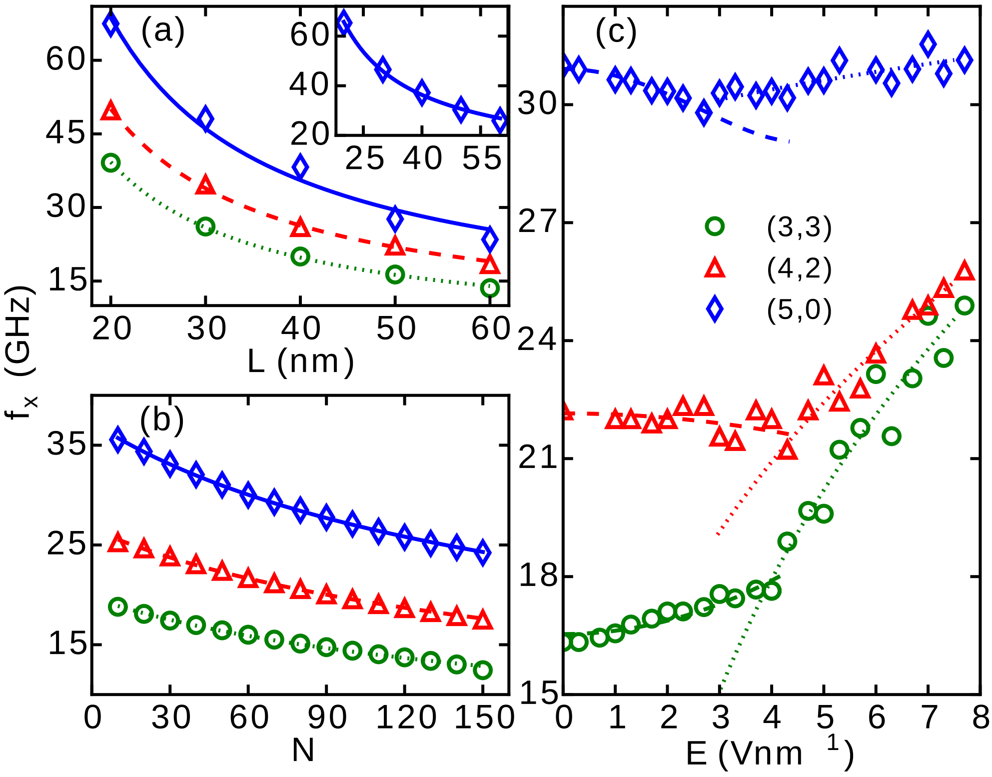

FIGURE 4.7. The variations of resonance frequency f_x with (a) length (L) of three different CNTs, (b) number of atoms in the NP (N) and (c) applied electric field (E). All CNTs were decorated with a dot-shaped Ag NP (q = 1e). In (a) and (b) E=0 while for the inset of panel (a) E =2 Vnm^{-1}. In (b) and (c), L = 50 nm and in (a) and (c), N = 50. The lines plotted in (a) and (b) are fits using Eq. (4.13). The dashed and dotted lines in (c) are the fits obtained using empirical dependencies [see text].

150 atoms, a frequency shift of about 10 GHz was observed for the Na NP in comparison to Ag and Pd NPs (we note that the dependence of deflection $u_0(E)$ for given number of atoms in the NP did not show significant difference for different elements, see Fig. 4.1d). Finally, for NPs made of the same element, e.g. with 10 and 20 atoms of Ag ($\Delta M \approx$2 zg), the frequency shift is found to be ~1 GHz. Such high sensitivity of our device is therefore rendered promising for mass-sensing applications, especially since the vibrational frequencies of CNTs above 1 GHz are readily experimentally detectable [127, 129, 154]. We note here that, since we neglected the polarization effects of the tubes, we expect similar results for non-metallic actin-filaments decorated with charged

metallic NPs [155], which yields a broader outlook of our analysis in the present paper.

The variations of f_x with E are more complicated. For three different CNTs, the MD data as a function of E is shown by symbols in Fig. 4.7c. By increasing E, one observes that transitions occur where $f_x(E)$ changes slope. We attribute this transition to the stretching becoming dominant over the bending regime [110]. The transition field E_t also varies with the CNT's chirality, e.g. larger E_t was found for the (3,3) and (4,2) CNTs than for the (5,0) CNT. The transition can also shift with the number of atoms in the NPs, e.g. the (5,0) CNT decorated with a ring-shaped Ag NP (N =100, q = 1e) has a transition field E_t ≈6 Vnm^{-1}, while E_t ≈3Vnm^{-1} for the dot-shaped Ag NP (N =50, q = 1e).

Finally, we find that the behavior of $f_x(E)$ at low field is not the same for the (5,0) and (4,2) (3,3) CNTs, which is not captured by Eq. (4.13). To propose a functional dependence that can account for this behavior, one should consider various possible reasons for frequency attenuation (e.g. due to electric field counteracting the CNT's restoring forces discussed in Ref. [111] as well as upward (higher-order) corrections for the frequency of each regime (see Ref. [112]). We found that the best fits, after adding functional terms corresponding to the latter discussion, are obtained by empirical formulas $\sqrt{1+c_5E^2+c_6E^4}$ for the bending regime ($T \ll YI/L^2$) and $\sqrt{1+c_7E^{2/3}}$ for the stretching regime ($T \gg YI/L^2$), shown respectively by dashed and dotted lines in Fig. 4.7c.

In addition to the frequency of vibrations along the direction of the electric field (f_x) the entangled two-dimensional CNT vibrations present a transverse mode along the y direction with a frequency f_y. In Fig. 4.8, the variations of the two frequencies f_x and f_y with L, N and E are shown for the (5,0) CNT. We found that the variation with length is nearly independent of the direction ($f_y \approx f_x$), as shown in Fig. 4.8a. However, lower f_y was observed when increasing N (see Fig. 4.8b). The variations of the two frequencies with E exhibit significant difference where the transition between the bending and the stretching regime occurs (see Fig. 4.8c), which indicates a more complex vibrational motion than those characteristic of either regime. Similar

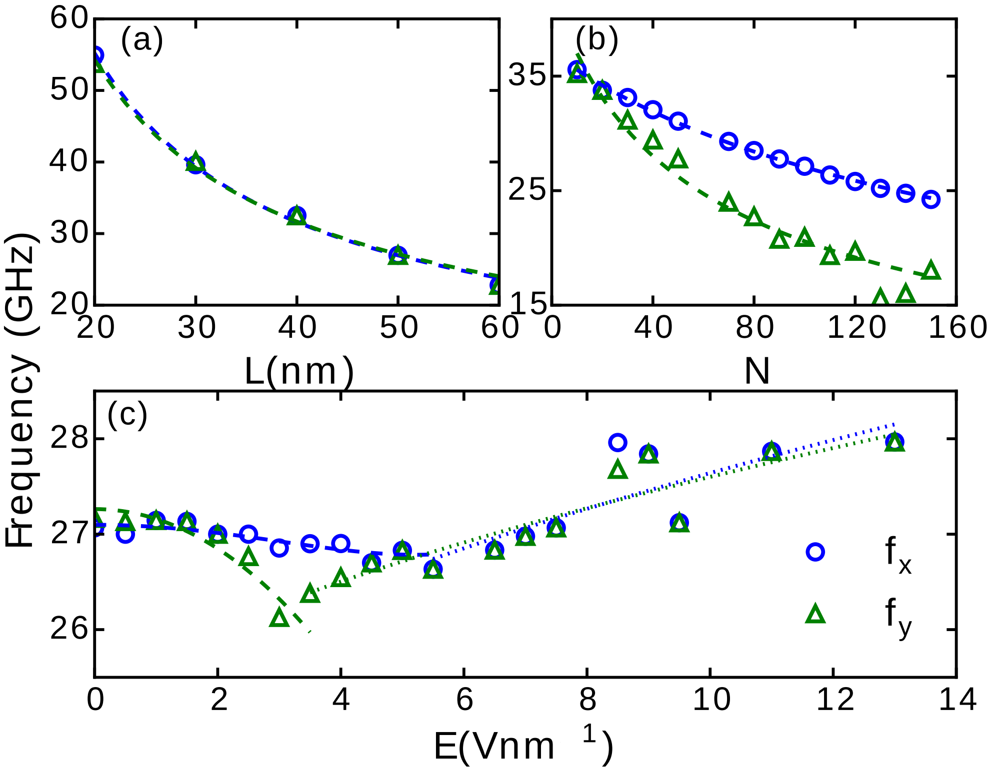

FIGURE 4.8. The variations of f_x and f_y with (a) L, for a ring-shaped NP and $E = 2\,\mathrm{Vnm}^{-1}$, (b) N, for a dot-shaped NP and $E = 0$, and (c) E, for a ring-shaped NP and $N = 100$. In all the panels a (5,0) CNT and a Ag NP (q = 1e) are considered. The lines plotted in (a) and (b) are fits using Eq. (4.13). The dashed and dotted lines in (c) are the fits obtained using empirical dependencies [see text].

difference in the transverse frequency has been previously reported when varying the position of the NP on the CNT [142]. This suggests that symmetry breaking contributes to the attenuation of the transverse frequency, which justifies the difference between f_x and f_y when varying N.

4.4 Conclusions

In summary, we addressed high sensitivity of decorated nanoelectromechanical systems (NEMS) to the microscopic properties of the attached object. The deformations of such device made of a carbon nanotube (CNT) and a metallic nanoparticle (NP) under electric field were spatially mapped. The exhibited trajectory patterns for the two dimensional vibrational motions of the CNT were found to be unconventional and dependent on the strength of the applied electric field. Such 2D motions can not be described by the well known linear Euler-Bernoulli beam-mass theory, but exhibit also an envelope frequency (Ω) which was found to be an order of magnitude smaller than the conventional frequency, thus convenient for experimental detection and analysis. Both the conventional and the modulation frequency were shown to be distinctively sensitive on the CNT geometry and all properties of the NP (shape, element, mass and charge), enabling quite broad sensing applications of this device, and further development of biological/inorganic hybrid devices along similar ideas.

The results of this chapter were published in:

- Belisa R. H. de Aquino, Mehdi Neek-Amal, and Milorad V. Milošević, *Unconventional two-dimensional vibrations of a decorated carbon nanotube under electric field: linking actuation to advanced sensing ability*, Sci. Rep. **7**, 13481 (2017).

Part III

Confined Water

CHAPTER 5

ELECTROSTRICTIVE BEHAVIOR OF CONFINED WATER SUBJECTED TO GPA PRESSURE

Water inside a nanocapillary exhibits unconventional structural and dynamical behavior due to its ordered structure. The confining walls, density and lateral pressures control profoundly the microscopic structure of trapped water. Here we study the electrostriction of confined water subjected to pressures of the order of GPa for two different setups: i) a graphene nanochannel containing a constant number of water molecules independent of the height of the channel, ii) an open nanochannel where water molecules can be exchanged with those in a reservoir. For the former case, a square-rhombic structure of confined water is formed when the height of the channel is $d = 6.5\text{Å}$ having a density of $\rho = 1.42\,\mathrm{g cm^{-3}}$. By increasing the height of the channel, a transition from flat to a buckled state occurs whereas the density rapidly decreases and reaches the bulk density for $d \cong 8.5\text{Å}$. When a perpendicular electric field is applied, the water structure and the lateral pressure changes. For strong electric fields ($\sim 1\,V/\text{Å}$), the square-rhombic structure is destroyed. For an open setup, a solid phase of confined water consisting of an imperfect square-rhombic structure is formed. By applying a perpendicular field, the density and phase of confined water changes. However, the density and pressure inside the channel decreases as compared to the first setup. Our study makes a close relation between recent experiments on confined water and reveals the sensitivity of the microscopic

structure of confined water to the size of the channel, external electric field and experimental setup.

5.1 Introduction

The microscopic structure of confined water has been studied extensively in the past two decades. Water inside a nanocapillary becomes ordered exhibiting unconventional behavior [30, 32, 156–158]. The confinement size (channel height), the internal pressure and the microscopic structure of the confining walls are important factors that determine the microscopic structure of confined water [46, 52, 54, 159–163]. The confining walls can weakly interact with water (hydrophobic) or absorb water (hydrophilic) which results in different orientations of the water molecules near the confining walls [164]. Despite extensive theoretical studies on confined water there are still many unsolved questions such as the exact orientation of the water molecules over different substrates which can provide information on the contact angle of the water droplet [165–168]. The density of water, possible phase transitions and the effects of lateral pressure also are open questions [169–171]. Although there are several reports on the electrostriction of confined water [45, 46, 54, 172], further investigations are needed on the out of plane deformations of a single layer of water in the presence of an external perpendicular electric field.

The main challenges, from a theoretical point of view, are: i) the force fields in molecular dynamics simulations were mostly parameterized using bulk water properties, ii) the weak interactions (dispersion forces), and iii) the limiting computational time restricts us to small systems when using density functional theory calculations. However, many of the main properties of confined water can be understood using classical force fields [161, 162]. There are several reports on the electrostriction of confined water and the possible electric field induced liquid to gas phase transition [46, 172]. Classical thermodynamics predicts an increase in the density of bulk liquid when subjected to a weak external field [173], i.e. $\frac{\delta\rho}{\rho} \propto E^2$. However for confined water inside an open channel and subjected to an electric field evaporation was predicted [172]. This might be due to metastable phases of confined water [172].

Here by using the art of molecular dynamics (MD) simulations we study the microscopic structure of a single layer of water confined between two graphene sheets subjected to a pressure of about 1 GPa for two different setups: i) a graphene nanochannel containing a fixed number of water molecules, and ii) an open nanochannel which exchanges water molecules with a reservoir via both sides. These setups are relevant for recent experiments [29, 174]. We study possible phase transitions and concomitant changes in the density and lateral pressure. Different setups lead to different kinds of structural deformation of confined water. By applying a *perpendicular* electric field the dipole moment of the water molecules reorient resulting in variations in the H-bond network and a structural deformation of confined water. The buckling height varies with the channel height and with the strength and orientation of the external electric field. In our previous work [54], we studied the hysteresis in the polarization of confined water in the presence of an *in-plane* electric field and found structural transitions which are very different from those reported here (i.e. ordered to disordered phase) for perpendicular electric field.

5.2 Model and methods

We employed atomistic molecular dynamics (MD) simulations implemented in the LAMMPS package [83]. We used the water model TIP4P [73] for water-water interaction. The graphene-water interaction was modeled by the Lennard-Jones (LJ) potential, with $\epsilon_{C-O} = 0.0949\,\mathrm{eV}$ and $\sigma_{C-O} = 3.28\,\text{Å}$. In order to calculate the lateral (p_{xy}) and transverse pressure (p_z), we calculated the stress tensor of water molecules inside the channel:

$$\hat{\sigma} = \begin{pmatrix} \sigma_{xx} & \sigma_{xy} & \sigma_{xz} \\ \sigma_{yx} & \sigma_{yy} & \sigma_{yz} \\ \sigma_{zx} & \sigma_{zy} & \sigma_{zz} \end{pmatrix}, \tag{5.1}$$

with $\sigma_{ab} = \sigma_{ba}$ and $a, b = \{x, y, z\}$, i.e., the stress tensor is symmetric, where σ_{aa} (σ_{ab}) are the normal (shear) components. The aforementioned pressures can be written as

$$p_{xy} = -\frac{\langle \sigma_{xx} \rangle + \langle \sigma_{yy} \rangle}{2}, \tag{5.2}$$

$$p_z = -\langle \sigma_{zz} \rangle, \tag{5.3}$$

where $\langle\ \rangle$ denotes the ensemble average. The stress tensor components are calculated by summing the kinetic energy contribution to the energy contribution due to the interactions of each atom, i.e.,

$$\sigma_{ab} = -\frac{1}{V} \sum_{i=1}^{N} \left[m_i v_{i,a} v_{i,b} + r_{i,a} F_{i,b} \right], \tag{5.4}$$

where $F_{i,b}$ considers the contribution of pairwise interactions, bonds and angles constraints, long-range Coulombic interactions required by the TIP4P model and external applied forces such as the electrical force [84, 175]. In Eq. (5.4), $V = A\,\bar{d}$ is the effective volume of the channel between two graphene sheets with area A separated by a distance d. The effective distance is defined by $\bar{d} = d - \sigma_{C-O}$, where $\sigma_{C-O} = 3.28\,\text{Å}$ is a measure of the excluded volume due to the water-wall interaction. More details on pressure calculations of inhomogeneous quasi-two-dimensional systems can be found in the Appendix of Ref. 176.

5.2.1 Constant number of water molecules: model A

First, we simulate a single channel of graphene which contains a fixed number of water molecules (see Fig. 5.1). The simulation system consists of a computational unit cell with 840 water molecules confined between two AB-stacked graphene sheets with a total of 5120 carbon atoms and separated by a distance d. Top and two side views of our system for two different channel heights are shown in Figs. 5.1(a-c). The initial structure of confined water is a square lattice of O atoms with lattice constant $2.8\,\text{Å}$ and a random distribution of H bonds. Periodic boundary conditions were applied in the xy-plane. We set the computational unit cell to be commensurate with the graphene lattice [54]. We performed NPT simulation annealing, using a Nosé-Hoover thermo/barostat to obtain the correct simulation box and inter-atomic distances. After cooling down the system to nearly zero Kelvin, a square-rhombic ice structure is obtained at a pressure of 0.15GPa. This pressure is

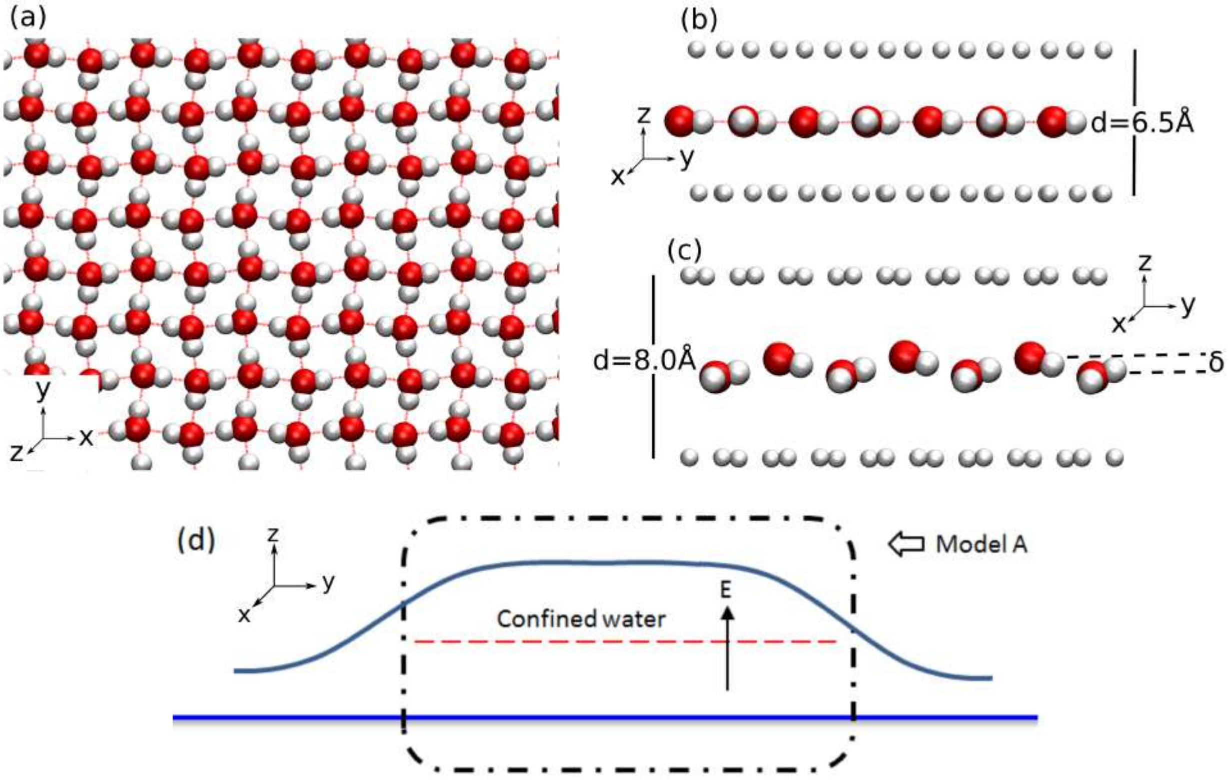

FIGURE 5.1. Model A: Constant number of molecules inside a graphene nanochannel. The square-rhombic lattice for confined water is shown in (a). Red (white) balls are O (H) atoms of the water molecules. In (b, c), side view for two different interlayer distances, $d = 6.5\,\text{Å}$ and $d = 8\,\text{Å}$, with buckling height δ. In (d) a schematic view of the nanoclosure filled by a single layer of water is shown. The dashed rectangle refers to the middle portion of the nanobubble which is relevant to our model A.

in good agreement with previous reports from several groups [54, 161]. Annealing the system up to nearly zero Kelvin temperatures allows the system to reach a stable configuration. The obtained structure is in agreement with the minimum energy configuration obtained in our previous work [54]. Then, an NVT ensemble is adopted using a Nosé-Hoover thermostat in order to preserve the constant volume while an electric field is applied perpendicularly to the graphene sheets. Here, a time-dependent perpendicular electric field is applied in order to obtain the time-dependent evolution of the system. The electric field is varied with a rate of change of $40\,\text{VÅ}^{-1}\text{ns}^{-1}$ while the system, which is at $T = 1\,\text{K}$, stays in thermodynamic equilibrium. A similar procedure was adopted and described in our previous work with in-plane electric field [54], where rates of the same order of magnitude were used and the effects of the rate of change on the hysteretic behavior of confined water was investigated. We will show that a very strong perpendicular electric field, in the range [-3, 3] V/Å, will change the microscopic structure of water. Initially, we consider a monolayer of water inside a channel with $d = 6.0$ Å [52, 54, 161]. Subsequently, we increase d in order to elucidate the effects of the channel height on the water layer.

The above system (model A) containing constant number of molecules is typically realized in graphene bubbles (see Fig. 1(d)) [174]. The number of molecules is constant in the system shown in Figs. 1(b) and 1(c). Our setup corresponds to a perfect nanobubble while in a real nanobubble there are often terraces at the edges of the nanobubble [161] which are not included in our model A. In fact, model A corresponds to the middle portion of the nanobubble as indicated by the dashed rectangle in Fig. 1(d).

5.2.2 Open system: model B

A different system (model B) that has been investigated experimentally [29] consists of a nanochannel connected to one reservoir via both sides (in Fig. 5.2, a channel with $d = 7.0$ Å is shown). In fact the channel is made by removing a single layer of graphene from bulk graphite. Recently, Radha *et al.* successfully fabricated such nanochannels [29]. In order to model the experimental setup, we considered a graphene nanochannel immersed in a water reservoir in the NPT ensemble, where the temperature, pressure and subsequently density of water inside the reservoir is controlled by using a Nosé-Hoover thermo/barostat. Here the confined system is open from both sides and exchange of water molecules with the reservoir is possible. The temperature is kept constant at room temperature. Periodic boundary conditions were applied along the z(y) direction in the reservoir (channel). We found that weaker electric fields (compared to model A) are required to change the microscopic structure of confined water (~ 0.5 V/Å).

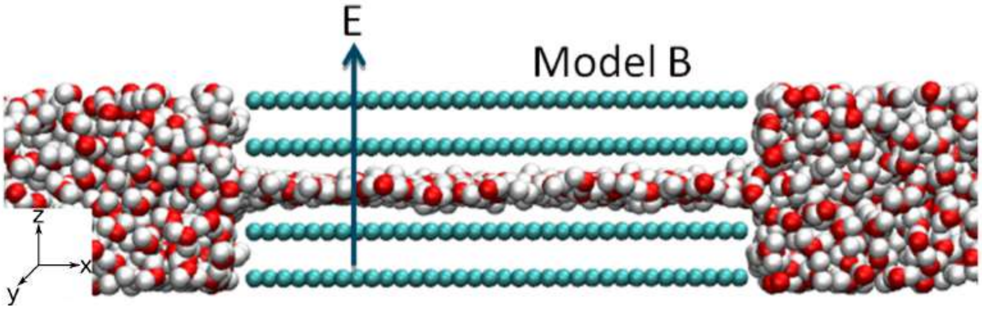

FIGURE 5.2. Model B: An open graphene nanochannel that can exchange water with the reservoir. The electric field is only applied in the channel region.

5.3 Results: model A

First we report results for a periodic system which contains a constant number of molecules. This model has recently been widely used in several ab-initio studies [53, 177, 178]. Here we report minimum energy configuration of the confined single layer of water inside the channel subjected to a perpendicular electric field.

5.3.1 Microscopic structure: density and buckling

Our annealing MD simulations for confined monolayer water between two graphene sheets separated by distances in the range $d = (6.0-8.5)$ Å led to a square-rhombic water monolayer, as depicted in Fig. 5.1(a) with flat and buckled structure, for $d = 6.5$ Å and $d = 8.0$ Å (buckling height $\delta = 1.8$ Å), respectively. The confinement induces structural deformation on the water structure, e.g. by increasing d from $d = 6.5$ Å to $d = 8$ Å, water molecules spontaneously expand to the larger available space yielding a transition from flat to a buckled structure. Transitions to buckled phases have been already investigated and reported for similar systems [179]. The transition from a flat to the buckled state by increasing d is identified as two peaks appearing in the density profile of oxygen (O) atoms along the z direction which are shown in Fig. 5.3 for $d = 6.0$ Å, $d = 7.25$ Å, and $d = 8.5$ Å. In the former case, the O-atoms are narrowly distributed around $z = 0$ while in the two latter cases

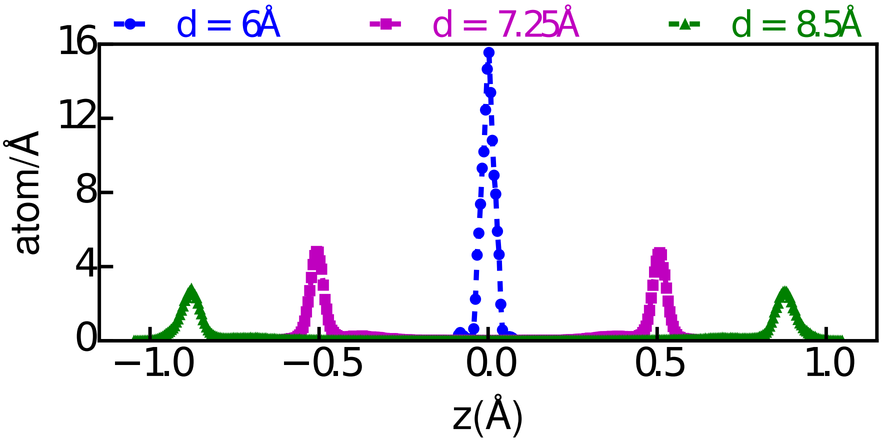

FIGURE 5.3. The density profile of oxygen atoms along z direction for three different graphene interlayer distances d.

two peaks are located at $z = \pm 0.5$ Å and $z = \pm 0.9$ Å, respectively. The buckling height δ varies with channel height d and the peaks have a larger variance and larger separation for larger d.

The dependence of δ on d and water density ρ are shown in Fig. 5.4. The transition from flat state ($\delta = 0$) to the buckled state ($\delta \neq 0$) occurs at $d \approx$ 6.6 Å. For $d \geq 6.6$ Å, the buckled structure is determined by the competition between the different interactions in the system and δ increases nonlinearly with d reaching 1.75 Å when $d = 8.5$ Å, see Fig. 5.4. For $d > 8.5$ Å, the single buckled layer structure no longer exists and a bilayer of confined water is formed. The water density is defined as $\rho = m/v$, where m is the total mass of the water molecules and v is the effective confined volume as defined in Sec. 5.2 [170]. As seen from Fig. 5.4, ρ decreases with d starting from high density 1.42 gcm^{-3} to about 1 gcm^{-3}. In fact the square-rhombic structure corresponds to a high density of water which can be considered as a new dense phase of ice. Notice that the experimental confirmation of square ice is still controversial [180].

The water structure reported in our study is similar to that reported in Ref. 46, although a denser triangular lattice structure for the confining walls with lattice constant 2.3Å was used (as compared to our used hexagonal lattice of graphene). Moreover, the pressure values which were reported in Ref. [46] are very different from ours (see below). The buckling heights obtained here

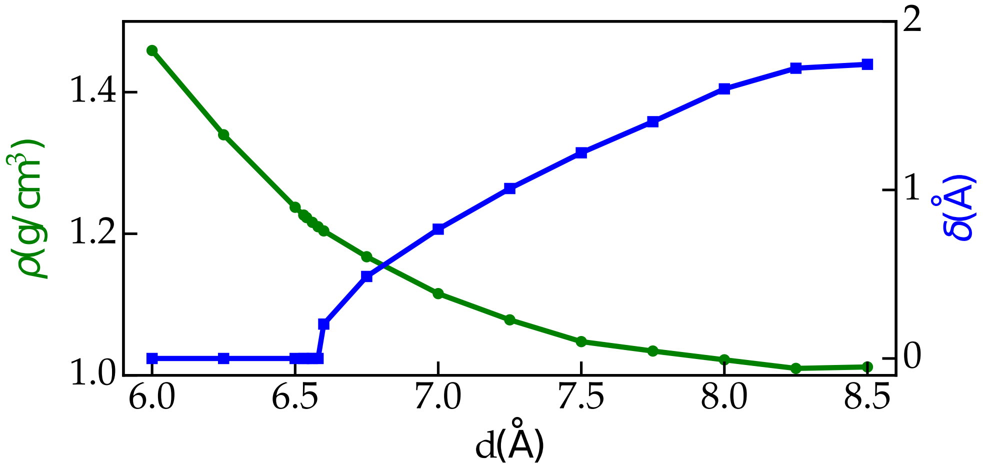

FIGURE 5.4. The variation of buckling height δ (right scale) and density (left scale) ρ with channel height d. For $d = 6.6$ Å, the transition from flat to buckled state occurs.

[see Fig. 5.4] are also in line with Ref. [46], e.g., for $d = 7.9$ Å we obtained $\delta = 1.54$ Å.

5.3.2 The effects of perpendicular electric field

By applying a perpendicular electric field E (along z direction), the electric force exerts a torque on the water molecules and causes the dipole moments of the water molecules to align with E. Consequently, the square-rhombic lattice structure of the single layer of water is destroyed. Notice that as the initial ordered structure (of O atoms) is lost, the buckling height δ is not a well defined parameter. Therefore, we define the parameter h as the portion of the channel height that is occupied by the O atoms (see Fig. 5.5(a)). For instance for $d = 6$ Å $h = 0$ (flat) while for $d = 7.25$ Å and $d = 8.5$ Å we found $h = 1.0$ Å and $h = 1.75$ Å, respectively. The variation of h with applied electric field is shown in Fig. 5.5(b) for three different d values. The larger d the smaller the critial electric field E_c at which the H-atoms move out of plane, because of larger degree of freedom of water. Generally, h increases with electric field until it reaches a maximum. By analyzing the maximum value of h for each d we found that the minimum distance between the water molecules and the graphene sheets is about ~ 2.75 Å, which is in

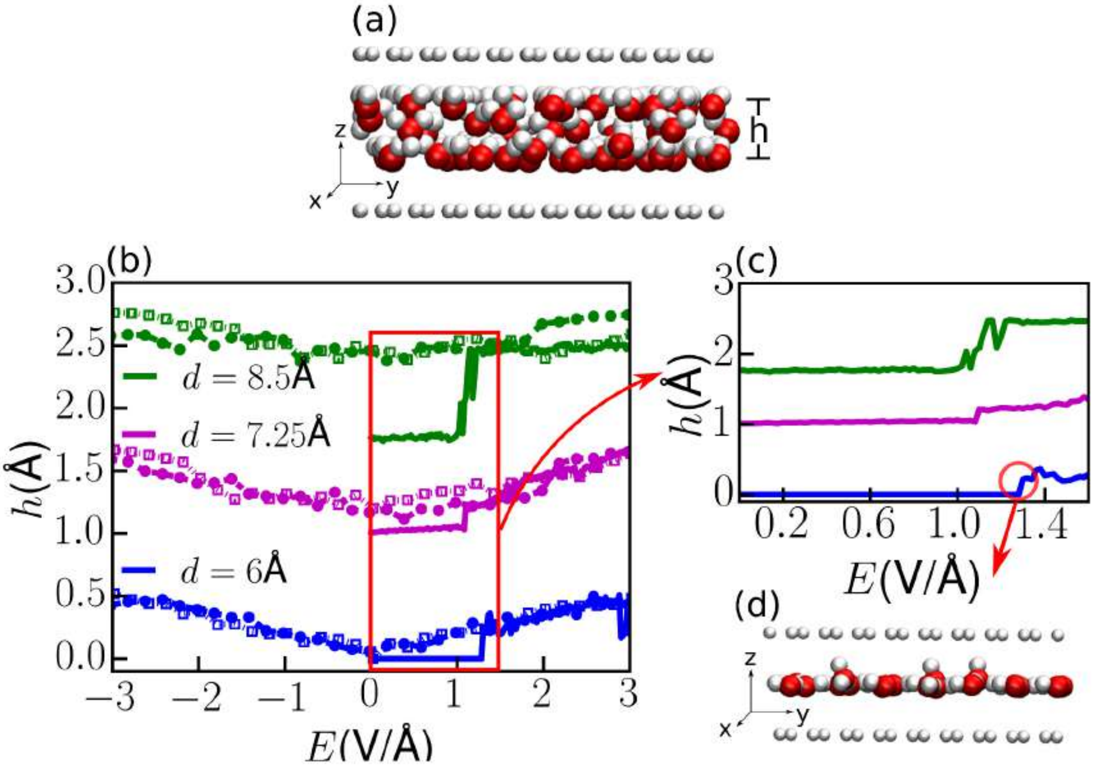

FIGURE 5.5. Side view of confined water for $d = 8.5\,\text{Å}$, where the shift of O-atoms in the z-direction is denoted by h (a). The variation of h with E for different d. The solid line corresponds to the increase of E from 0 to 3 V/Å. The circles (squares) corresponds to the decrease (increase) of E from 3 (-3) to -3 (3) (b). In (c) we show the solid line in the zoomed region. (d) Side view of the water monolayer for $d = 6.0\,\text{Å}$ indicates that the hydrogen atoms are oriented in the transverse direction when $E = 1.3$ V/Å.

agreement with our previous results [162]. By increasing the electric field above a threshold value ($E_c = 1.35$ V/Å for $d = 6$ Å), the torque exerted by the electric force flips the water molecules resulting in a sharp increase of h (see Figs. 5.5(c, d)). Sudden change in the water structure due to an increase of electric field was previously reported in Ref. 46.

The alignment of water molecules with electric field generates a nonzero polarization Q_z (i.e. net dipole along z-direction), which increases more rapidly for larger d values. For weaker fields ($E < E_c$), the semi-flat structure remains unchanged and the total dipole moment varies linearly with E. In this quasi-linear regime one can write $Q_z \approx \chi E$ where χ is the polarizability of water. For

$d = 6.0\,\text{Å}$ ($7.25\,\text{Å}$), $\chi \sim 2.38 \times 10^{-22}\,\text{Cnm}^2/\text{V}$ ($\chi \sim 2.46 \times 10^{-22}\,\text{Cnm}^2/\text{V}$), which is two times larger than the polarizability of bulk water [181]. The reason the polarizability in the bulk is smaller is because the water molecules are surrounded in all directions by other water molecules imposing orientations to establish hydrogen bonds different than the orientation dictated by the external electric field. In the slab confinement, there are only water molecules nearly in the same plane that can oppose the orientation of the electric field [179]. However, for $E > E_c$ the water molecules evolve to the out-of-plane space resulting in a deformation of the initial ordered and semi-flat structure with an enhancement in the nonlinearity. The variation of $\langle \tilde{Q}_z \rangle$ with E after loosing the initial planar structure is shown in Figs. 5.6(a-c) for $d = 6.0\,\text{Å}$, $d = 7.25\,\text{Å}$ and $d = 8.5\,\text{Å}$. Here, $\langle \tilde{Q}_z \rangle = \sum_i^N \frac{Q_{z,i}}{Q_i}$, where N is the number of water molecules in the channel, Q_i is the dipole moment of the ith molecule and $Q_{z,i}$ is the component of Q_i in the z direction. We found a hysteretic behavior which depends on the graphene interlayer distance d. Such hysteresis is different from the previously reported one for applied in-plane electric field, i.e. in our previous work a larger area under the Q_z versus E curve was observed. Also in an previous work a smaller electric field was needed to reach the maximum dipole moment [54].

We found a significant response of the single layer of water to the applied perpendicular electric field. This can be noticed by comparing the density profiles of the O atoms along the z-axis obtained before applying electric field, shown in Fig. 5.3, and Figs. 5.6(d-i), which show the density profile of O-atoms when Q_z is maximum, i.e., $\langle \tilde{Q}_z \rangle \sim 1$ and when the system reaches $Q = 0$ again by decreasing E. When $d < 6.6\,\text{Å}$, the initial flat water structure obtained at $E = 0$ becomes buckled when $\langle \tilde{Q}_z \rangle \sim 1$. The result for $d = 6.0\,\text{Å}$ is shown in Fig. 5.6(d), where the density profile of O atoms represents two peaks at $z = \pm 0.3\,\text{Å}$. The top and side views of the water structure for $d = 6.0\,\text{Å}$ when Q_z is maximum are shown in Fig. 5.7(a). The top view corresponds to an ordered structure (quasi-rhombic lattice), while the side view shows a buckled structure, where neighboring water molecules are perpendicularly oriented with respect to each other. When the system is restored to $Q_z = 0$ the O atoms return to the plane occupied before applying E (see Figs. 5.3 and 5.6(e))

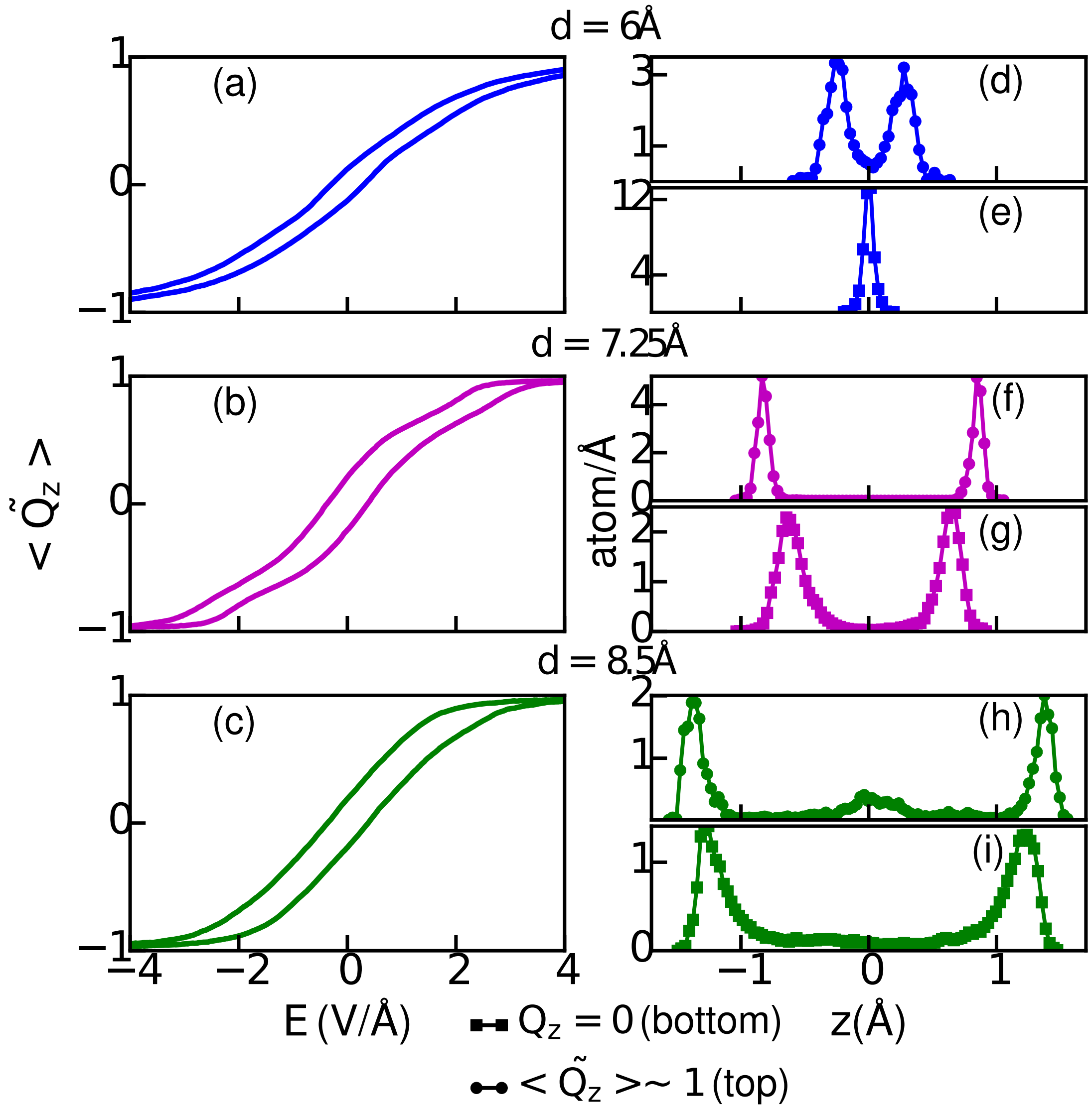

FIGURE 5.6. The variation of the z-component of the net dipole moment $\langle \tilde{Q}_z \rangle$ with E for (a) $d = 6.0\,\text{Å}$, (b) $d = 7.25\,\text{Å}$ and (c) $d = 8.5\,\text{Å}$. The corresponding density profiles of O-atoms along z direction when $\langle \tilde{Q}_z \rangle \sim 1$ (top figures) and when the system recovers $Q_z = 0$ (bottom figures) are shown in panels (d-i).

but the initial square-rhombic structure is no longer found (an amorphous structure appears). The top and side views of the confined water structure for $d = 6.0\,\text{Å}$ when the system is returned to $Q_z = 0$ by decreasing E is shown in Fig. 5.7(b). The top view shows that some defects are found while the O atoms tend to recover their initial square-rhombic structure corresponding to a larger standard deviation in the density profile of O atoms. Nonetheless,

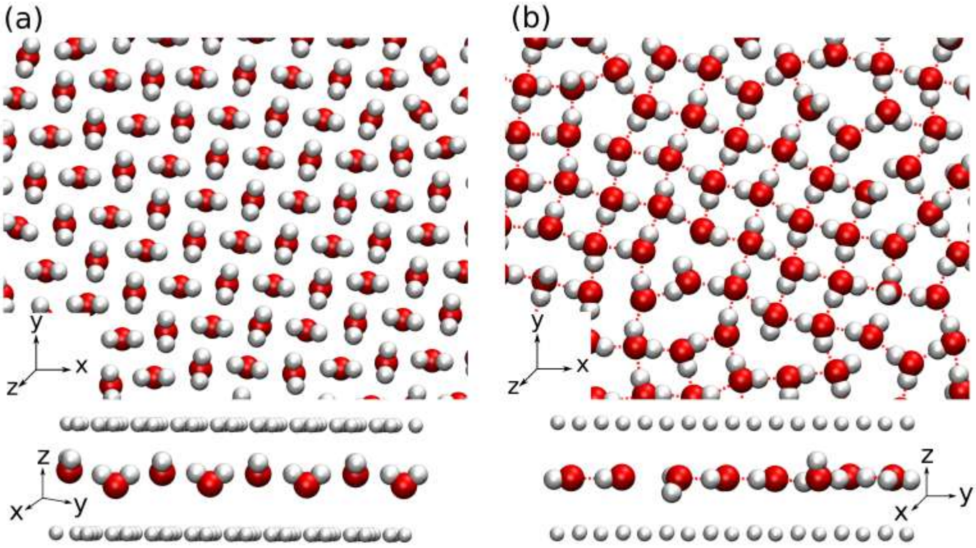

FIGURE 5.7. Top and side views of monolayer confined water for $d = 6.0\,\text{Å}$ and (a) $\langle \tilde{Q}_z \rangle \sim 1$ and (b) when the system returns to $Q_z = 0$.

the side view in Fig. 5.7(b) shows a nearly flat structure, although there are a few H-atoms parallel to the transverse z direction directed up or down (notice that O atoms are slightly displaced). When $d \geq 6.6\,\text{Å}$, the channel height is wide enough to favour the formation of buckled monolayer water, as discussed previously. However, a different buckled structure with a more pronounced buckling is obtained when Q_z is maximum. This is shown in Fig. 5.6(f), where the density profile along the z-axis for $d = 7.25\,\text{Å}$ indicates that the O atoms are located at $z = \pm 0.85\,\text{Å}$ in comparison to the two planes centered at $z = \pm 0.5\,\text{Å}$ before E is applied (see Fig. 5.3). When the electric field is decreased and the system reaches $Q_z = 0$ again, the O atoms occupy two planes located at $z = \pm 0.6\,\text{Å}$, as shown in Fig. 5.6(g)). In the case of larger d, e.g. $d = 8.5\,\text{Å}$, when Q_z is maximum the region between the water planes exhibits a third smaller peak in the density profile of O atoms centered at $z = 0$ (see Fig. 5.6(h). When the system returns to $Q_z = 0$, the O atoms are located at $z = \pm 1.1\,\text{Å}$(see Fig. 5.6(i)) instead of being at $z = \pm 0.9\,\text{Å}$ for the initial square-rhombic buckled structure (see Fig. 5.3).

In Ref. [46], the O atoms are shifted downward when an electric field is applied. Therefore, the position of the planes slightly differ from those

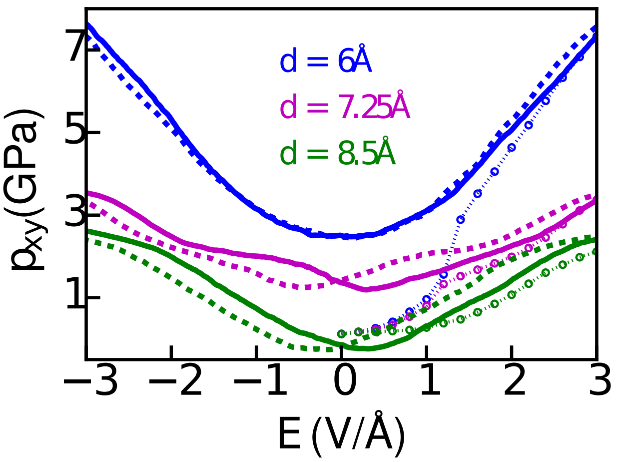

FIGURE 5.8. The variation of the lateral pressure p_{xy} with E. The dotted line with circles corresponds to the increase of E from 0 to 3 V/Å. The dashed (solid) line corresponds to the decrease (increase) of E from 3 (−3) to −3 (3).

observed in our simulations (this might be due to including the interaction between the H-atoms and walls in Ref. [46]). However, the water structures and buckling heights reported here for different applied electric fields (and polarizations) are qualitatively in agreement with those of Ref. [46], e.g. a distance of ~ 2 Å between the two planes occupied by the O atoms is reported for $d = 7.9$ Å and $E = 0.5$ V/Å, when the reported water structure was similar to the structure shown in Fig. 5.7(a).

5.3.3 The effects of lateral pressure

Here we show that the lateral pressure in model A is always of the order of GPa although in previous work it was reported to be about 1 bar [46]. Figure 5.8 shows the variation of the lateral pressure p_{xy} with applied E. The lateral pressure p_{xy} increases with E until it reaches a maximum value (p_{xy}^{m}). The maximum obtained lateral pressure varies significantly with d. In fact, we found $p_{xy}^{\mathrm{m}} = 12$ GPa for $d = 6.0$ Å, while $p_{xy}^{\mathrm{m}} = 3.0$ GPa for $d = 8.5$ Å. Besides a hysteretic behavior which becomes more prominent when increasing d is observed. The latter can be seen by comparing the solid and dashed curves in Fig. 5.8 corresponding to increasing and decreasing field, respectively. We found that for $d = 6\,\text{Å}$, $p_{xy} \propto \alpha E^2$, with $\alpha = 8.4 \times 10^{-2}$ C/m^2. The non-parabolic shape observed for $d = 7.25\,\text{Å}$ is related to changes in the water structure.

It is interesting to note that, since the density of the system for a given d is constant by increasing the electric field, $\delta\rho = 0$ while $\delta p_{\text{tot}} \neq 0$. This is beyond the prediction of classical thermodynamics [173], i.e. $\frac{\delta\rho}{\rho} \propto E^2$, and is due to the effects of confinement. However, in a system where confined water can exchange molecules with a reservoir, variations in the water density is possible when applying an electric field (see below).

5.4 Results: model B

Hereafter we turn our attention to model B. We first report the microscopic structure of water inside the channel subjected to a pressure of order GPa, then the effects of the applied electric field, pressure and density will be considered.

5.4.1 microscopic structure

The water structure inside the open channel depends significantly on the pressure in the reservoir and applied electric field. In Fig. 5.9 we show different snapshots of confined water inside an open channel where the pressure in the reservoir is kept either at 1 GPa or 1 bar. The confined water at 1 GPa pressure exhibits locally a square-rhombic structure, as observed in model A (see Fig. 5.1(a)). Once the electric field is applied, water molecules are squeezed out from the system under ordinary 1 bar pressure while for the system with GPa pressure only a small decrease in density is observed. The reason for the significant decrease in the density is that the electric field aligns the dipoles of the water molecules in the channel which repel each other. Notice that the electric field is applied only on the water molecules inside the channel and not in the reservoir.

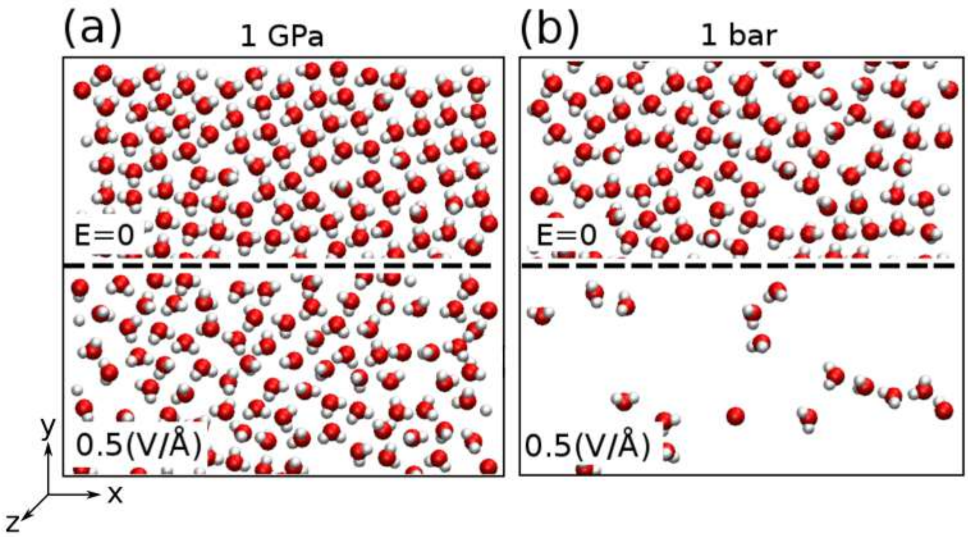

FIGURE 5.9. Four snap shots taken from confined water in the open system where the pressure in the reservoir is kept at 1 bar (a) and 1 GPa (b) and electric field is 0 (top figures) and 0.5 V/Å(bottom figures).

5.4.2 The effects of perpendicular electric field on the total dipole moment and the H-bonds

We keep the pressure of the reservoir of our open system constant at about 1.0 GPa. After equilibrating the system at room temperature, during 0.1 ns, we started to apply a perpendicular electric field on water in the nanochannel at an average rate of 2 VÅ^{-1}ns^{-1}. Figure 5.10(a) shows the variation of the applied field with time with a maximum of 0.5 V/Å after 0.4 ns of simulation. The corresponding increase in the z-component of the net dipole of confined water is shown in Fig. 5.10(b). We found that when the electric field reaches 0.5 V/Å, the corresponding dipole moment is $\langle\tilde{Q}_z\rangle \sim 0.25$ (~ 0.4) for $d = 7$ Å ($d = 10$ Å), while in model A, the dipole found to be $\langle\tilde{Q}_z\rangle \sim 0.12$ for $d = (6-8.5)$ Å. Therefore the field necessary to align the water molecules for this open system setup is smaller than that obtained for model A. Accordingly the number of H-bonds $\langle HB\rangle$ decreases with increasing electric field, see Fig. 5.10(c). It is seen that by increasing the electric field, the wider the channel the larger the number of H-bonds per water molecule. Due to confinement effects, the number of H-bonds here are smaller than for bulk water.

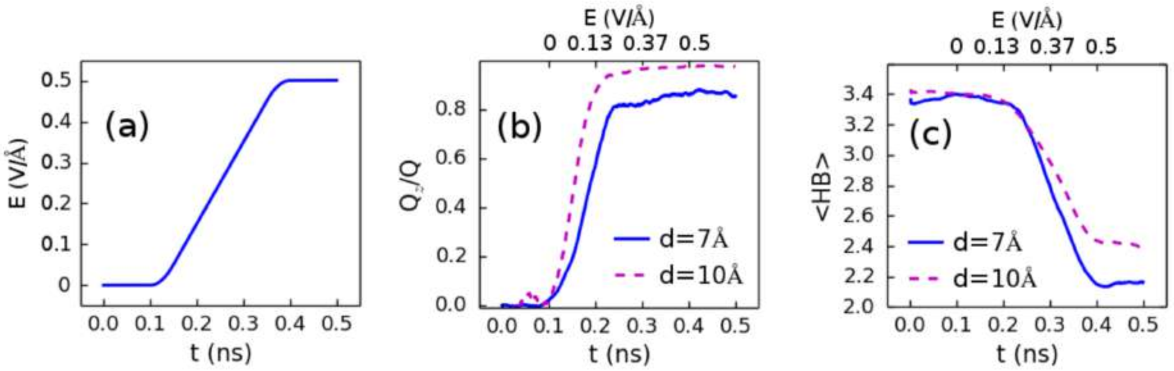

FIGURE 5.10. . (a) The applied electric field reaches 0.5 V/Å during 0.4 ns. (b) The variations of the z-component of the total dipole moment of confined water with time. (c) The variations in the number of H-bonds with time.

5.4.3 The effects of perpendicular electric field: pressure and density

We found that the influence of the applied electric field on the pressure components inside the nanochannel depends on the channel height. Though the lateral pressure (p_{xy}) is almost constant in the channel of size $d = 7$ Å, p_z increases significantly with electric field, as shown in Fig. 5.11(a). However, Fig. 5.11(b) shows that, for $d = 10$ Å, p_z is nearly constant, which makes the decrease in p_{xy} more significant. The different behaviors of p_z with increasing E is due to the smaller available space for water molecules in a channel with height d=7 Å. We conclude that the major role is played by the p_z component for narrower channels. The effects of a perpendicular electric field on the pressure of water confined in an open channel is different from the behavior found for the previous setup (see Fig. 5.8). Moreover, Figs. 5.11(a,b) show that after the electric field reaches a maximum of E =0.5 V/Å, the pressure components remain nearly constant, which indicate the system is at equilibrium. A similar behavior can be noticed for the net dipole moment $\langle \tilde{Q}_z \rangle$ and the number of H-bonds $\langle HB \rangle$ in Figs. 5.10(b,c).

In order to show possible phase transitions induced by the applied field, we calculated the density variation of confined water (inside the channel) with respect to the applied field. In Fig. 5.12 we depict the variation of the

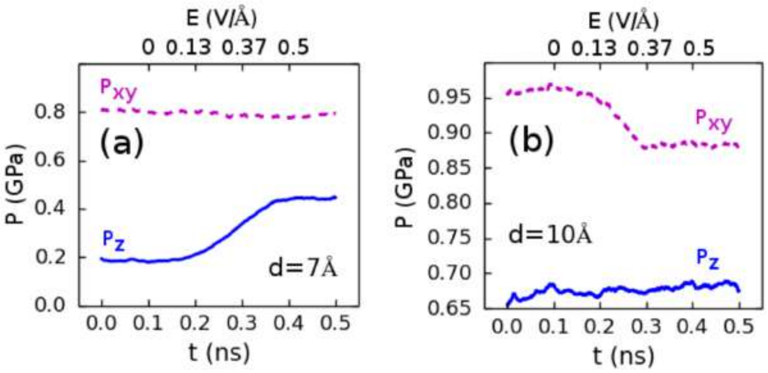

FIGURE 5.11. The variation of pressure of confined water with applied field for two channel heights with d=7Å and d=10Å (a). Two different components of pressure, i.e. p_z and p_{xy}, and total pressure inside the channel are shown separately in (b) and (c).

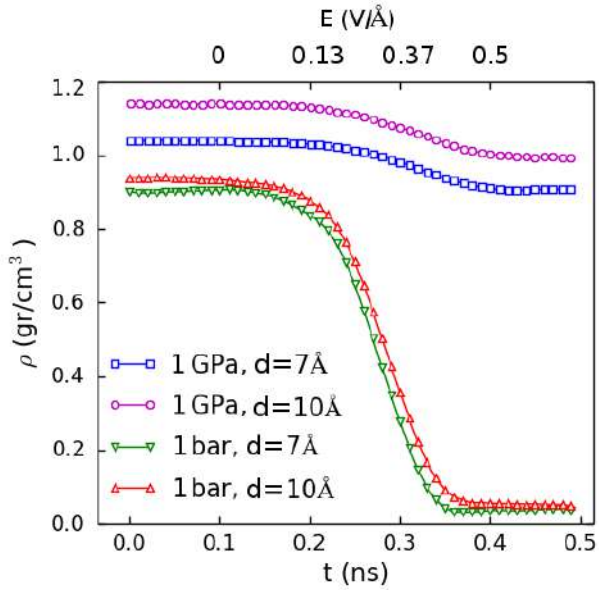

FIGURE 5.12. The variation of density with electric field for nanochannels with height d = 7Å and d = 10Å subjected to external pressure 1 bar and 1 GPa.

density with time for two different channels (d=7, 10 Å) and two different pressures (1 bar and 1 GPa). The results indicate evaporation of water when the pressure of the reservoir is kept at 1 bar. However when the external pressure is about 1 GPa, only a small decrease in density is observed, which indicates a transition from solid to liquid phase. The density decreases from

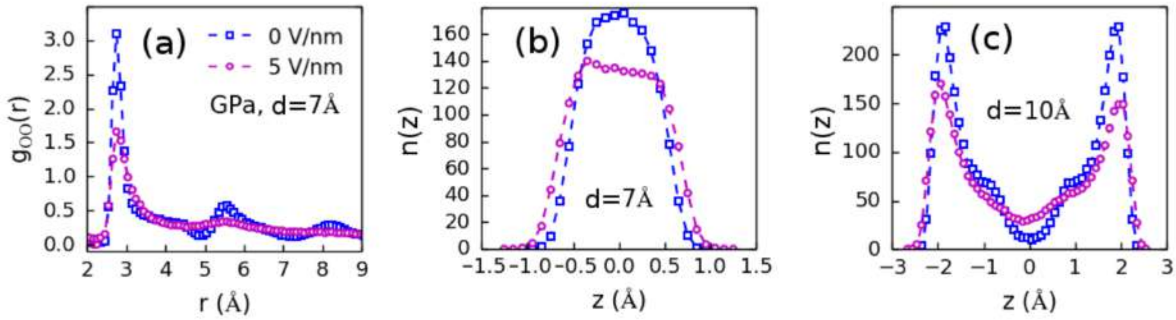

FIGURE 5.13. The radial distribution function for a system with d=7Å (a) and the corresponding density profiles along z-direction for d=7Å (b) and d=10Å (c). The results for two different electric fields are compared.

1.2 to about 0.9 gcm^{-3}. Our results for 1 bar is in agreement with those reported by Vaitheeswaran *et al.* [172]. In order to confirm the latter effect, the corresponding RDFs were calculated and are shown in Fig. 5.13(a) for d = 7Å subjected to GPa pressure and two different electric fields, i.e. 0 and 0.5 V/Å. The second peak in the RDF disappears when the electric field is 0.5 V/Å, which is an indication of a transition from the solid to the liquid phase. In Figs. 5.13(b,c) we depict the density profiles of O atoms along the z-direction for two systems with d=7Å and d=10Å, respectively. It is shown that for a smaller (larger) channel a single (bilayer) layer of water is formed. The larger the electric field, the smaller the number of water molecules which is consistent with Fig. 5.12. The evolution from one to two peaks with increasing d is similar to what we observed for model A, i.e. Fig 5.3.

5.5 Discussion and concluding remarks

In the past few years several studies [46, 52, 54, 161, 162], based on molecular dynamics simulations, disclosed different physical aspects of confined water between graphene layers. Here, we show that by changing the experimental setup, both the microscopic structure of confined water and the pressure inside the capillary will be different. The pressure, usually called van der Waals (vdW) pressure, is of the order of GPa for channels of height about

(6-10)Å [161]. Notice that in a real experimental situation the vdW forces between the two graphene sheets is attractive which minimize the contact region below the graphene sheet of a nanobubble. If water is trapped between the sheets, the bubble will shrink in size until the elastic energy of the graphene sheet and the adhesion between the substrate are balanced, i.e. a stable nanobubble is formed [182, 183]. This motivated us to introduce model A. If enough water molecules are trapped in this nanobubble a single layer of water molecules can be formed which is under the influence of large lateral and vertical pressures. For such a system the number of water molecules is constant, the temperature is kept nearly at zero Kelvin, and the height of the graphene nanochannel determines the water structure either to be flat or buckled. The structure of a monolayer water for $d \leq 8.5$ Å was found to be square-rhombic. We found that in a nanochannel with constant number of water molecules, the buckling height δ increases with the height of the channel, it reaches ~ 1.75 Å for a channel of $d \approx 8.5$Å. On the other hand, the three dimensional water density ρ decreases with increasing d.

Moreover, we studied the response of the confined monolayer of water to an out of plane electric field. By applying an external electric field the lateral pressure varies significantly and becomes larger than 1 GPa. The smaller d, the larger the lateral pressure. The net dipole moment of confined water increases linearly with electric field for weak fields and saturates at large field. For strong electric fields the square-rhombic structure is lost and the net dipole moment exhibits a hysteretic behavior. The minimum value of the electric field that is needed to deform the square-rhombic structure was found to be about 1.3 V/Å for $d = 8.5$ Å. Therefore we conclude that the confined monolayer of water in the first setup is very stable and resists against electric fields of about $< 1V/$Å. The very strong electric field applied on the confined water may ionize the water molecules in real situations and therefore it may appear that our conclusions in case of the first simulated setup has some limitations. However, although bulk water is ionized under such a strong electric field [34], in recent ab-initio calculations on confined water it was found that ionization of square-rhombic ice did not occur at such high electric fields and therefore we believe that our results are meaningful [53, 177, 178].

In the second part of this study, we reported the results for an open channel where water molecules can be exchanged with a reservoir via both sides at $T = 300\,\mathrm{K}$. Much weaker electric fields (as compared to the first setup) are required to induce deformation in the water structure. By controlling the pressure of the reservoir, we were able to control the pressure inside the channel. However, we found that the previously found square-rhombic structure now contains defects. The transition from solid to gas phase (albeit very few water molecules remain in the channel) due to the applied field, occurs only when ambient pressures are applied on the reservoir, i.e. 1 bar. However, keeping GPa pressure at the reservoir, we observed a transition from solid to liquid phase.

Our study demonstrated the sensitivity of the microscopic structure of confined single layer of water to different geometries of the simulation setup and external parameters.

Publication The results of this chapter were published in:

- Belisa R. H. de Aquino, H. Ghorbanfekr-Kalashami, M. Neek-Amal, and F. M. Peeters, *Electrostrictive behavior of confined water subjected to GPa pressure*, Phys. Rev. B **97**, 144111 (2018).

CHAPTER 6

IONIZED WATER CONFINED IN GRAPHENE NANOCHANNELS

When confined between graphene layers, water behaves differently from bulk and exhibits unusual properties such as fast water flow and ordering into a crystal. The hydrogen-bonded network is affected by the limited space and by the characteristics of the confining walls. The presence of extraordinary hydronium and hydroxide ions in narrow channels affects: i) water permeation through the channel, ii) they may interact with functional groups on the graphene oxide surface and on the edges, and iii) they change the thermochemistry of water which are fundamentally important to be understood especially when confined water is subjected to external electric field. Here we study the physical properties of water when confined between two graphene sheets and containing hydronium and hydroxide. We found that: i) there is a disruption in the solvation structure of the ions which is also affected by the layering structure of confined water, ii) hydronium and hydroxide occupy specific regions inside the nanochannel, and iii) the recombination rate of the ions in confined systems is slower than in bulk water and depends on the channel height and commensurability between the size of the molecules and the nanochannel height. Our work reveals distinctive properties of water confined in a nanocapillary in the presence of additional hydronium and hydroxide ions.

6.1 Introduction

The viscoelastic properties of nanoconfined water in graphene oxide nanocapillaries change significantly with the chemical nature of the confining walls, the dynamic state of the confined liquid, and the presence of various ions in water [184–187]. In experiments, atomically flat 2D-capillaries were fabricated with precise size exhibiting controled water flux determined by the channel size, e.g. an unexpectedly fast flow (up to 1 m/s) of water through flat nanochannels was reported [29]. This unexpected phenomena was found to be affected by the presence of ions as well as the presence of external electric field [185–190].

Moreover, several experimental and theoretical studies have been performed aiming to understand the solvation and mobility mechanisms of ions as well as the effect of an external electric field on the confined water [43, 187, 189–194]. An external electric field changes the physical properties of polar liquids due to the reorientation of their permanent dipoles: i) an in-plane electric field applied parallel to the channel polarizes water molecules which are confined between two graphene layers, resulting in distinct ferroelectricity and electrical hysteresis [54] and ii) a perpendicular field causes changes in the density and the phase of confined water [159, 195, 196]. Despite extensive theoretical studies on confined water [30, 32, 54, 156–162, 169] there are still many unsolved questions when confined water is subjected to an external electric field and in particular when the normal ionization state of water is altered.

In a recent study, the effects of ionization of water on water permeation through graphene oxide layers were studied [187]. It was found that the electric field induced ionization of water might be responsible for the blocking of the water flow. Previously, it was reported that water confined in nanochannels presents a layered structure and faster diffusion when compared to bulk exhibiting commensurability effects [162]. Using atomic force microscopy technique and by applying a low frequency electric field the permittivity of confined water under extreme confinement was determined to be ~2 [190]. However, how such effects influence the solvation, surface affinity and mobility of hydronium and hydroxide ions are still open questions.

In bulk, water ionization and the high density of hydrogen bonds that continuously form and break makes water a common solvent for several chemical and biological processes [197, 198]. The hydrogen bond network is responsible for several unique properties of water, such as density anomalies and high surface tension. Another consequence is the large mobility of hydronium (H_3O^+) and hydroxide (OH^-) ions which mediate acid-base chemical reactions and are of fundamental importance in complex enzymatic reactions [199]. In ordinary conditions, once formed, hydronium and hydroxide ions rapidly recombine, which is due to the interplay between vehicular diffusion and proton transfers between the ion and its neighboring water molecule, i.e. the Grotthus hopping mechanism [44]. All of these properties can be significantly influenced when water is confined between graphene sheets.

Here, by implementing molecular dynamics (MD) simulations, we investigate the structural and dynamical properties of the hydronium and hydroxide ions in confined water between two parallel graphene sheets. The extraordinary concentration of ions can be produced either by external electric field or be injected into the system resulting in a much larger concentration than in equilibrium. The later assumption can be realized around the electrodes and/or inside graphene oxide capillaries subjected to local strong electric fields [187]. The additional hydronium and hydroxide are extremely active and can react with various kinds of functional groups of graphene oxide membranes. The molecular mechanisms underlying the interaction of functionals of GO flakes and ions in the presence of external parameters are not understood yet. In this study we do not include the functional groups and only consider the effects of confinement on the solvation of the ions. We found that confinement affects both the structural and dynamical properties of the ions when they are diffusing in a 2D-space. The lack of a 3D-space and the water structure formed in 2D-space cause changes in the solvation of the confined ions when compared to the bulk system. Moreover, we show that confinement produces not only a layered structure for water but also for the ions, susceptible to changes depending on the channel height. Finally, we also report the effects of confinement and commensurability on the recombination process of the ions, leading to an ion lifetime that depends on the height of the

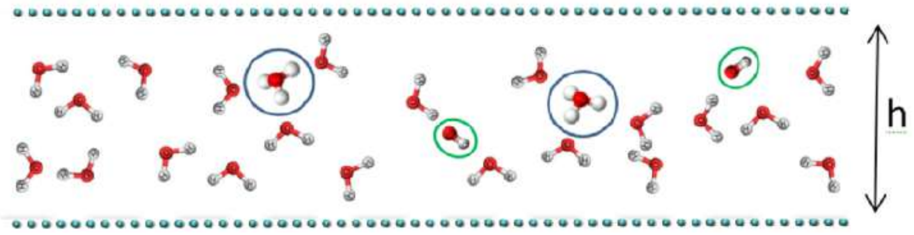

FIGURE 6.1. Side view of the setup of water confined between two graphene sheets containing two hydronium (blue circle) and hydroxide (green circle).

graphene nanochannel. Our results from classical MD simulations are in good agreement with Car-Parrinello (CP) MD simulations and shed light upon the unique properties of hydronium and hydroxide in graphene nanocapillaries.

6.2 Model and methods

We employed atomistic molecular dynamics (MD) simulations implemented in the LAMMPS package [83]. In order to model the ion recombination on water and the interaction between water and the carbon atoms on the graphene sheets, we used an improved ReaxFF force field [200, 201], which gives more accurate water density and properly describes the proton transfer mechanisms of hydronium (H_3O^+) and hydroxide (OH^-) [200]. A schematic picture of the simulation setup containing two pairs of ions in confined water between two graphene sheets is shown in Fig. 6.1.

In order to serve as a reference to our results regarding water confined in a graphene nanochannel, we initially considered bulk water. The simulation box contained 6845 water molecules with periodic boundary conditions. A 200 ps simulation was performed using the NPT ensemble with the Nosé-Hoover thermo/barostat and a time-step of 0.25 fs to equilibrate the system at $T = 298\,\mathrm{K}$ and $p = 1\,\mathrm{atm}$. In order to produce ions, unless specified otherwise, water molecules were randomly selected and replaced either by H_3O^+ or OH^- according to the water ionization equation: $2\,H_2O \longrightarrow OH^- + H_3O^+$. The number of substitutions were chosen to correspond to an initial ion concentration of 1 %. Such high concentration is necessary for the study of statistical and dynamical properties of the ions to be computationally feasible and should give reliable qualitative results. Production run was performed during 200 ps.

For the confined system, we considered two parallel graphene sheets separated by h, with area $A = 106,5\,\mathrm{nm}^2$ and with periodic boundary conditions in the x-y plane (parallel to the graphene sheets). To simulate the correct density for water, the number of water molecules was chosen in order to have bulk water density, i.e. $\rho \sim 1\,\mathrm{g/cm}^3$ under a pressure of 1 atm and a temperature of 298 K. First, a 200 ps simulation only with water molecules was performed using the NVT ensemble with a Nosé-Hoover thermostat and a time-step of 0.25 fs. Then, water molecules were replaced by H_3O^+ and OH^- following the procedure described above. Next, a 200 ps production run was performed. Different channel heights h in the range $[6.5, 11]$ Å and 30 simulations with different initial positions for the ions were performed in order to obtain good statistics. A proton transfer occurs when the closest oxygen (O) atom to an hydrogen (H) atom changes within two consecultive time steps, i.e., an H atom hops from one molecule to the other. Intermediate proton transfer processes are defined by a proton transfer between an ion and a H_2O molecule. In this sense, a recombination is reached when the proton transfer process occurs between H_3O^+ and OH^- ions, i.e., $H_3O^+ + OH^- \longrightarrow 2\,H_2O$.

We also conducted additional *ab initio* molecular dynamics simulations (AIMD) by using the Car-Parrinello (CP) method [58] implemented in the CPMD package [202]. A time-step of 4 a.u. (0.097 fs), fictitious electron mass of 400 a.u. (0.000548 a.m.u.), Perdew- Burke-Ernzerhof (PBE) functionals, and a plane wave energy cutoff of 50 Ry were chosen [191]. Furthermore, van der Waals correction according to Grimme [203] and norm-conserving pseudopotential to describe the core region of carbon and oxygen atoms were used. AIMD simulations employing the same set of parameters at room temperature proved to guarantee the adiabaticity condition and good agreement (i.e. radial distribution function) with previous studies on bulk water [204, 205] and properly reproduces the proton transfer for two neighboring ions [43].

CPMD simulations were carried out up to 5 ps starting from the initial configuration obtained from the classical MD. Due to computational limitations, we considered a relatively small system containing two layers of graphene (360 carbon atoms) and dimensions of 22 Å × 21 Å with 60 water molecules (540 atoms in total) that yielded an interlayer distance of 7 Å. A vacuum distance of 1.5 Å along the nanochannel height was set and ions were added following the procedure outlined above for the confined and the bulk (180 water molecules) systems. The results were compared with those of classical MD simulations performed with the same choices of system size and time-step.

Our MD simulations for hydronium and hydroxide ions in water confined in a graphene nanochannel led to different structural and dynamical properties for both OH^- and H_3O^+. The confinement affected not only the recombination of the ions, but also their solvation structures and density profiles. These effects are discussed below.

6.3 Effects of the graphene nanochannel height on the solvation of the ions

In order to investigate the effects of confinement on the solvation of the ions, we considered a single ion (either H_3O^+ or OH^-) in confined and bulk water.

6.3.1 Radial distribution function

The differences between confined and bulk water can be noticed from the O^*-O radial distribution functions (RDFs) shown in Fig. 6.2 for different channel heights, h, and bulk where O^* (O) is the oxygen of the ion (water molecule). Our results for bulk are in agreement with those reported in Ref. [200]. The increase in the first peak height of the H_3O^+ (Fig. 6.2(a)) and OH^- (Fig. 6.2(b)) RDFs for stronger confinements indicates a stronger interaction between the ions and their first solvation shell. The shoulders at ~ 3.2 (~ 2.8) in the H_3O^+ (OH^-) RDF correspond to the interaction with the HB donor or the second nearest water molecules, depending on the confinement. The nearly absence of a peak at ~ 4 Å in the H_3O^+ RDF for $h = 6.5$ Å as well as the inward shift of the second peak in the OH^- RDF for $h = 8.5$ Å indicates that the influence of the nanochannel size on the structural properties of the ions is not limited

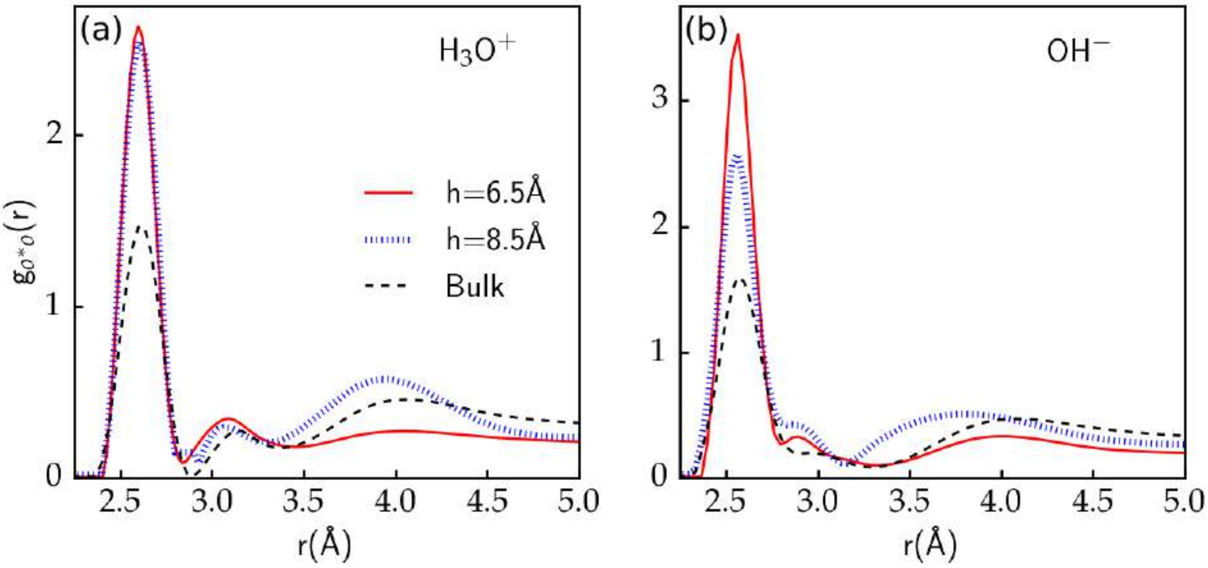

FIGURE 6.2. Radial distribution functions for O*-O of confined and bulk water, where O* corresponds to the oxygen of the ion: (a) H_3O^+ (b) OH^-.

to the nearest water molecules and is rather long range. It also implies that commensurability effects plays more important role at long range.

6.3.2 Spatial distribution function

The spatial distribution functions (SDFs) for the ions also depict the effects of confinement caused by the graphene nanochannel. The SDFs for H_3O^+ and OH^- are shown in Figs. 6.3(a-c) and Figs. 6.3(d-f), respectively, and exhibit regions of nonzero probability occupied by the O atoms of the water molecules around the ion at a distance $r < 3.25$ Å for the graphene nanochannel. The first solvation shell of H_3O^+ is determined by the three clouds closer to the hydrophilic (H^*) sites of the ion, which correspond to the three water molecules donating a HB to H_3O^+ and are due to the three-coordination nature of H_3O^+. Those clouds are present for all the investigated channel heights and are in agreement with the first solvation shell for bulk water [200]. However, the effects of the graphene capillary size are significant beyond the first solvation shell. This is evidenced by the differences in the other clouds shown in Figs. 6.3(a-c) for different confinements. For $h = 6.5$ Å(Fig. 6.3(a)), *three* other

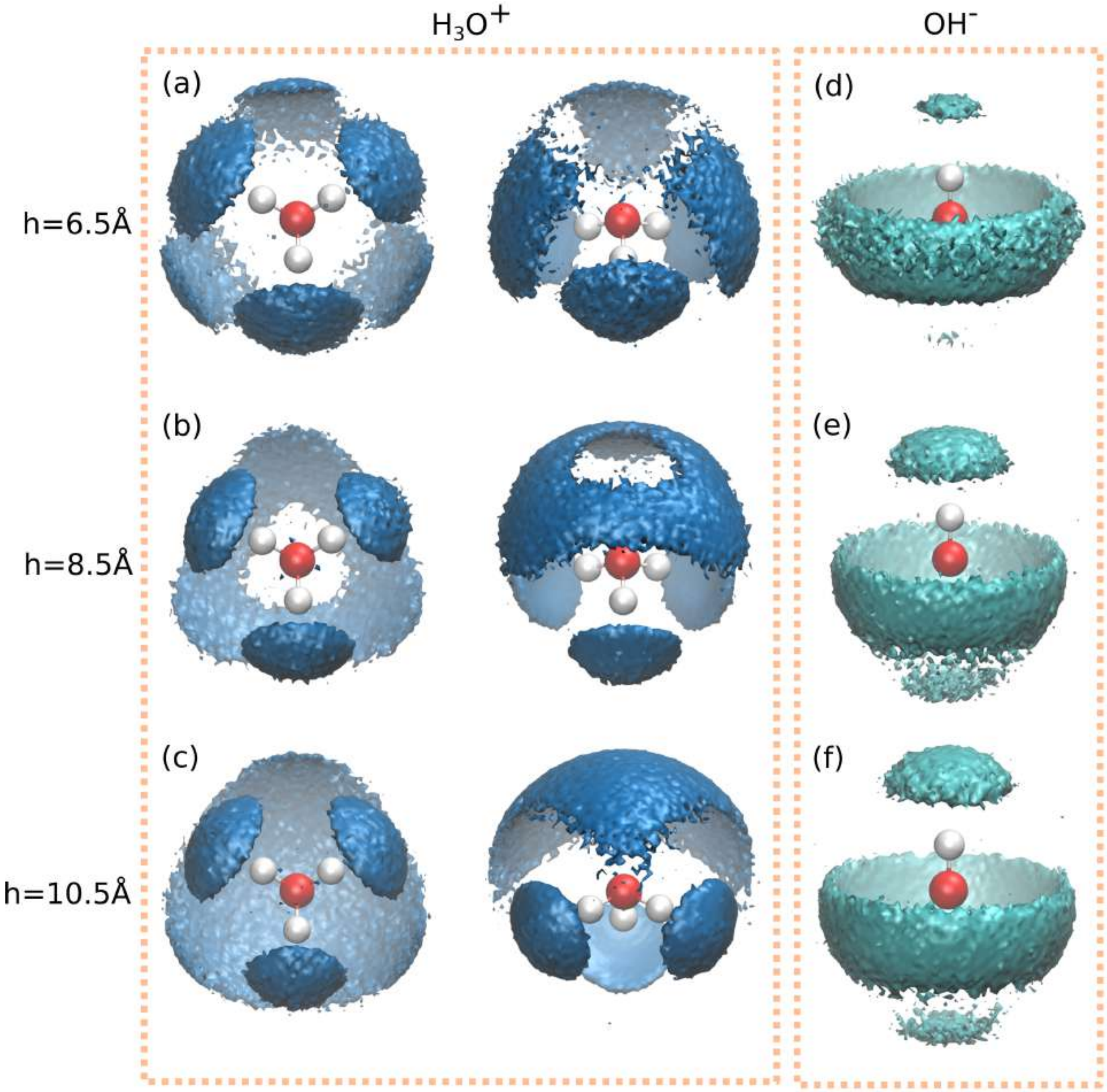

FIGURE 6.3. Spatial distribution functions (SDFs) with $r < 3.25$ Å of the water molecules (blue) around H_3O^+ [O^* (H^*) in red (white)] and (c) $h = 6.5$ Å, (d) $h = 8.5$ Å and (e) $h = 10.5$ Å (two different view angles are shown in the left and right-hand sides). The corresponding SDFs of water molecules (light blue) around OH^- are shown in (f-h).

clouds are symmetrically displaced with respect to the regions occupied by the first solvation shell, corresponding to the second nearest water molecules. The structure formed by the clouds indicates that the ion is surrounded by a nearly flat water structure, which is in agreement with the theoretically predicted and experimentally observed water structure for such small channel heights [52, 55, 159, 162, 196]. For $h = 8.5\,\text{Å}$ (Fig. 6.3(b)), a single *hollow* cloud surrounds the hydrophobic (O^*) site of the ion. This is due to the competition between confinement and propensity of H_3O^+ to accept an HB from a water molecule. As h is further increased, the outer cloud becomes similar to the one observed for bulk [200], i.e., a wide and completely *full* cloud as shown in Fig. 6.3(c) for $h = 10.5\,\text{Å}$, which means the effects of confinement on the solvation structure of H_3O^+ are more significant for $h < 10\text{Å}$.

The solvation structure of OH^- is less affected by the graphene nanochannel height as compared to H_3O^+. This is evidenced by the SDFs for OH^- and $r < 3.25\,\text{Å}$ shown in Figs. 6.3(d-f) for $h = 6.5\,\text{Å}$, $h = 8.5\,\text{Å}$ and $h = 10.5\,\text{Å}$, respectively. The SDFs for $h = 8.5\,\text{Å}$ and $h = 10.5\,\text{Å}$ almost coincide and are similar to the SDF for bulk reported in Ref. [200]. In this case, a central cloud surrounding the hydrophilic site of the ion (O^*) is observed together with two smaller clouds aligned to the O^*-H bond. The central and bottom cloud correspond to the HB donors, while the upper cloud, closer to the hydrophobic site (H^*) corresponds to the HB acceptor. The central cloud appears slightly below the plane containing the O^* atom, due to the tetrahedral structure formed by the ion and the water molecules. The effects of the graphene nanocapillary become evident, however, for $h = 6.5\,\text{Å}$, with the *alignment* of the central cloud to the O^* atom, due to the obtained flat water structure. Besides, the smaller upper and bottom clouds with respect to larger channel heights, indicates the preference of the OH^- ion to be aligned *perpendicularly* to the water monolayer. The nearly *absence* of a bottom cloud in Fig. 6.3(d) evidences that, even when the O^*-H bond is in plane with respect to the water monolayer, the occupancy of this site by an HB donor is unlikely for narrow graphene nanocapillaries.

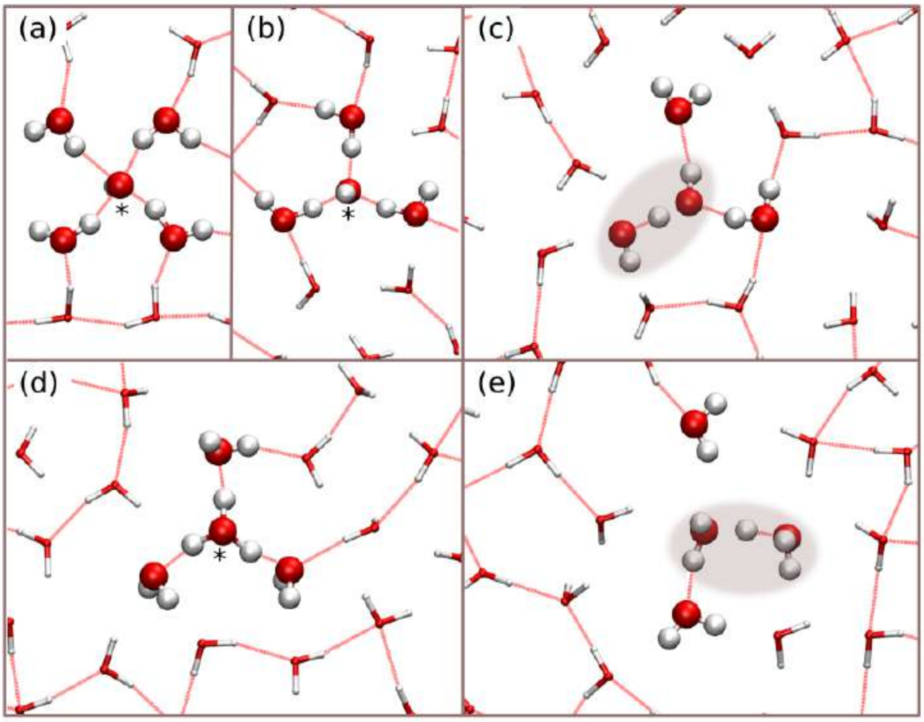

FIGURE 6.4. Top view of the hydration structures of the ions inside a graphene nanochannel with $h = 6.5\,\text{Å}$. The OH^- ion (a) with four, (b) with three HB water donors and (c) forming a Zundel-like structure shown in the highlighted region. The H_3O^+ ion (d) with three HB water acceptors and (d) forming a Zundel structure in the highlighted region. The O^* atom is indicated by an asterisk (*), hydrogen bonds are indicated by red lines, oxygen (hydrogen) by red (white) color.

6.4 Hydration of the ions in a narrow graphene nanochannel

Fig. 6.4 shows the top view of different hydration structures formed around the ions and the nearest water molecules for a graphene channel height of $h = 6.5\,\text{Å}$. For the OH^- ion, Figs. 6.4(a-b) show the ion with the O^*-H bond aligned perpendicularly to the water lattice, with the O^* atom belonging to the water plane. On the other hand, (c) shows the OH^- ion with the O^*-H bond in the water plane. The configuration in (a) has a hypercoordinated structure with four water molecules donating HBs to OH^-, while (b) shows the $OH^-(\cdot\cdot H_2O)_3$ ion formed by three water molecules donating a HB to the OH^-

ion. The proton transfer mechanism can be glanced in the highlighted region of Fig. 6.4(c), where a Zundel-like intermediate $[OH\cdot\cdot H\cdot\cdot OH]^-$ appear, with an undercoordinated OH^-. The hydration structures of the ions and lately the hypercoordinate state of OH^-, i.e., $OH^-(\cdot\cdot H_2O)_4$, has been subject to several previous studies on bulk water using different techniques [193, 194, 206–208]. However, the configurations depicted in Figs. 6.4(a-c) show the *absence* of a HB donor parallel to the O^*-H^* bond, corresponding to the almost inexistent bottom cloud in Fig. 6.3(d), which is a consequence of the strong confinement inside the graphene nanochannel.

Figure 6.4(d) shows that the water structure formed inside the narrow graphene channel also affects the hydration structure of H_3O^+, which donates HBs to three water molecules, while other *three* water molecules are displaced between the HB acceptors, in agreement with the SDF shown in Fig. 6.3(a) and clearly differing from bulk water behavior, where a water molecule is expected to approach the O^* atom [200]. Besides, Fig. 6.4(e), shows an undercoordinated structure for H_3O^+ with one *lone* O^*-H bond oriented *perpendicular* to the water monolayer, which does not happen in bulk water. Such configuration and relative position of the H_3O^+ ion with respect to the water layer elucidate the reason for the larger clouds shown in Fig. 6.3(a). The highlighted region in Fig. 6.4(e) shows the Zundel-like structure intermediate $[H_2O\cdot\cdot H\cdot\cdot H_2O]^+$ of the proton transfer process, which follows the Eigen-Zundel-Eigen mechanism.

6.5 Effects of commensurability on the density profile of the ions

While in bulk the water molecules are uniformly distributed, when confined in a graphene nanocapillary, the commensurability between the channel height and the size of the water molecule governs layering structure of confined water which depends on the channel height [162]. Likewise, commensurability effects also determine the distribution of the ions inside the graphene nanochannel. The different regions occupied by the ions are reflected in the density profile of the oxygens in the direction perpendicular to the graphene

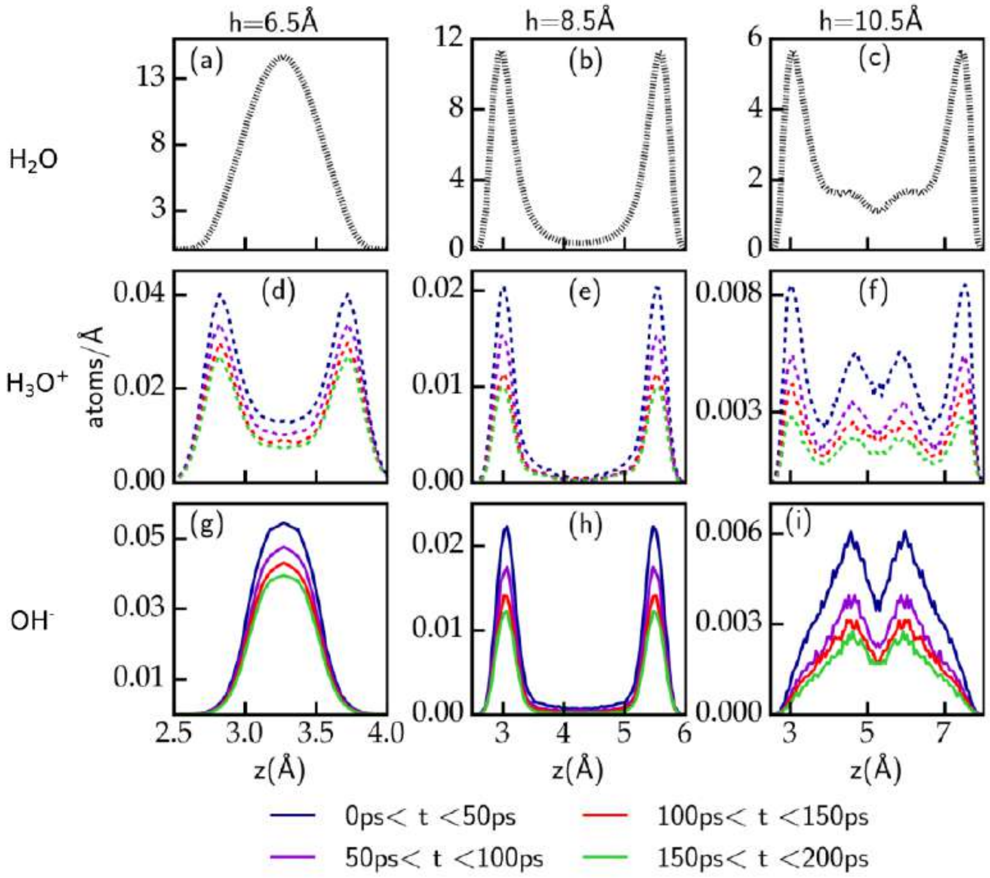

FIGURE 6.5. Density profile of oxygens of different molecules/ions for different h values. The different curves are for different time intervals showing a decrease in H_3O^+ and OH^- density with time because of recombination.

sheets (z-axis). Figures 6.5(a-i) show the density profile of the oxygens for water, H_3O^+ and OH^- and Figs. 6.6(a-f) show side views of the hydration structure of the ions for different channel heights. The different colors in Figs. 6.5(a-i) represent different simulation time intervals. Smaller peaks in the density profiles with time reflects the decay in the ion concentration due to recombination, which will be further discussed.

6.5.1 Water

The density profiles of water are shown in Figs. 6.6(a-c) for different channel heights. For $h = 6.5$ Å, only one central peak exists which is typical for a flat

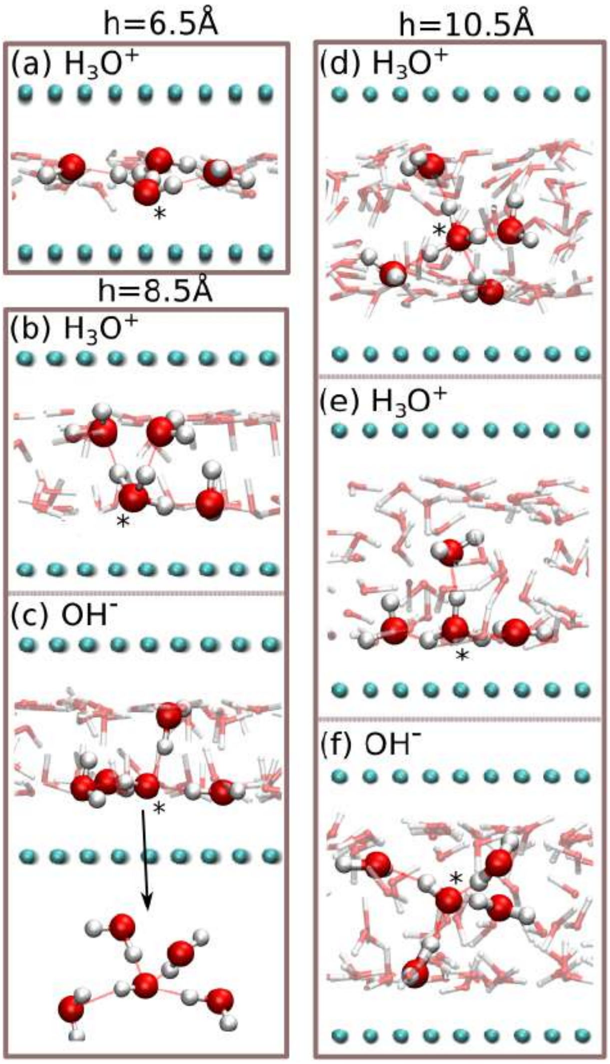

FIGURE 6.6. Side view of possible hydration structures for an ion (indicated by an asterisk (*)) for the corresponding h values are shown in (j-o). In panel (l) a different view angle is shown in the bottom.

water monolayer. For larger channel heights, however, two density peaks at the edges are shown, with a bilayer profile shown for $h = 8.5$ Å and the density in the internal region increases as h increases, as seen for $h = 10.5$ Å. These are typical behaviors of water confined in graphene nanochannels [162].

6.5.2 The hydronium ion

The density profile of H_3O^+ for h = 6.5 Å (Fig. 6.5(d)) presents *two* peaks symmetrically located around the center of the channel and a *nonzero* density in the internal region. The former are due to the tetrahedral structure of the H_3O^+ ion together with its three-coordinate nature that leads to a slight shift of the O^* atom outward with respect to the water plane when hydrated as shown in Fig. 6.4(d). This shift in the H_3O^+ position is shown in Fig. 6.6(a). The nonzero density close to the center of the graphene channel is due to the hydration structure shown in Fig. 6.4(e). As for h = 8.5 Å (Fig. 6.5(e)) the H_3O^+ ions form a *bilayer* structure having intra and interlayer HBs with neighboring water molecules as shown in Fig. 6.6(b). In the case of h = 10.5 Å (Fig. 6.5(f)), the commensurability between the channel and H_3O^+ sizes enables the occupancy of internal regions and two smaller *inner* peaks are shown, correponding to hydration structures as the one shown in Fig. 6.6(d). However, there is still a prevalence of H_3O^+ occupancy in the edges indicating that the structure shown in Fig. 6.6(d) appears mainly when mediating proton transfer processes between the edges, with the structure shown in Fig. 6.6(e) having a longer lifetime.

6.5.3 The hydroxide ion

The hydroxide ion behaves as water molecules for both the monolayer (h = 6.5 Å) and bilayer cases (h = 6.5 Å). For instance for a channel of height h = 6.5 Å, the O^* atom tend to occupy the central region where only *one* central peak appears in the density profile of OH^- (Fig. 6.5(g)). For h = 8.5 Å the OH^- ions form two water layers corresponding to the *two* density peaks in Fig. 6.5(h). In the latter case the ion is hydrated by forming intra and interlayer HBs as shown at the top of Fig. 6.6(c) (at the bottom, a different angle of the structure formed by OH^- and the closest water molecules is shown). However, for larger channel, e.g. h = 10.5 Å the hydroxide ions are mostly in the interior region of the water slab (see Fig. 6.5(i)) having two *inner* peaks coinciding with the inner peaks found for H_3O^+ (see Fig. 6.5(f)). Figure 6.6(f) shows that the OH^- ions form HBs with edge water molecules as well as with inner molecules and others slightly shifted inward with respect to the edges.

6.6 Affinity of the ions into the surface

The propensity of H_3O^+ and OH^- to remain at the water surface in a water slab or water cluster has been subject of ongoing debate. Some studies report an acidic surface with a superficial enhancement of hydrated protons while others report the propensity of OH^- ions to remain at the surface leading to a superficial basic pH. [209–215] In the case of ions in water confined in a graphene nanochannel, our results show that the surface affinity of the ions are determined by commensurability effects. For example, in a graphene nanocapillary with $h = 6.5\,\text{Å}$, we found that the H_3O^+ ions remain closer to the graphene sheets while the OH^- ions are located within the water plane leading to a basic water plane and acidic edges. However, for $h = 8.5\,\text{Å}$, both ions form bilayer water leading to a neutral surface. For larger channel heights, e.g. $h = 10.5\,\text{Å}$, an acidic surface is favored where OH^- ions are absent at the edges. The different curves shown Figs. 6.5(d-i) reveal the latter effects while the ion density decreases with time (due to ion recombination) and the density profile remains unaltered.

6.7 Ion recombination inside the graphene nanochannel

Finally an induced water ionization by, e.g. an electric field [187] causes an initial higher concentration of the ions which decreases with time due to the recombination processes. In our simulation results, this behavior is confirmed by the decrease in the density in Figs. 6.5(g-o). The variation of the ion concentration with time is shown in Fig. 6.7(a). For a channel height of $h = 6.5\,\text{Å}$ the ion concentration follows an exponential decay, i.e., $f(t) = c_1 e^{-t/\tau_1} + c_2 e^{-t\tau_2}$. Here, τ_1 is the time constant corresponding to the first picoseconds of the simulation, when faster recombination processes occur due to the higher ion concentration, while the rest (and most) of the

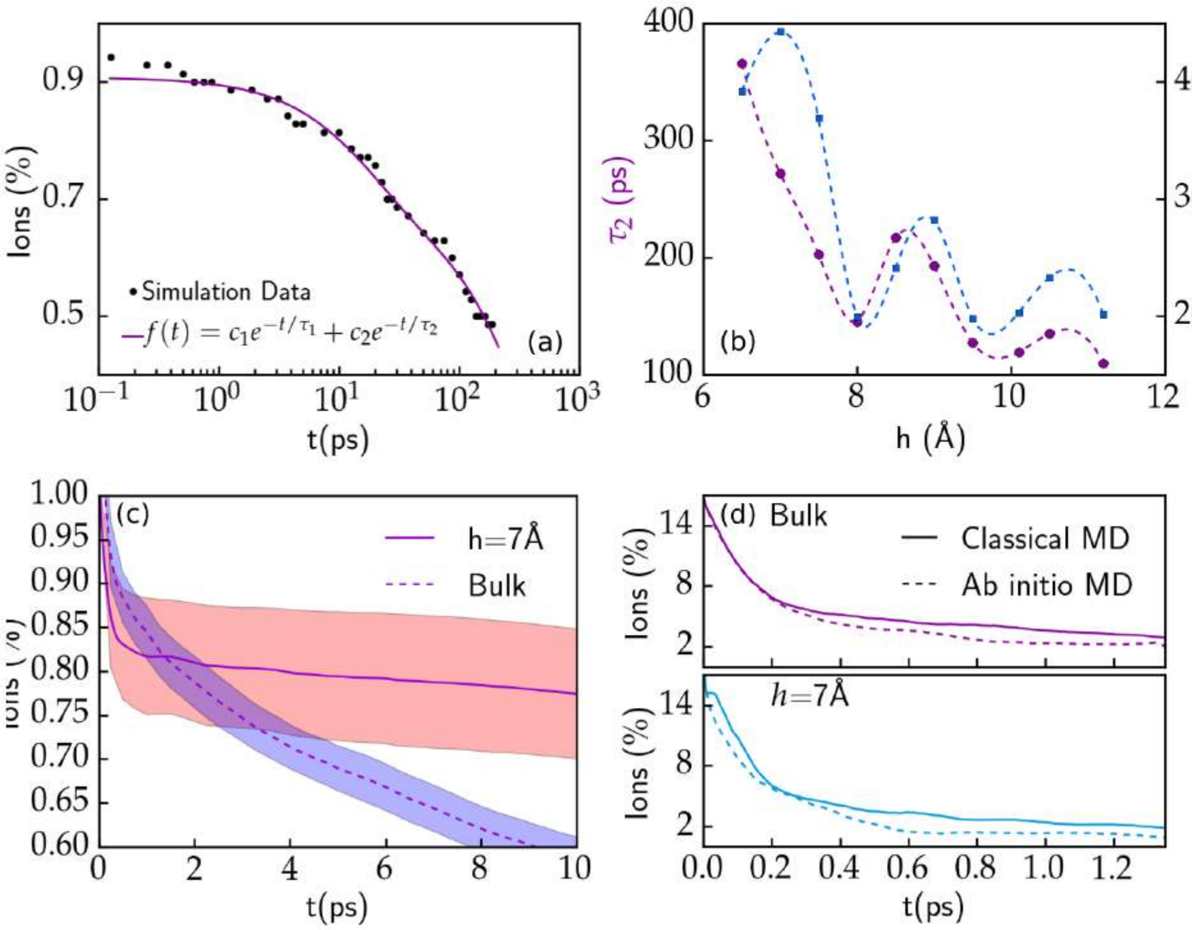

FIGURE 6.7. (a) The variation of the concentration of the ions with time for $h = 6.5$ Å. The plain, dotted and dashed curves are exponential fits indicated in the figure. (b) The variation of the time constants τ_1 and τ_2 with the channel height h. The dashed curve is a spline interpolation of the data. The variation of the concentration of ions with time for bulk and confined water ($h = 7$ Å) (c) with an initial ion concentration of 1 % (filled regions correspond to standard deviations) and (d) with an initial ion concentration of $\sim 17\%$, for classical and CPMD simulations.

simulation time is dominated by τ_2, which is related to the ion lifetime. Such behavior is observed for both bulk and confined system, with the time constants depending on the graphene channel height. Figure 6.7(b) shows that both time constants tend to decrease with increasing h, i.e., in narrow graphene nanocapillaries, the ion lifetime is increased. However, the presence of local maxima in Fig. 6.7(b) represents the effects of commensurability between the channel height and the size of the ions. The local maxima coincide with the channel heights that allow a well defined layered structure for the ions (see Fig. 6.5). Similar effects of commensurability have been previously reported for the viscosity of confined water [162].

The 2D-diffusive motion of ions inside the confinement causes different physical properties as compared to bulk. Our findings are in agreement with previous reports regarding proton transfer in layered 2D water, where the solvation shell structure and H-bond reorganization slow down the rate of net proton transfer events as compared to bulk water [216]. Figure 6.7(c) shows the variation of the ion concentration with time for $h = 7\,\text{Å}$ and bulk. We found $\tau_1 = 11\,\text{ps}$ and $\tau_2 = 47\,\text{ps}$ for bulk water, i.e., around half the values obtained for $h = 11.2\,\text{Å}$ (see Fig. 6.7(b)). It is expected, however, that in one-dimensional water chains such as water confined in carbon nanotubes the behavior would be the opposite, i.e., faster net proton transfer rate with respect to bulk and consequently smaller ion lifetime due to a different proton transfer mechanism [217].

The decay of the ion concentration with time in our classical MD simulations were compared to those of CPMD simulations. The variation of the ion concentration with time for both classical MD and CPMD simulations are shown in Fig. 6.7(d) for bulk and confined system ($h = 7\,\text{Å}$). Here, an initial ion concentration of 17% was used. Such high initial concentration, as well as smaller system size are needed due to computational limitations. We found that although very distinct methods, the decaying behavior of the ion concentration of both CPMD and classical MD results are similar, with the ion lifetime slightly larger for classical MD simulations.

6.8 Conclusions and discussions

Controlling water flow through porous membranes and consequently designing controllable nanochannels are one of the major challenges in nanoengineering of advanced nanostructures. The combined modelling and experimental efforts in achieving these goals by using several external parameters such as electric field and temperature will bring new fundamental understanding of molecular transport at the nanoscale. Moreover, using materials other than graphene (e.g. hexagonal boron nitride (h-BN) and MoS_2), allows expanding the functionality of nanochannels, producing novel nanochannels, and provides a deeper understanding of the nanoscale transport physics. In the long term, this may have applications in water desalination and gas separation technology. The problems raised in this paper is of interest for the graphene community because the presence of ions, here the presence of extraordinary concentration of hydronium and hydroxide ions changes: i) the permeability of water through nanochannels, ii) thermochemistry of the confined water, iii) dynamical properties of confined water such as diffusion constant and viscosity, and iv) hydration shells and dehydration behavior of various ions. For instance, the different solvation structure and recombination time of the ions in confined systems will change the ionic properties of the confined water which ultimately influence water permeability and even reduces graphene oxide. Moreover, the longer lifetime of ions in confined system as compared to bulk facilitates the interaction of hydronium and hydroxide with other atoms in the system and functionals of graphene oxide.

In summary, the commensurability between the graphene nanochannel size and the size of the ions and water molecules determine the structural and dynamical properties of hydronium and hydroxide which were found to be significantly different from those for bulk water [200]. The ions rearrange depending on the channel height and their solvation and their distribution strongly depend on the layering structure of the water formed in the confined region. For strong confinements, the limited space restricts the water molecules to receive (donate) an hydrogen bond from (to) the OH^- (H_3O^+) ion. The surface affinity of the ions depends on the graphene nanocapillary size, i.e., although H_3O^+ ions mostly stay closer to the graphene sheets, the OH^-

ions may also appear either in the inner or in the outer regions depending on the channel height. The mobility of the ions is also affected by the capillary size. The ion lifetime is enhanced in confined water when compared to bulk and it can be locally increased due to commensurability effects. The latter will affect the thermochemistry of confined water. Our findings contribute to a better understanding of the interplay between the structural and dynamical properties of hydronium and hydroxide and their influence on the water flow through graphene nanocapillaries. Moreover, it is also relevant for biological proton channel systems and acid-base neutralization processes in confined regions.

The results of this chapter are under review at Physical Review B.

CHAPTER 7

SUMMARY AND OUTLOOK

7.1 Summary

In this thesis I employed molecular dynamics simulations to study systems arisen from different applications of carbon-based materials. The simulations were implemented by using LAMMPS, a cutting edge software able to simulate solid-state materials, soft matter, coarse-grained and mesoscopic systems. This choice enabled simulations of systems with thousands of atoms. The force fields were chosen in order to properly describe the main features of the investigated systems.

The first topic of interest was carbon nanotubes/nanoparticles hybrid devices. I investigated carbon nanotubes coated with Ag nanoparticles and linked the properties of nanoparticles to those of carbon nanotubes. In Chapter 3, I considered a system where Ag atoms were adsorbed on CNTs of different chiralities. The different CNT structures led to different migration and coalescence mechanisms for the nanoparticles. The nanoparticle diffusion also depended on the CNT chirality, where zigzag carbon nanotubes appeared as the best candidates for mass transport while armchair carbon nanotubes would be the best choice to be used as a support. The size of nanoparticles where determined by the propensity to migrate, with larger nanoparticles found for zigzag carbon nanotubes and for higher temperatures, which was also employed as a mechanism for controlling the nanoparticle size. Finally, the increase in the concentration of defects on the carbon nanotube surface led to a drastically drecrease in the diffusion of nanoparticles and consequently smaller size of nanoparticles, as the defects acted as anchoring sites.

Subsequently, the resonating properties of decorated carbon nanotubes were linked to their mass sensing ability. In Chapter 4, a carbon nanotube is decorated with a charged metallic nanoparticle subjected to the effects of an electric field. The field is applied perpendicularly to the carbon nanotube axis and the deflections of the tube are related to the magnitude of the field. Two different NP shapes (dot- and ring-shaped) as well as three different metallic species (Ag, Pd and Na) were investigated. Carbon nanotubes of three possible chiralities (armchair, zigzag, chiral) with a diameter of ~ 0.4 nm were considered. The nanotube deflections were linked to its chirality and nanoparticle charge, while the mass, metallic species and shape of nanoparticless had little to no effect. The airmchair carbon nanotube had the largest deflections, while the zigzag carbon nanotube was the less affected. Vibrational motions due to the assembly of nanoparticles on carbon nanotubes were observed to be not only in the direction of the electric field, but to have a two-dimensional (2D) nature. The vibrational pattern proved to be dependent on the applied electric field and the properties of carbon nanotubes and nanoparticles, including mass, shape and metallic species. The 2D vibrations of a charged pristine carbon nanotube presented deflections with one order of magnitude smaller as compared to decorated carbon nanotubes. The frequencies of vibrations of the decorated carbon nanotubes were also linked to the properties of the system, namely nanotube length, NP mass and applied electric field. The deflections, vibrations and resonance frequencies were fitted against analytical expressions, exhibiting good agreement. The findings presented here evidences the possibility to apply 2D-vibrations of carbon nanotube nanoresonators to mass detection.

The second topic of this thesis was focused on confined water in nanocapillaries. Chapter 5 refers to the effects on structural properties of monolayer water due to changes in the graphene nanochannel height, perpendicularly applied electric field and lateral pressure. First, a graphene nanochannel containing a fixed number of water molecules subjected to ~ 0.15 GPa pressure was investigated. By equilibrating the system until it reached a temperature of 1 K, the monolayer water exhibited a square-rhombic structure, which was flat (buckled) for channel heights smaller (larger) than 6.6 Å. By applying an electric field perpendicular to the graphene sheets, the square-rhombic structure was destroyed as the water molecules flipped towards the electric field and the water net dipole moment presented a hysteretic behavior. The structural changes induced by the applied field were accompanied by an increase in the lateral pressure up to GPa order pressures. Subsequently, an open graphene nanochannel immersed in a water reservoir at room temperature was considered. A lateral pressure was applied to the reservoirs, where 1 GPa and 1 bar pressures were considered. By applying a perpendicular electric field, the water molecules initially inside the nanochannel were nearly completely expelled to the reservoirs in the case of 1 bar pressure, while for 1 GPa pressure the decrease in the water density was minimal. Increasing the electric field led to a significantly faster increase in the net dipole moment as compared to the water monolayer in the previous system. The variations of the pressure with electric field showed a dependence on the confinement, where variations in the transverse (lateral) pressure were more significant for strong (weak) confinements.

Finally, the behavior of ionized water in graphene nanochannels was investigated in Chapter 6. We first considered water confined in a graphene nanochannel and, after equilibrating the system at room temperature, water molecules were randomly replaced by an equal concentration of hydronium and hydroxide ions. The effects of confinement on the structural properties of the ions could be clearly observed by the radial and spatial distribution of nearest water molecules. The hydroxide ion exhibited both the hypercoordinated structure and the first solvation shell composed of three water molecules, while the former was the standard structure found for hydronium. Proton transfer processes exhibited the Eigen-Zundel-Eigen mechanism for both ions. The distribution of the ions in the nanochannel depended on the channel height: a nanochannel containing a bilayer water exhibited nearly neutral edges, while the most common distribution exhibited hydronium ions closer to the edges while hydroxide ions remained in the slab interior. The ion recombination, which occurred due to the combination of vehicular diffusion and proton transfer mechanisms, exhibited an exponential decay with time, where the ion lifetime was larger for confined than for bulk water. However, local increase in the ion lifetime was observed depending on the channel height, evidencing commensurability effects.

7.2 Outlook

The study of decorated carbon nanotubes in Chapters 3 and 4 was conducted by considering carbon nanotubes and attached metallic nanoparticles. The complexity of the system can be enhanced by considering other kinds of particles/molecules adsorbed on carbon nanotubes and/or the adsorption of nanoparticles on, e.g., amyloid fibrils, which helical configuration have similarities with the structure of carbon nanotubes. The addition of solvent in the system can also enable the study of the effects of pH on the adsorbing sites. Moreover, accounting for charge transfer between the substrate and the nanoparticles allow for the investigation of this effect on the metallic adsorption and sensing properties. A more advanced study of such devices is fundamental to optimize hybrid materials aiming the fabrication of metallic nanowires by using carbon nanotubes/amyloid substrates or to explore the mass transport potential of such materials. The detailed description of the nanoresonating properties of hybrid devices can evidence the remarkable sensibility of nanoresonators and potential applications, where nanoparticle sensing is essential to detect, e.g., functional compounds or biomarkers.

In Chapters 5 and 6, the investigation of water inside graphene nanocapillaries was focused on the effects of confinement, pressure and electric field on the water structure and/or water ions. The results can be compared to recent experiments on graphene nanobubbles and nanocapillaries and bring new insights on the structural and dynamical properties of confined water, such as 2D water structure and fast water flow in nanochannels. The study can be expanded to consider the presence of defects and functionalized sites on the graphene sheets in order to investigate water/ion permeation and flow through the graphene sheets. The effects of confinement on larger ions that are commonly present on water can also be studied in order to investigate water/ion obstruction in nanochannels, which are useful for designing new filtration devices.

BIBLIOGRAPHY

[1] S. K. Tiwari, V. Kumar, A. Huczko, R. Oraon, A. De Adhikari, and G. C. Nayak, “Magical allotropes of carbon: Prospects and applications,” *Crit. Rev. Solid State Mater. Sci.*, vol. 41, p. 257, 2016.

[2] A. Dato, Z. Lee, K.-J. Jeon, R. Erni, V. Radmilovic, T. J. Richardson, and M. Frenklach, “Clean and highly ordered graphene synthesized in the gas phase,” *Chem. Commun.*, vol. 40, p. 6095, 2009.

[3] S. K. Tiwari, V. Kumar, A. Huczko, R. Oraon, A. De Adhikari, and G. C. Nayak, “The rise of graphene,” *Nat. Mater*, vol. 6, p. 183, 2007.

[4] K. S. Novoselov, V. I. Fal’ko, L. Colombo, P. R. Gellert, M. G. Schwab, and K. Kim, “A roadmap for graphene,” *Nature (London)*, vol. 490, p. 192, 2012.

[5] A. A. Balandin, “Thermal properties of graphene and nanostructured carbon materials,” *Nat. Mater*, vol. 10, p. 581, 2011.

[6] C. Lee, X. Wei, J. W. Kysar, and J. Hone, “Measurement of the elastic properties and intrinsic strength of monolayer graphene,” *Science*, vol. 321, p. 388, 2008.

[7] L. A. Falkovsky, “Optical properties of graphene,” *J. Phys.*, vol. 129, p. 012004, 2008.

[8] A. H. Castro Neto, F. Guinea, N. M. R. Peres, K. S. Novoselov, and A. K. Geim, “The electronic properties of graphene,” *Rev. Mod. Phys.*, vol. 81, p. 109, 2009.

[9] T. Odom, J. Huang, P. Kim, and C. Lieber, “Atomic structure and electronic properties of single-walled carbon nanotubes,” *Nature*, vol. 391, p. 62, 1998.

[10] R. Baughman, A. Zakhidov, and W. de Heer, “Carbon nanotubes-the route toward application,” *Science*, vol. 297, p. 787, 2002.

[11] S. Iijima, “Helical microtubules of graphitic carbon,” *Nature*, vol. 354, p. 58, 1991.

[12] L.-C. Qin, X. Zhao, K. Hirahara, Y. Miyamoto, Y. Ando, and S. Iijima, “The smallest carbon nanotube,” *Nature*, vol. 408, p. 50, 2000.

[13] G. D. Nessim, “Properties, synthesis and growth mechanisms of carbon nanotubes with special focus on thermal chemical vapor deposition,” *Nanoscale*, vol. 2, p. 1306, 2010.

[14] B. I. Kharisov, O. V. Kharissova, U. O. Méndez, and I. F. Gómez, “Decoration of carbon nanotubes with metal nanoparticles: recent trends,” *Synthesis and Reactivity in Inorganic, Metal-Organic, and Nano-Metal Chemistry*, 2015.

[15] S. J. Kim, K. Choi, B. Lee, Y. Kim, and B. H. Hong, “Materials for flexible, stretchable electronics: Graphene and 2d materials,” *Ann. Rev. Mater. Res.*, vol. 45, p. 84, 2015.

[16] N. G. Sahoo, “Polymer nanocomposites based on functionalized carbon nanotubes,” *Prog. Polym. Sci*, vol. 35, p. 837, 2010.

[17] Q. Wang and B. Arash, “Nanoresonators in sensors and molecular transportation: An introduction to the possibilities of carbon nanotubes and graphene sheets,” *IEEE Nanotechnol. Mag.*, vol. 8, p. 29, 2014.

[18] B. Arash, J.-W. Jiang, and T. Rabczuk, “A review on nanomechanical resonators and their applications in sensors and molecular transportation,” *Applied Physics Reviews*, vol. 2, no. 2, p. 021301, 2015.

[19] Z. Cao and B. B. Wei, “A perspective: carbon nanotube macro-films for energy storage,” *Ener. Environ. Sci.*, vol. 6, p. 3183, 2013.

[20] P. Simon and Y. Gogotsi, “Materials for electrochemical capacitors,” *Nat. Mater*, vol. 7, p. 845, 2008.

[21] W. Yang, G. Chen, Z. Shi, C.-C. Liu, L. Zhang, G. Xie, M. Cheng, D. Wang, R. Yang, D. Shi, K. Watanabe, T. Taniguchi, Y. Yao, Y. Zhang, and G. Zhang, “Epitaxial growth of single-domain graphene on hexagonal boron nitride,” *Nature Materials*, vol. 12, p. 792, 2013.

[22] J. Chaste, A. Eichler, J. Moser, R. Rurali, and A. Bachtold *Nat. Nanotechnol.*, vol. 7, p. 301, 2012.

[23] H. B. Peng, C. W. Chang, S. Aloni, T. D. Yuzvinsky, and A. Zettl, “Ul-

trahigh frequency nanotube resonators," *Phys. Rev. Lett.*, vol. 97, p. 087203, Aug 2006.

[24] B. Lassagne, D. Garcia-Sanchez, A. Aguasca, and A. Bachtold, "Ultrasensitive mass sensing with a nanotube electromechanical resonator," *Nano Lett.*, vol. 8, no. 11, pp. 3735–3738, 2008.

[25] H.-Y. Chiu, P. Hung, H. W. C. Postma, and M. Bockrath, "Atomic-scale mass sensing using carbon nanotube resonators," *Nano Lett.*, vol. 8, no. 12, pp. 4342–4346, 2008.

[26] J. Chaste, M. Sledzinska, M. Zdrojek, J. Moser, and A. Bachtold, "High-frequency nanotube mechanical resonators," *Applied Physics Letters*, vol. 99, no. 21, p. 213502, 2011.

[27] B. Arash, Q. Wang, and N. Wu, "Gene detection with carbon nanotubes," *J. Nanotech. Eng. Med.*, vol. 3, p. 020902, 2012.

[28] J. C. T. Eijkel and A. van den Berg, "Nanofluidics: what is it and what can we expect from it?," *Microfluid. Nanofluidics*, vol. 1, p. 249, 2005.

[29] B. Radha, A. Esfandiar, F. C. Wang, A. P. Rooney, K. Gopinadhan, A. Keerthi, A. Mishchenko, A. Janardanan, P. Blake, L. Fumagalli, M. Lozada-Hidalgo, S. Garaj, S. J. Haigh, I. V. Grigorieva, H. A. Wu, and A. K. Geim, "Molecular transport through capillaries made with atomic-scale precision," *Nature (London)*, vol. 538, p. 222, 2016.

[30] M. Majumder, N. Chopra, R. Andrews, and B. J. Hinds, "Nanoscale hydrodynamics: enhanced flow in carbon nanotubes," *Nature*, vol. 438, p. 44, 2005.

[31] M. Majumder, N. Chopra, and B. J. Hinds, "Mass transport through carbon nanotube membranes in three different regimes: ionic diffusion and gas and liquid flow," *ACS Nano*, vol. 5, p. 3867, 2011.

[32] J. K. Holt, H. G. Park, Y. Wang, M. Stadermann, A. B. Artyukhin, C. P. Grigoropoulos, A. Noy, and O. Bakajin, "Fast mass transport through sub-2-nanometer carbon nanotubes," *Science*, vol. 312, p. 1034, 2006.

[33] S. C. O'Hern, D. Jang, S. Bose, J.-C. Idrobo, Y. Song, T. Laoui, J. Kong, and R. Karnik, "Nanofiltration across defect-sealed nanoporous monolayer graphene," *Nano Lett.*, vol. 15, p. 3254, 2015.

[34] M. Chaplin, "Water structure and science." `http://www1.lsbu.ac.uk/water/`.

[35] M. Boero, K. Terakura, T. Ikeshoji, C. Liew, and M. Parrinello, "Hydrogen bonding and dipole moment of water at supercritical conditions: A first-principles molecular dynamics study.," *Phys. Rev. Lett.*, vol. 82, p. 3245, 2000.

[36] E. Schwegler, G. Galli, F. Gygi, and R. Q. Hood, "Dissociation of water under pressure," *Phys. Rev. Lett.*, vol. 87, p. 265501, 2001.

[37] M. Ceriotti, J. Cuny, M. Parrinello, and D. E. Manolopoulos, "Nuclear quantum effects and hydrogen bond fluctuations in water," *PNAS*, vol. 110, p. 15591, 2013.

[38] E. A. Zheligovskaya and G. G. Malenkov, "Crystalline water ices," *Russ. Chem. Rev*, vol. 75, pp. 57–76, 2006.

[39] P. Wernet, D. Nordlund, U. Bergmann, M. Cavalleri, M. Odelius, H. Ogasawara, L. Å. Näslund, T. K. Hirsch, L. Ojamäe, P. Glatzel, L. G. M. Pettersson, and A. Nilsson, "The structure of the first coordination shell in liquid water," *Science*, vol. 304, no. 5673, pp. 995–999, 2004.

[40] I. Tinoco, K. Sauer, and J. C. Wang, *Physical Chemistry: Principles and Applications in Biological Sciences*.
Pretince-Hall, 3 ed., 1995.

[41] D. Marx, M. E. Tuckerman, J. Hutter, and M. Parrinello, "The nature of the hydrated excess proton in water," *Nature*, vol. 397, p. 601, 1999.

[42] P. Geissler, C. Dellago, D. Chandler, J. Hutter, and M. Parrinello, "Autoionization in liquid water," *Science*, vol. 291, p. 2121, 2001.

[43] A. Hassanali, M. K. Prakash, and H. Eshet, "On the recombination of hydronium and hydroxide ions in water," *PNAS*, vol. 108, p. 20410, 2011.

[44] N. Agmon, "The Grotthuss mechanism," *Chem. Phys. Lett.*, vol. 244, p. 456, 1995.

[45] R. Zangi and A. E. Mark, "Electrofreezing of confined water," *J. Chem. Phys.*, vol. 120, p. 7123, 2004.

[46] H. Qiu and W. Guo, "Electromelting of confined monolayer ice," *Phys. Rev. Lett.*, vol. 110, p. 195701, 2013.

[47] G. Cassone, P. V. Giaquinta, S. F., and A. M. Saitta, "Proton conduction in water ices under an electric field," *J. Phys. Chem. B*, vol. 118, p. 4419, 2014.

[48] A. Saitta, F. Saija, and P. V. Giaquinta, "Ab initio molecular dynamics study of dissociation of water under an electric field," *Phys. Rev. Lett.*, vol. 108, p. 207801, 2012.

[49] M. Otani, T. Hamada, O. Sugino, Y. Morikawa, Y. Okamoto, and T. Ikeshoji, "Electrode dynamics from first principles," *Journal of Phys. Soc. Japan*, vol. 77, p. 024802, 2008.

[50] L. J. Michot, F. Villi'eras, M. François, I. Bihannic, M. Pelletier, and J.-M. Cases, "Water organisation at the solid-aqueous solution interface," *Comptes Rendus Geoscience*, vol. 334, p. 611, 2002.

[51] J. Chen, A. Zen, J. G. Brandenburg, D. Alfe, and A. Michaelides, "Evidence for stable square ice from quantum monte carlo," *Phys. Rev. B*, vol. 94, p. 220102, 2016.

[52] L. Zhu, G. Lu, S. Mao, D. A. Dikin, X. Chen, and R. S. Ruoff *NANO*, vol. 02, p. 149, 2007.

[53] F. Corsetti, P. Matthews, and E. Artacho, "Structural and configurational properties of nanoconfined monolayer ice from first principles," *Sci. Rep.*, vol. 6, p. 18651, 2016.

[54] M. Sobrino Fernandez, F. M. Peeters, and M. Neek-Amal, "Electric field induced structural changes of water confined between two graphene layers," *Phys. Rev. B*, vol. 94, p. 045436, 2016.

[55] M. Sobrino Fernandez, F. M. Peeters, and M. Neek-Amal, "AA-stacked bilayer square ice between graphene layers," *Phys. Rev. B*, vol. 92, p. 245428, 2015.

[56] M. Raju, A. van Duin, and M. Ihme, "Phase transitions of ordered ice in graphene nanocapillaries and carbon nanotubes," *Sci. Rep.*, vol. 8, p. 3851, 2018.

[57] L. Kelvin, "Baltimore lectures on molecular dynamics and the wave theory of light." CUP, 1904.

[58] R. Car and M. Parrinello, "Unified approach for molecular dynamics and density-functional theory," *Phys. Rev. Lett.*, vol. 55, p. 2471,

1985.

[59] L. Verlet, “Computer “experiments" on classical fluids. I. Thermodynamical properties of Lennard-Jones molecules,” *Phys. Rev.*, vol. 159, p. 98, 1967.

[60] S. Nosé, “A unified formulation of the constant temperature molecular dynamics methods,” *J. Chem. Phys*, vol. 81, p. 511, 1984.

[61] W. G. Hoover, “Canonical dynamics: Equilibrium phase-space distributions,” *Phys. Rev. A*, vol. 31, p. 1695, 1985.

[62] H. C. Andersen, “Molecular dynamics simulations at constant pressure and/or temperature,” *J. Chem. Phys.*, vol. 72, p. 2384, 1980.

[63] W. G. Hoover, “Constant-pressure equations of motion,” *Phys. Rev. A*, vol. 34, p. 2499, 1986.

[64] M. Parrinello and A. Rahman, “Crystal structure and pair potentials: A molecular-dynamics study,” *Phys. Rev. Lett.*, vol. 45, p. 1196, 1980.

[65] D. Frenkel and B. Smit, *Understanding Molecular Simulation*. Academic Press, San Diego, 2002.

[66] L. D. Landau and E. M. Lifshitz, *Statistical Physics*. Butterworth-Heinemann, Oxford, 1996.

[67] J.-P. Hansen and I. R. McDonald, *Theory of Simple Liquids*. Academic Press, London, 3 ed., 2006.

[68] F. Jense, *Introduction to Computational Chemistry*. Qilley, Chichester, 2 ed.

[69] J. E. Jones, “On the determination of molecular fields. II. from the equation of state of a gas,” *Proc. R. Soc. Lond. A*, vol. 106, pp. 463–477, 1924.

[70] M. Oobatake and T. Ooi, “Determination of energy parameters in lennard-jones potentials from second virial coefficients,” *Progress of Theoretical Physics*, vol. 48, no. 6, pp. 2132–2143, 1972.

[71] S. Erkoç, *Annu. Rev. Comput. Phys. IX*, vol. 1. World Scientific, 2001.

[72] D. Yin and A. D. MacKerell, “Combined ab initio/empirical approach for optimization of lennard–jones parameters,” *Journal of Computational Chemistry*, vol. 19, no. 3, pp. 334–348, 1998.

[73] W. L. Jorgensen, J. Chandrasekhar, J. D. Madura, R. W. Impey, and M. L. Klein, “Comparison of simple potential functions for simulating liquid water,” *J. Chem. Phys.*, vol. 79, p. 926, 1983.

[74] M. S. Daw and M. I. Baskes, “Semiempirical, quantum mechanical calculation of hydrogen embrittlement in metals,” *Phys. Rev. Lett.*, vol. 50, p. 1285, 1983.

[75] S. M. Foiles, M. I. Baskes, and M. S. Daw, “Embedded-atom-method functions for the fcc metals Cu, Ag, Au, Ni, Pd, Pt, and their alloys,” *Phys. Rev. B*, vol. 33, pp. 7983–7991, Jun 1986.

[76] D. W. Brenner, “Empirical potential for hydrocarbons for use in simulating the chemical vapor deposition of diamond films,” *Phys. Rev. B*, vol. 42, p. 9458, 1990.

[77] S. J. Stuart, A. B. Tutein, and J. A. Harrison, “A reactive potential for hydrocarbons with intermolecular interactions,” *The Journal of Chemical Physics*, vol. 112, no. 14, pp. 6472–6486, 2000.

[78] T. P. Senftle, S. Hond, M. M. Islam, S. B. Kylasa, Y. Zheng, Y. K. Shin, C. Junkermeier, R. Engel-Herbert, M. J. Janik, H. M. Aktulga, T. Verstraelen, and A. C. T. van Duin, “The ReaxFF reactive force-field: development, applications and future directions,” *NPJ Comput. Mater.*, vol. 2, p. 15011, 2016.

[79] A. C. T. van Duin, S. Dasgupta, F. Lorant, and W. A. Goddard III, “ReaxFF: A reactive force field for hydrocarbons,” *J. Phys. Chem. A*, vol. 105, p. 9396, 2001.

[80] W. J. Mortier, S. K. Ghosh, and S. Shankar, “Electronegativity Equalization Method for the calculation of atomic charges in molecules,” *J. Am. Chem. Soc.*, vol. 108, p. 4315, 1986.

[81] A. K. Rappe and W. A. Goddard III, “Charge equilibration for molecular dynamics simulations,” *J. Phys. Chem.*, vol. 95, p. 3358, 1991.

[82] M. F. Russo and A. C. T. van Duin, “Atomistic-scale simulations of chemical reactions: Bridging from quantum chemistry to engineering.,” *Nuclear Instruments and Methods in Physics Research Section B: Beam Interaction with Materials and Atoms*, vol. 269, p. 1549, 2011.

[83] S. Plimpton, “Fast parallel algorithms for short-range molecular dy-

namics," *J. Comp. Phys.*, vol. 117, no. 1, pp. 1 – 19, 1995.

[84] A. P. Thompson, S. J. Plimpton, and W. Mattson *J. Chem. Phys*, vol. 131, p. 154107, 2009.

[85] B. A. Luty, M. E. Davis, I. G. Tironi, and W. F. Van Gunsteren, "A comparison of particle-particle particle-mesh and Ewald methods for calculating electrostatic interactions in periodic molecular systems," *Molecular Simulation*, vol. 14, p. 11, 1994.

[86] R. W. Hockney and J. W. Eastwood, *Computer simulation using particles*.
Adam Hilger, NY, 1989.

[87] E. L. Pollock and J. Glosli, "Comments on P3M, FMM and the Ewald method for large periodic Coulombic systems," *Comp. Phys. Comm*, vol. 95, p. 93, 1996.

[88] S. T. Purcell, P. Vincent, C. Journet, and V. T. Binh, "Tuning of nanotube mechanical resonances by electric field pulling," *Phys. Rev. Lett.*, vol. 89, p. 276103, Dec 2002.

[89] Z. Wang and L. Philippe, "Deformation of doubly clamped single-walled carbon nanotubes in an electrostatic field," *Phys. Rev. Lett.*, vol. 102, p. 215501, May 2009.

[90] V. Vasumathi, D. Pramanik, A. K. Sood, and P. K. Maiti *Soft Matter*, vol. 9, p. 1372, 2013.

[91] G. Romero and S. E. Moya *Soft Matter*, vol. 8, p. 9727, 2012.

[92] B. R. H. de Aquino, M. Neek-Amal, and M. V. Milošević, "Unconventional two-dimensional vibrations of a decorated carbon nanotube under electric field: linking actuation to advanced sensing ability," *Sci. Rep*, vol. 7, p. 13481, 2017.

[93] M. M. J. Treacy, T. W. Ebbesen, and J. M. Gibson *Nature*, vol. 381, p. 678, 1996.

[94] S. J. Tans, M. H. Devoret, H. Dai, A. Thess, R. E. Smalley, L. J. Geerligs, and C. Dekker *Nature*, vol. 386, p. 474, 1997.

[95] F. Xin and L. Li *Composites Part A*, vol. 42, no. 8, p. 961, 2006.

[96] S. Fullam, D. Cottell, H. Rensmo, and D. Fitzmaurice *Adv. Mater.*, vol. 12, p. 1430, 2000.

[97] V. Georgakilas, D. Gournis, V. Tzitzios, L. Pasquato, D. M. Guldi, and M. Prato, “Decorating carbon nanotubes with metal or semiconductor nanoparticles,” *J. Mater. Chem.*, vol. 17, pp. 2679–2694, 2007.

[98] C. Feng, J. Wang, Y. Cheng, P. He, and K. M. Liew *RSC Adv.*, vol. 4, p. 60711, 2014.

[99] J.-C. Charlier *Acc. Chem. Res.*, vol. 35, p. 1063, 2002.

[100] T. M. Day, P. R. Unwin, N. R. Wilson, and J. V. Macpherson *J. Am. Chem. Soc.*, vol. 127, p. 10647, 2005.

[101] M. Correa-Duarte, J. Perez-Juste, A. Sanchez-Iglesias, M. Giersig, and L. Liz-Marzan *Angew. Chem., Int. Ed.*, vol. 44, p. 4375, 2005.

[102] A. Ongaro, F. Griffin, P. Beecher, L. Nagle, D. Iacopino, A. Quinn, G. Redmond, and D. Fitzmaurice *Chem. Mater.*, vol. 17, no. 8, p. 1959, 2005.

[103] K. Zhang, J. Ji, X. Fang, L. Yan, and B. Liu *Analyst*, vol. 140, no. 1, p. 134, 2015.

[104] B. Wu, Y. Kuang, X. Zhang, and J. Chen *Nano Today*, vol. 6, p. 75, 2011.

[105] G. Wildgoose, C. Banks, and R. Compton *Small*, vol. 2, no. 2, p. 182, 2006.

[106] T. M. Day, P. R. Unwin, and J. V. Macpherson *Nano Lett.*, vol. 7, no. 1, p. 51, 2007.

[107] D. Gingery and P. Bühlmann *Carbon*, vol. 46, p. 1966, 2008.

[108] M. Neek-Amal, R. Asgari, and M. R. R. Tabar, “The formation of atomic nanoclusters on graphene sheets,” *Nanotechnology*, vol. 20, no. 13, p. 135602, 2009.

[109] P. A. E. Schoen, J. H. Walther, S. Arcidiacono, D. Poulikakos, and P. Koumotsakos, “Nanoparticle traffic on helical tracks: thermophoretic mass transport through carbon nanotubes,” *Nano Lett*, vol. 6, p. 1910, 2006.

[110] V. Sazanova, Y. Yaish, H. Üstünel, D. Roundy, T. A. Arias, and P. L. McEuen *Nature*, vol. 431, p. 284, 2004.

[111] V. A. Sazonova, *A Tunable Carbon Nanotube Resonator*.
PhD thesis, Cornell University, 8 2006.

[112] S. Sapmaz, Y. M. Blanter, L. Gurevich, and H. S. J. van der Zant, “Carbon nanotubes as nanoelectromechanical systems,” *Phys. Rev.*

B, vol. 67, p. 235414, Jun 2003.

[113] I. W. Frank, D. M. Tanenbaum, A. M. van der Zande, and P. L. McEuen *J. Vac. Sci. Technol. B*, vol. 25, p. 2558, 2007.

[114] H. Javaheri, B. Barbiellini, and G. Noubir, "Energy transfer performance of mechanical nanoresonators coupled with electromagnetic fields," *Nanoscale Research Letters*, vol. 7, no. 1, p. 572, 2012.

[115] X. M. H. Huang, X. L. Feng, C. A. Zorman, M. Mehregany, and M. L. Roukes, "VHF, UHF and microwave frequency nanomechanical resonators," *New J. Phys.*, vol. 7, no. 1, p. 247, 2005.

[116] H.-J. Chen and K.-D. Zhu, "Graphene-based nanoresonator with applications in optical transistor and mass sensing," *Sensors*, vol. 14, no. 9, pp. 16740–16753, 2014.

[117] H. J. Mamin and D. Rugar, "Sub-attonewton force detection at millikelvin temperatures," *Appl. Phys. Lett.*, vol. 79, p. 3358, 2001.

[118] B. Ilic, H. G. Craighead, S. Krylov, W. Senaratne, C. Ober, and P. Neuzil, "Attogram detection using nanoelectromechanical oscillators," *Journal of Applied Physics*, vol. 95, no. 7, pp. 3694–3703, 2004.

[119] K. L. Ekinci, X. M. H. Huang, and M. L. Roukes, "Ultrasensitive nanoelectromechanical mass detection," *Applied Physics Letters*, vol. 84, no. 22, pp. 4469–4471, 2004.

[120] A. Eichler, J. Moser, M. I. Dykman, and A. Bachtold *Nat. Commun.*, vol. 4, p. 2843, 2013.

[121] P. Poncharal, Z. L. Wang, D. Ugarte, and W. A. de Heer, "Electrostatic deflections and electromechanical resonances of carbon nanotubes," *Science*, vol. 283, no. 5407, pp. 1513–1516, 1999.

[122] K. Jensen, K. Kim, and A. Zettl, "An atomic-resolution nanomechanical mass sensor," *Nat. Nanotechnol.*, vol. 3, p. 533, 2008.

[123] C. Wang, J. Kim, Y. Zhu, J. Yang, G.-H. Lee, S. Lee, J. Yu, R. Pei, G. Liu, C. Nuckolls, J. Hone, and Q. Lin, "An aptameric graphene nanosensor for label-free detection of small-molecule biomarkers," *Biosens. Bioelectron.*, vol. 71, pp. 222 – 229, 2015.

[124] T. Thundat, E. A. Wachter, S. L. Sharp, and R. J. Warmack, "Detection of mercury vapor using resonating microcantilevers," *Applied Physics*

Letters, vol. 66, no. 13, pp. 1695–1697, 1995.

[125] Y. Weizmann, D. M. Chenoweth, and T. M. Swager, “DNA-CNT nanowire networks for DNA detection,” *Journal of the American Chemical Society*, vol. 133, no. 10, pp. 3238–3241, 2011.

[126] P. M. Kosaka, V. Pini, J. J. Ruz, R. A. da Silva, M. U. González, D. Ramos, M. Calleja, and J. Tamayo, “Detection of cancer biomarkers in serum using a hybrid mechanical and optoplasmonic nanosensor,” *Nat. Nanotechnol.*, vol. 9, p. 1047, 2014.

[127] S. B. Legoas, V. R. Coluci, S. F. Braga, P. Z. Coura, S. O. Dantas, and D. S. Galvão, “Gigahertz nanomechanical oscillators based on carbon nanotubes,” *Nanotechnology*, vol. 15, no. 4, p. S184, 2004.

[128] Q. Zheng and Q. Jiang, “Multiwalled carbon nanotubes as gigahertz oscillators,” *Phys. Rev. Lett.*, vol. 88, p. 045503, Jan 2002.

[129] E. A. Laird, F. Pei, W. Tang, G. A. Steele, and L. P. Kouwenhoven, “A high quality factor carbon nanotube mechanical resonator at 39 GHz,” *Nano Lett.*, vol. 12, no. 1, pp. 193–197, 2012.

[130] A. K. Hüttel, G. A. Steele, B. Witkamp, M. Poot, L. P. Kouwenhoven, and H. S. J. van der Zant, “Carbon nanotubes as ultrahigh quality factor mechanical resonators,” *Nano Letters*, vol. 9, no. 7, pp. 2547–2552, 2009.

[131] J. Moser, A. Eichler, J. Güttinger, M. I. Dykman, and A. Bachtold, “Nanotube mechanical resonators with quality factors of up to 5 million,” *Nat. Nano.*, vol. 9, pp. 1007–1011, 2014.

[132] L. N. Lewis, “Chemical catalysis by colloids and clusters,” *Chem. Rev.*, vol. 93, no. 8, pp. 2693–2730, 1993.

[133] P. V. Kamat, “Photophysical, photochemical and photocatalytic aspects of metal nanoparticles,” *J. Phys. Chem. B*, vol. 106, no. 32, pp. 7729–7744, 2002.

[134] H. Arakawa, J. Neault, and H. Tajmir-Riahi, “Silver(I) complexes with DNA and RNA studied by fourier transform infrared spectroscopy and capillary electrophoresis,” *Biophys. J.*, vol. 81, no. 3, pp. 1580 – 1587, 2001.

[135] Y. Sun and Y. Xia, “Shape-controlled synthesis of gold and silver

nanoparticles," *Science*, vol. 298, no. 5601, pp. 2176–2179, 2002.

[136] A. Abdelhalim, A. Abdellah, G. Scarpa, and P. Lugli, "Metallic nanoparticles functionalizing carbon nanotube networks for gas sensing applications," *Nanotechnology*, vol. 25, no. 5, p. 055208, 2014.

[137] J. L. Elechiguerra, J. L. Burt, J. R. Morones, A. Camacho-Bragado, X. Gao, H. H. Lara, and M. J. Yacaman, "Interaction of silver nanoparticles with HIV-1," *Journal of Nanobiotechnology*, vol. 3, no. 1, p. 6, 2005.

[138] F. Furno, K. S. Morley, B. Wong, B. L. Sharp, P. L. Arnold, S. M. Howdle, R. Bayston, P. D. Brown, P. D. Winship, and H. J. Reid, "Silver nanoparticles and polymeric medical devices: a new approach to prevention of infection?," *J.Antimicrob. Chemother.*, vol. 54, no. 6, p. 1019, 2004.

[139] J. Kong, M. G. Chapline, and H. Dai, "Functionalized carbon nanotubes for molecular hydrogen sensors," *Adv. Mater.*, vol. 13, no. 18, pp. 1384–1386, 2001.

[140] Q. Zhao, M. Buongiorno Nardelli, W. Lu, and J. Bernholc, "Carbon nanotube-metal cluster composites: A new road to chemical sensors?," *Nano Lett.*, vol. 5, no. 5, pp. 847–851, 2005.

[141] W. G. Conley, A. Raman, C. M. Krousgrill, and S. Mohammadi, "Nonlinear and nonplanar dynamics of suspended nanotube and nanowire resonators," *Nano Lett.*, vol. 8, no. 6, pp. 1590–1595, 2008.

[142] E. Gil-Santos, D. Ramos, J. Marínez, M. Fernández-Regúlez, R. García, A. San Paulo, M. Calleja, and J. Tamayo, "Nanomechanical mass sensing and stiffness spectrometry based on two-dimensional vibrations of resonant nanowires," *Nat. Nanotechnol.*, vol. 5, p. 641, 2010.

[143] Z. K. Tang, N. Wang, X. X. Zhang, J. N. Wang, C. T. Chan, and P. Sheng, "Novel properties of 0.4 nm single-walled carbon nanotubes templated in the channels of $AlPO_4$-5 single crystals," *New Journal of Physics*, vol. 5, no. 1, p. 146, 2003.

[144] J. T. Ye, Z. M. Li, Z. K. Tang, and R. Saito, "Raman spectra of lithium doped single-walled 0.4 nm carbon nanotubes," *Phys. Rev. B*, vol. 67,

p. 113404, Mar 2003.

[145] F. Buonocore, “First-principles investigation of the interaction of gold and palladium with armchair carbon nanotube,” *Molecular Simulation*, vol. 36, no. 10, pp. 729–735, 2010.

[146] W. Zhu and E. Kaxiras, “The nature of contact between Pd leads and semiconducting carbon nanotubes,” *Nano Letters*, vol. 6, no. 7, pp. 1415–1419, 2006.

[147] L. Hu, X. Hu, X. Wu, C. Du, Y. Dai, and J. Deng, “Density functional calculation of transition metal adatom adsorption on graphene,” *Physica B: Condensed Matter*, vol. 405, no. 16, pp. 3337 – 3341, 2010.

[148] A. Ishii, M. Yamamoto, H. Asano, and K. Fujiwara, “DFT calculation for adatom adsorption on graphene sheet as a prototype of carbon nanotube functionalization,” *Journal of Physics: Conference Series*, vol. 100, no. 5, p. 052087, 2008.

[149] S.-P. Huang, D. S. Mainardi, and P. B. Balbuena, “Structure and dynamics of graphite-supported bimetallic nanoclusters,” *Surface Science*, vol. 545, no. 3, pp. 163 – 179, 2003.

[150] S. K. R. S. Sankaranarayanan, V. R. Bhethanabotla, and B. Joseph, “Molecular dynamics simulations of the structural and dynamic properties of graphite-supported bimetallic transition metal clusters,” *Phys. Rev. B*, vol. 72, p. 195405, Nov 2005.

[151] L. D. Landau and E. M. Lifshitz, *Theory of Elasticity*.
Nauka, 1987.

[152] Q. Yang, Y. Su, C. Chi, C. T. Cherian, K. Huang, V. G. Kravets, F. C. Wang, J. C. Zhang, A. Pratt, A. N. Grigorenko, F. Guinea, G. A. K., and R. R. Nair, “Ultrathin graphene-based membrane with precise molecular sieving and ultrafast solvent permeation,” *Nat. Mater*, vol. 16, p. 1198, 2017.

[153] C. M. Harris and A. G. Piersol, *Harris’ Schock and Vibration Handbook*.
McGraw-Hill, 2002.

[154] H. J. Huang, Y. Zhang, Y. L. Ke, N. S. Xu, and S. Z. Deng, “A modulated field emission from carbon nanotubes cold cathode cavity resonator

in L band frequency," *IEEE Xplore, Vacuum Nanoelectronics Conference (IVNC), 2015 28th International*, 2015.

[155] F. Patolsky, Y. Weizmann, and I. Willner, "Actin-based metallic nanowires as bio-nanotransporters," *Nature Materials*, vol. 3, p. 692, 2004.

[156] J. K. Holt, "Carbon nanotubes and nanofluidic transport," *Adv. Mater.*, vol. 21, p. 3542, 2009.

[157] X. Qin, Q. Yuan, Y. Zhao, S. Xie, and Z. Liu, "Measurement of the rate of water translocation through carbon nanotubes," *Nano Lett.*, vol. 11, p. 2173, 2011.

[158] J. Köfinger, G. Hummer, and C. Dellago, "Macroscopically ordered water in nanopores," *Proc. Natl. Acad. Sci. U. S. A*, vol. 105, p. 13218, 2008.

[159] R. Zangi and A. E. Mark, "Monolayer ice," *Phys. Rev. Lett.*, vol. 91, p. 025502, 2003.

[160] R. Zangi and A. E. Mark, "Bilayer ice and alternate liquid phases of confined water," *J. Chem. Phys*, vol. 119, p. 1964, 2003.

[161] G. Algara-Siller, O. Lehtinen, F. C. Wang, R. R. Nair, U. Kaiser, H. A. Wu, A. K. Geim, and I. V. Grigorieva, "Square ice in graphene nanocapillaries," *Nature*, vol. 519, p. 443, 2015.

[162] M. Neek-Amal, F. M. Peeters, I. V. Grigorieva, and A. K. Geim, "Commensurability effects in viscosity of nanoconfined water," *ACS Nano*, vol. 10, p. 3685, 2016.

[163] L. Yang, Y. Guo, and D. Diao, "Structure and dynamics of water confined in a graphene nanochannel under gigapascal high pressure: dependence of friction on pressure and confinement," *Phys. Chem. Chem. Phys.*, vol. 19, p. 14048, 2017.

[164] G. D. Bixler and B. Bhushan, "Bioinspired micro/nanostructured surfaces for oil drag reduction in closed channel flow," *Soft Matter*, vol. 9, p. 1620, 2013.

[165] X. Li, H. Qiu, X. Liu, J. Yin, and W. Guo, "Wettability of supported monolayer hexagonal boron nitride in air," *Adv. Funct. Mater.*, vol. 27, p. 1603181, 2017.

[166] H. Li and X. C. Zeng, "Wetting and interfacial properties of water

nanodroplets in contact with graphene and monolayer boron–nitride sheets," *ACS Nano*, vol. 6, p. 2401, 2012.

[167] F. Sedlmeier, J. Janecek, C. Sendner, L. Bocquet, R. R. Netz, and D. Horinek, "Water at polar and nonpolar solid walls," *Biointerphases*, vol. 3, p. FC23, 2008.

[168] M. N.-A. et. al *under review*, 2017.

[169] V. Satarifard, M. Mousaei, F. Hadadi, J. Dix, M. Sobrino Fernandez, P. Carbone, J. Beheshtian, F. M. Peeters, and M. Neek-Amal, "Reversible structural transition in nanoconfined ice," *Phys. Rev. B.*, vol. 95, p. 064105, 2017.

[170] P. Kumar, S. V. Buldyrev, F. W. Starr, N. Giovambattista, and H. Eugene Stanley, "Thermodynamics, structure, and dynamics of water confined between hydrophobic plates," *Phys. Rev. E.*, vol. 72, p. 051503, 2005.

[171] H. Mosaddeghi, S. Alavi, M. H. Kowsari, and B. Najafi, "Simulations of structural and dynamic anisotropy in nano-confined water between parallel graphite plates," *J. Chem. Phys.*, vol. 137, p. 184703, 2012.

[172] S. Vaitheeswaran, H. Yin, and J. C. Rasaiah, "Water between plates in the presence of an electric field in an open system," *J. Phys. Chem. B*, vol. 109, p. 6629, 2005.

[173] H. S. Frank *J. Chem. Phys*, vol. 23, p. 2023, 1955.

[174] K. S. Vasu, E. Prestat, J. Abraham, J. Dix, R. J. Kashtiban, J. Beheshtian, J. Sloan, P. Carbone, M. Neek-Amal, S. J. Haigh, A. K. Geim, and R. R. Nair, "Van der waals pressure and its effect on trapped interlayer molecules," *Nature Commun.*, vol. 7, p. 12168, 2016.

[175] T. W. Sirk, S. Moore, and E. F. Brown *J. Chem. Phys*, vol. 138, p. 064505, 2013.

[176] R. Zangi and S. A. Rice, "Phase transitions in a quasi-two-dimensional system," *Phys. Rev. E*, vol. 58, p. 7529, 1998.

[177] F. Corsetti, J. Zubeltzu, and E. Artacho, "Enhanced configurational entropy in high-density nanoconfined bilayer ice," *Phys. Rev. Lett.*, vol. 116, p. 085901, 2016.

[178] J. Chen, G. Schusteritsch, C. J. Pickard, C. G. Salzmann, and

A. Michaelides, “Two dimensional ice from first principles: Structures and phase transitions,” *Phys. Rev. Lett.*, vol. 6, p. 025501, 2016.

[179] R. Zangi, “Water confined to a slab geometry: a review of recent computer simulation studies,” *J. Phys.: Condens. Matter*, vol. 16, p. S5371, 2004.

[180] W. Zhou, K. Yin, C. Wang, Y. Zhang, T. Xu, A. Borisevich, L. Sun, J. C. Idrobo, M. F. Chisholm, S. T. Pantelides, R. F. Klie, and A. R. Lupini, “The observation of square ice in graphene questioned,” *Nature*, vol. 528, p. 7583, 2015.

[181] L. I. V. and A. A. Stuchebrukhov, “Electronic polarizability and the effective pair potentials of water,” *J. Chem. Theory Comput.*, vol. 6, p. 3153, 2010.

[182] H. Ghorbanfekr-Kalashami, K. S. Vasu, R. R. Nair, F. M. Peeters, and M. Neek-Amal, “Dependence of the shape of graphene nanobubbles on trapped substance,” *Nature Commun.*, vol. 8, p. 15844, 2017.

[183] K. Yue, W. Gao, R. Huang, and K. M. Liechti, “Analytical methods for the mechanics of graphene bubbles,” *J. Appl. Phys*, vol. 112, p. 083512, 2012.

[184] R. Nair, H. A. Wu, P. N. Jayaram, I. V. Grigorieva, and A. K. Geim, “Unimpeded permeation of water through helium-leak–tight graphene-based membranes,” *Science*, vol. 335, p. 442, 2012.

[185] R. K. Joshi, P. Carbone, F. C. Wang, V. G. Kravets, Y. Su, I. V. Grigorieva, H. A. Wu, A. K. Geim, and R. R. Nair, “Precise and ultrafast molecular sieving through graphene oxide membranes,” *Science*, vol. 343, p. 752, 2014.

[186] A. Esfandiar, B. Radha, F. C. Wang, Q. Yang, S. Hu, S. Garaj, R. R. Nair, A. K. Geim, and K. Gopinadhan, “Size effect in ion transport through angstrom-scale slits,” *Science*, vol. 358, p. 511, 2017.

[187] K.-G. Zhou, K. S. Vasu, C. T. Cherian, M. Neek-Amal, J. C. Zhang, H. Ghorbanfekr-Kalashami, K. Huang, O. P. Marshall, V. G. Kravets, J. Abraham, Y. Su, A. N. Grigorenko, A. Pratt, A. K. Geim, F. M. Peeters, K. S. Novoselov, and R. R. Nair, “Electrically controlled

water permeation through graphene oxide membranes," *Nature*, vol. 559, p. 236, 2018.

[188] L. Chen, G. Shi, J. Shen, B. Peng, B. Zhang, Y. Wang, F. Bian, J. Wang, D. Li, Z. Qian, G. Xu, J. Zeng, L. Zhang, Y. Yang, G. Zhou, M. Wu, W. Jin, J. Li, and H. Fang, "Ion sieving in graphene oxide membranes via cationic control of interlayer spacing," *Nature (London)*, vol. 550, p. 380, 2017.

[189] J. Abraham, K. S. Vasu, C. D. Williams, K. Gopinadhan, Y. Su, C. T. Cherian, J. Dix, E. Prestat, S. J. Haigh, I. V. Grigorieva, P. Carbone, G. A. K., and R. R. Nair, "Tunable sieving of ions using graphene oxide membranes," *Nat. Nanotechnol*, vol. 12, p. 546, 2017.

[190] L. Fumagalli, A. Esfandiar, R. Fabregas, S. Hu, P. Ares, A. Janardanan, Q. Yang, B. Radha, T. Taniguchi, K. Watanabe, G. Gomila, K. S. Novoselov, and A. K. Geim, "Anomalously low dielectric constant of confined water," *Science*, vol. 360, p. 1339, 2018.

[191] M. Tuckerman, K. Laasonent, M. Sprik, and M. Parrinello, "Ab initio molecular dynamics simulation of the solvation and transport of hydronium and hydroxyl ions in water," *J. Chem. Phys.*, vol. 103, p. 150, 1995.

[192] M. E. Tuckerman, K. Laasonent, M. Sprik, and M. Parrinello, "Ab initio simulations of water and water ions," *J. Phys.: Condens. Matter*, vol. 6, pp. A93–A100, 1994.

[193] M. E. Tuckerman, D. Marx, and M. Parrinello, "The nature and transport mechanism of hydrated hydroxide ions in aqueous solution," *Nature*, vol. 417, p. 925–929, 2002.

[194] X. Li, V. E. Teige, and S. S. Iyengar, "Can the four-coordinated, penta-valent oxygen in hydroxide water clusters be detected through experimental vibrational spectroscopy?," *J. Phys. Chem. A*, vol. 111, pp. 4815–4820, 2007.

[195] H. Itoh and H. Sakuma, "Dielectric constant of water as a function of separation in a slab geometry: A molecular dynamics study," *J. Chem. Phys*, vol. 142, p. 184703, 2015.

[196] B. R. H. de Aquino, H. Ghorbanfekr-Kalashami, M. Neek-Amal, and

F. M. Peeters, “Electrostrictive behavior of confined water subjected to gpa pressure,” *Phys. Rev. B*, vol. 97, p. 144111, 2018.

[197] I. Ohmine and H. Tanaka, “Fluctuation, relaxations, and hydration in liquid water. hydrogen-bond rearrangement dynamics,” *Chem. Rev.*, vol. 93, pp. 2545–2566, 1993.

[198] P. L. Geissler, C. Dellago, D. Chandler, J. Hutter, and M. Parrinello, “Autoionization in liquid water,” *Science*, vol. 291, pp. 2121–2124, 2001.

[199] M. Eigen, “Proton transfer, acid-base catalysis, and enzymatic hydrolysis. Part I: ELEMENTARY PROCESSES.,” *Angew. Chem. Int. Ed. Engl.*, vol. 3, pp. 1–19, 1964.

[200] W. Zhang and A. C. T. van Duin, “Second-generation ReaxFF water force field: Improvements in the description of water density and OH-anion diffusion,” *J. Phys. Chem. B*, vol. 121, pp. 6021–6032, 2017.

[201] W. Zhang and A. C. T. van Duin, “Improvement of the ReaxFF description for functionalized hydrocarbon/water weak interactions in the condensed phase,” *J. Phys. Chem. B*, vol. 122, pp. 4083–4092, 2018.

[202] “CPMD.” Copyright IBM Corp 1990-2015, Copyright MPI für Festkörperforschung Stuttgart 1997-2001.

[203] S. Grimme, “Semiempirical gga-type density functional constructed with a long-range dispersion correction,” *J. Comput. Chem.*, vol. 27, p. 1787, 2006.

[204] R. Z. Khaliullin and T. D. Kühne, “Microscopic properties of liquid water from combined ab initio molecular dynamics and energy decomposition studies,” *Phys. Chem. Chem. Phys.*, vol. 15, p. 15746, 2013.

[205] S. Izvekov and G. A. Voth, “Car–parrinello molecular dynamics simulation of liquid water: New results,” *J. Chem. Phys.*, vol. 116, p. 10372, 2002.

[206] B. Chen, I. Ivanov, J. M. Park, M. Parrinello, and M. L. Klein, “Solvation structure and mobility mechanism of OH-: A car-parrinello molecular dynamics investigation of alkaline solutions,” *J. Phys.*

Chem. B, vol. 106, pp. 12006–12016, 2002.

[207] A. Botti, F. Bruni, S. Imperti, and M. A. Ricci, “Solvation of hydroxyl ions in water,” *J. Chem. Phys.*, vol. 119, p. 5001, 2003.

[208] S. Imberti, A. Botti, F. Bruni, G. Cappa, M. A. Ricci, and A. K. Soper, “Ions in water: the microscopic structure of concentrated hydroxide solutions,” *J. Chem. Phys.*, vol. 122, p. 194509, 2005.

[209] K. R. Brorsen, S. R. Pruitt, and M. S. Gordon, “Surface affinity of the hydronium ion: The effective fragment potential and umbrella sampling,” *J. Phys. Chem. B*, vol. 118, pp. 14382–14387, 2014.

[210] C. Bai and J. Herzfeld, “Surface propensities of the self-ions of water,” *ACS Cent Sci.*, vol. 2, pp. 225–231, 2016.

[211] A. M. Beattie, J. K. Djerdjev and G. G. Warr, “The surface of neat water is basic,” *Faraday Discuss.*, vol. 141, pp. 31–39, 2009.

[212] P. B. Petersen and R. J. Saykally, “Is the liquid water surface basic or acidic? Macroscopic vs. molecular-scale investigations,” *Chem. Phys. Lett.*, vol. 458, pp. 255–261, 2008.

[213] P. B. Petersen and R. J. Saykally, “Evidence for an enhanced hydronium concentration at the liquid water surface,” *J. Phys. Chem. B*, vol. 109, pp. 7976–7980, 2005.

[214] V. Buch, A. Milet, R. Vácha, P. Jungwirth, and J. P. Devlin, “Water surface is acidic,” *PNAS*, vol. 104, pp. 7342–7347, 2007.

[215] T. L. Tarbuck, S. T. Ota, and G. L. Richmond, “Spectroscopic studies of solvated hydrogen and hydroxide ions at aqueous surfaces,” *J. Am. Chem. Soc.*, vol. 128, pp. 14519–14527, 2006.

[216] A. Bankura and A. Chandra, “Proton transfer through hydrogen bonds in two-dimensional water layers: A theoretical study based on *ab initio* and quantum-classical simulations,” *J. Chem. Phys*, vol. 142, p. 044701, 2015.

[217] Z. Cao, Y. Peng, T. Yan, S. Li, A. Li, and G. A. Voth, “Mechanism of fast proton transport along one-dimensional water chains confined in carbon nanotubes,” *J. Am. Chem. Soc*, vol. 132, p. 11395, 2010.

CURRICULUM VITAE

BELISA R. H. DE AQUINO
belisa.deaquino@uantwerpen.be
belisadeaquino@gmail.com

Education

- Ph.D. in Physics. **University of Antwerp**, Antwerp, Belgium 2014 - 2018
  Area of study: Atomistic simulations of soft/hard matter hybrid systems
- Master in Physics. **Federal University of Pernambuco**, Recife, Brazil 2011 - 2013
  Area of study: Mesoscopic superconductivity, vortex-antivortex matter in Corbino disks
- Bachelor in Physics. **Federal University of Pernambuco**, Recife, Brazil 2007 - 2010
  Project: Pinning of vortex matter in thin film superconductors

Skills and personal features

- Languages: **Portuguese** (native), **English** (fluent), **Spanish** (fluent), **French** (basic)
- Programming & Scientific packages/programs: **C/C++, Python, Matplotlib, Matlab, Bash, LAMMPS, VMD.**
- Desktop Editing and Productivity Software: **Vim, TEX(LATEX, BibTEX), Microsoft Office, InkScape**
- Operating Systems: **Linux, Windows**

List of publications

- B. R. H. de Aquino, H. Ghorbanfekr-Kalashami, M. Neek-Amal, and F. M. Peeters. *Ionized water confined in graphene nanochannels* Under review in Phys. Rev. B

- B. R. H. de Aquino, H. Ghorbanfekr-Kalashami, M. Neek-Amal, and F. M. Peeters. *Electrostrictive behavior of confined water subjected to GPa pressure.* Phys. Rev. B, **97**, 144111, 2018. doi:10.1103/PhysRevB.97.144111

- B. R. H. de Aquino, M. Neek-Amal, and M. V. Milošević. *Unconventional two-dimensional vibrations of a decorated carbon nanotube under electric field: linking actuation to advanced sensing ability* Sci. Rep., **7**, 13481, 2017. doi:10.1038/s41598-017-12647-2

- L. R. E. Cabral, B. R. C. H. T. de Aquino, C. C. de Souza Silva, M. V. Milošević, and F. M. Peeters. *Two-shell vortex and antivortex dynamics in a Corbino superconducting disk.* Phys. Rev. B, **93**, 014515, 2016. doi:10.1103/PhysRevB.93.014515

- B. R. C. H. T. de Aquino, L. R. E. Cabral, C. C. de Souza Silva, J. Albino Aguiar, M. V. Milošević, and F. M. Peeters. *Dynamic phases of vortex-antivortex molecules in a Corbino disk with magnetic dipole on top* Physica C, **479**, 115, 2012. doi:10.1016/j.physc.2011.12.016

Conferences and other activities

- B. R. H. de Aquino, H. Ghorbanfekr-Kalashami, M. Neek-Amal, F. M. Peeters. Electrostrictive behavior of confined water subjected to GPa pressure. In: *Belgian Physical Society (BPS) Annual Scientific Meeting*, Antwerp, Belgium, April 11, 2018. Poster.

- *Biomolecular data mining: a hands-on training.* University of Antwerp, Antwerp, Belgium, September 11–13, 2017.

- B. R. H. de Aquino, M. Neek-Amal, M. V. Milošević. Unconventional Two dimensional Vibrations of a Decorated Carbon Nanotube Under Electric Field. In: *BPS Annual Scientific Meeting*, Mons, Belgium, May 17, 2017. Poster.

- *Electrochemistry and Bio-electrochemistry: Fundamentals and Applications (3rd edition).* University of Antwerp, Antwerp, Belgium, August 18–22, 2014.

- *45th IFF Spring School - Computing Solids: Models, Ab-inition Methods and Supercomputing.* Forschungszentrum Jülich, Jülich, Germany, March 10–21, 2014.

- B. R. H. de Aquino, L. R. E. Cabral, C. C. de Souza Silva, J. A. Aguiar, M. V. Milošević, F. M. Peeters. Vortex-antivortex motion in a superconducting Corbino disk in the presence of a magnetic dot on top. In: *XXXV National Meeting of Condensed Matter Physics (ENFMC)*, Águas de Lindóia-SP, Brazil, May 14-18, 2012. Oral.

- B. R. H. de Aquino, L. R. E. Cabral, C. C. de Souza Silva, J. A. Aguiar, M. V. Milošević, F. M. Peeters. Vortex dynamics in a Corbino disk in the presence of a magnetic dipole. In: *Physics Meeting 2011 - XXXIV ENFMC*, Foz do Iguaçu-PR, Brazil, Jun 5-10, 2011. Oral.